UNIVERSITY OF OTTAWA

Characterization Techniques and Optimization Principles for Multi-Junction Solar Cells and Maximum Long Term Performance of CPV Systems

Mark Yandt, B. Eng. Mgt., M. A. Sc.

A thesis submitted to the Faculty of Graduate and Postdoctoral Studies in partial fulfilment of the requirements for the Doctorate of Philosophy degree in Electrical and Computer Engineering.

February, 2017

School of Electrical Engineering and Computer Science
University of Ottawa

The larger the island of knowledge, the longer the shoreline of wonder.

Ralph W. Sockman

TABLE OF CONTENTS

LIST OF FIGURES

LIST OF ACRONYMS

PV	Photovoltaics
CPV	Concentrating Photovoltaics
EQE	External Quantum Efficiency
IQE	Internal Quantum Efficiency
APECS Project	Advancing Photovoltaics for Economical Concentrator Systems
ASTM	American Society for Testing and Materials
AM	Air Mass
AM1.5d, AM1.5g,	Geometric Air Mass value of 1.5 for the direct and global insolation
AM0	Air Mass of extraterrestrial insolation
SMARTS2	Simple Model of the Atmospheric Radiative Transfer of Sunshine
FF	Fill Factor
TCAD	Technology Computer Aided Design
OTF	Optical Transfer Function
MPPT	Maximum Power Point Tracker
L-I-V curve	Light-Current-Voltage curve

LIST OF SYMBOLS

$N_{photons}$	Number of photons
Irr	Spectral irradiance
E_{ph}	Energy of a photon
λ	Wavelength
T	Temperature
t	Time
E	Energy
h	Planck's constant
c	Speed of light
k, k_B	Boltzmann constant
e	Euler's number, base of the natural logarithm
θ	Zenith angle of the sun
I_d	Diode current
V_d	Diode voltage
J_o	Saturation current density
n	Ideality factor
q	Elementary charge
I_{mp}	Current at a solar cell's maximum power point
V_{mp}	Voltage at a solar cell's maximum power point
I_{sc}	Short circuit current
V_{oc}	Open circuit voltage
R_s	Series resistance
R_{sh}	Shunt resistance
X	Concentration, number of suns
J_{ph}	Photo current density
E_g	Semiconductor bandgap

ABSTRACT

Two related bodies of work are presented, both of which aim to further the rapid development of next generation concentrating photovoltaic systems using high efficiency multi-junction solar cells. They are complementary since the characterization of commercial devices and the systematic application of design principles for future designs must progress in parallel in order to accelerate iterative improvements.

First addressed, is the field characterization of state of the art concentrating photovoltaic systems. Performance modeling and root cause analysis of deviations from the modeling results are critical for bringing reliable high value products to the market. Two complementary tools are presented that facilitate acceleration of the development cycle. The "Dynamic real-time I-V Curve Measurement System…" provides a live picture of the current-voltage characteristics of a CPV module. This provides the user with an intuitive understanding of how module performance responds under perturbation. The "Shutter technique for noninvasive individual cell characterization in sealed concentrating photovoltaic modules," allows the user to probe individual cell characteristics within a sealed module. This facilitates non-invasive characterization of modules that are in situ. Together, these tools were used to diagnose the wide spread failure of epoxy connections between the carrier and the emitter of bypass diodes installed in sealed commercial modules.

Next, the optimization principals that are used to choose energy yield maximizing bandgap combinations for multi-junction solar cells are investigated. It is well understood that, due to differences in the solar resource in different geographical locations, this is fundamentally a local optimization problem. However, until now, a robust methodology for determining the influences of geography and atmospheric content on the ideal design point has not been developed. This analysis is presented and the influence of changing environment on the representative spectra that are used to optimize bandgap combinations is demonstrated. Calculations are confirmed with ground measurements in Ottawa, Canada and the global trends are refined for this particular location. Further, as cell designers begin to take advantage of more flexible manufacturing processes, it is critical to know if and how optimization criteria must change for solar cells with more junctions. This analysis is expanded to account for the differences between cells with up to 8 subcell bandgaps.

A number of software tools were also developed for the Sunlab during this work. A multi-junction solar cell model calibration tool was developed to determine the parameters that describe each subcell. The tool fits a two diode model to temperature dependent measurements of each subcell and provides the fitting parameters so that the performance of multi-junction solar cells composed of those subcells can be modeled for real world conditions before they are put on-sun. A multi-junction bandgap optimization tool was developed to more quickly and robustly determine the ideal bandgap combinations for a set of input spectra. The optimization process outputs the current results during iteration so that they may be visualized. Finally, software tools that compute annual energy yield for input multi-junction cell parameters were developed. Both a brute force tool that computes energy harvested at each time step, and an accelerated tool that first bins time steps into discrete bins were developed. These tools will continue to be used by members of the Sunlab.

ACKNOWLEDGEMENTS

Thank you Dr. Henry Schriemer and Dr. Karin Hinzer for your ongoing support and guidance since I began working toward my Master's degree 6 years ago. I have relied heavily on your advice, both academic and otherwise, and I am so thankful to have had enthusiastic supervisors who care personally about each and every student under their tutelage. You have given me opportunities to develop the softer skills involved in research. Team work and clear communication are highly valued in the Sunlab and this has helped me tremendously. I have particularly appreciated the collaborative culture you foster among your students, and believe this to be one of the greatest strengths of the Sunlab. You encourage us to challenge, discuss, critique, but ultimately help each other learn and we, your students, are all better off because of this.

Thank you Dr. John Cook for your enthusiastic, can-do attitude, even when it meant flipping shutters for me on a ladder in the wind at -10°C in 2 feet of snow. Your knowledge of the literature is inspiring and I could always count on your curiosity if I needed help outside in the cold or to refine the design of a new experiment.

Thank you to all of the post docs and students in the Sunlab. In particular, Dr. Chris Valdevia, Dr. Alex Walker, Dr. Olivier Theriaut and Dr. Ahmed Gabr: you helped me through the steepest part of my learning curve when I first began my studies and I couldn't have made it to the end of my Ph.D. without you. Matt Wilkins, Viktar Tatsiankou, Ross Cheriton, and Patrick McVey: you have been incredible team members in the Sunlab and I have counted on you for endless favours, opinions and explanations. It has been a pleasure working with each of you.

Thank you Mom, Dad and Greg for your ongoing support. You have given me all the tools needed to pursue higher education and I feel so fortunate to have the opportunity. I hope to pay it forward.

Finally, to my beautiful wife, Jenny, thank you for your unconditional love, for putting up with the engineer in me that often prioritizes efficiency above all else, and for being my best friend. The last two years have been the best of my life, and I look forward to living many more at your side.

STATEMENT OF ORIGINALITY

Except where stated otherwise, the results presented in this thesis were obtained by the author during the period of his Ph.D. research under the supervision of Dr. Karin Hinzer and Dr. Henry Schriemer. They are, to the best of the author's knowledge, original.

PUBLICATIONS

The following publications and presentations resulted from work performed during the completion of this thesis.

1. **M. D. Yandt**, K. Hinzer, H. Schriemer, "Representative Atmospheric Parameters for Multi-Junction Solar Cell Design", To be submitted to IEEE Journal of Photovoltaics March 2017.
2. **M. D. Yandt**, K. Hinzer, H. Schriemer, "Efficient Multi-Junction Solar Cell Design for Maximum Annual Energy Yield by Representative Spectrum Selection", IEEE Journal of Photovoltaics, 7 (2), 695-701 (2017); doi: 10.1109/JPHOTOV.2016.2638040.
3. **M. D. Yandt**, K. Hinzer, H. Schriemer, "Identifying Representative Air Masses for Multi-Junction Solar Cell Bandgap Optimization to Maximize Annual Energy Yield", 42nd IEEE Photovoltaic Specialists Conference (PVSC), New Orleans, LA, USA, 14 19 June 2015
4. **M. D. Yandt**, J. P. D. Cook, K. Hinzer, H. Schriemer, "Shutter technique for noninvasive individual cell characterization in sealed CPV modules", IEEE J. Photovoltaics 5 (2), 691-696, (2015); doi: 10.1109/JPHOTOV.2015.2392943
5. **M. D. Yandt**, J. P. D. Cook, M. Kelly, H. Schriemer, K. Hinzer, "Dynamic Real-Time I–V Curve Measurement System for Indoor/Outdoor Characterization of Photovoltaic Cells and Modules", IEEE Journal of Photovoltaics 5 (1), 337-343, (2015); doi: 10.1109/JPHOTOV.2014.2366690.
6. **M. D. Yandt**, J. P. D. Cook, J. F. Wheeldon, H. Schriemer, K. Hinzer, (2013) "Shutter Technique for Deconvolution of Individual Cell Performance in Multi-Cell CPV Modules" (CPV-9), Miyazaki, Japan, April 15 - 17, 2013
7. J. P. D. Cook, **M D. Yandt**, Michael Kelly, J. F. Wheeldon, K. Hinzer, H. Schriemer, "Shutter array technique for real-time non-invasive extraction of individual channel responses in multi-channel CPV modules", Proc. SPIE 8915, Photonics North 2013, 891509 (October 11, 2013); doi:10.1117/12.2037346
8. J. Mohammed, **M. D. Yandt**, M. Wilkins, A. Muron, T. J. Hall, J. E. Haysom, K. Hinzer, H. Schriemer, "Collection and storage of direct spectral irradiance and DNI datasets with high temporal resolution for CPV energy yield assessments", Photovoltaic Specialists Conference (PVSC), 2013 IEEE 39th, 16-21 June 2013, Tampa, FL, pp. 2320 – 2325, doi: 10.1109/PVSC.2013.6744941

1 Introduction

Concentrating photovoltaic (CPV) technology represents a higher efficiency next generation alternative to existing commercial photovoltaic solutions. The higher material and manufacturing cost of III-V based multi-junction solar cells (MJSCs) compared to most other photovoltaic technologies, including the ubiquitous silicon flat panel, is offset using relatively inexpensive large area collectors to concentrate light onto small area solar cells with world record conversion efficiencies.

CPV technologies based on III-V semiconductors offer compelling advantages over commercial silicon PV. They have excellent long term stability. Their higher efficiency means less land area needs to be used to accommodate CPV systems. The temperature dependence of III-V materials is also much less than most flat plate technologies making them a natural choice for warmer, high insolation environments. These advantages also make such MJSCs the preferred choice for space applications where weight and reliability are prioritized. Most importantly, however, the conversion efficiency of multi junction solar cells (SCs) has been increasing by almost one percent per year for more than 15 years. Since efficiency is the primary cost driver of any PV system the prospect of even higher efficiencies is a major motivator for the pursuit of the technology.

While the fundamental arguments for CPV technologies are strong, the net deployment costs are still too high to attract large scale investment. The complexity involved in cell and system optimization and the strict long term reliability requirements are both issues that are proving to be challenging hurdles for industry players in their efforts to sell high efficiency modules. It turns out that in order to pursue good MJSC design, one must have a solid grasp of the terrestrial solar resource and the nature of its fluctuating spectrum as a function of time, location, and atmospheric content [1]-[5]. The fundamentals of high efficiency solar cell design, the dependency on insolation conditions, and the factors that motivate the understanding of these dynamics are discussed in more detail in Chapter 2 to give context in the literature and to form the basis for the discussions presented in Chapter 4.

Recognizing the need for both theoretical and practical research in this growing industry, the Sunlab at the University of Ottawa positioned itself to work with several partners on the characterization, modeling and deployment of CPV systems. Under the direction of Dr. Hinzer and Dr. Schriemer, my Ph.D. work has pursued two related facets of this mandate. The first, was part of a project funded by a “Science Medicine & Engineering for Small and Medium sized Enterprises” (SME4SME) grant funded by the Canadian Federal Government. This work revolved around the upgrade and redeployment of second generation commercial CPV modules at an existing Sunlab test facility at the National Research Council campus in Ottawa ON. The modules consisted of 6 series connected triple junction solar cells under two stage Fresnel based concentrating optics.

The SME4SME project was an opportunity for the Sunlab’s industrial partner, OPEL Solar, to improve several important features of their module. Part of this work included the root-cause analysis of a steady decrease in power output that had been identified during performance analysis of the original system. Since only a limited amount of information could be gathered from the aggregate output at the inverter, it quickly became apparent that it would be necessary to take a closer look at individual modules. This prompted the development of some new tools. A “dynamic real-time I-V curve measurement system…” was developed to be able to visualize the response of modules on-sun as we investigated them. This gave us real time information about the alignment, temperature and internal functionality of the 6 series connected cells within individual modules.

This test station was published in IEEE Journal of Photovoltaics because it was the first time that a live picture of PV current voltage characteristics had been taken advantage of for system diagnostics and proved to be an invaluable piece of equipment. This publication is included in Section 3.1.

The test station was capable of tracing the current-voltage I-V curve of single modules which we could isolate from the rest of the system temporarily without damaging the modules or their connections. This gave us much better performance resolution than the output at the inverter which only measured the aggregate output of 2 strings of 15 & 18 modules each. However, we still needed to deconvolve the operation of the 6 series connected solar cells within each module to rigorously compare measured performance to the modelled performance and identify the cause of degradation.

At this point we decided to take full advantage of the fact that each solar cell in the module was fitted with a bypass diode to optically probe individual cells, through their concentrating optics, without cutting into or damaging the module. By this method, it was possible to separate the I-V characteristics of each individual, lens-cell, channel by selectively illuminating them. Selective illumination could be achieved in any number of ways but to give ourselves control over the pattern of illuminated/shaded cells, a frame was built with opaque doors exactly the size of each optical channel that fit over the module while it was on-sun. This "Shutter technique for noninvasive individual cell characterization in sealed concentrating photovoltaic modules" was also published in the Journal of Photovoltaics and is discussed in detail in Section 3.2.

Chapter 4 of this thesis describes work completed as part of a collaboration with Morgan Solar Inc., another of the Sunlab's industrial partners, during a project called Advancing Photovoltaics for Economical Concentrator Systems (or APECS) as well as another project called Concentrating Photovoltaic Energy Yield Analysis (or CPVEYA). This work involved analysis of local solar resources and the development of system models that would allow for local system performance optimization. The modeling of next generation system performance has been a consistent theme even in the very practical papers just introduced, but for this work, new models had to be developed to take a more theoretical look at how we should take advantage of the new material/design flexibility that was being refined by cell manufacturers. The obvious advantages to increasing the number of subcells in multi-junction solar cells to increase conversion efficiency was and is leading the industry to consider 4, 5 and 6 junction cell designs [8]-[12]. The difficulty is that optimizing cell designs for annual energy yield is non-trivial, encompassing a huge number of criteria including varying ambient conditions that differ with geography. This prompted a specific investigation on how to achieve "Efficient Multi-Junction Solar Cell Design for Maximum Annual Energy Yield by Representative Spectrum Selection." In this work we developed a systematic approach to determining the best representative spectrum for which to choose multi-junction bandgaps. Details of this investigation are presented in Section 4.1.

Finally, the general trends in the methodology described above were applied for Ottawa to demonstrate and verify how the methodology is used to achieve locally relevant representative spectra. To this end, an investigation of how representative atmospheric constituents affect the choice of representative spectrum in a particular location was presented. Understanding the major atmospheric influences on energy yield informs our choice of representative spectrum but also determines differences in the energy rating that we predict for a CPV system in a new location. Discussions around energy rating of CPV systems are central in the CPV industry because multi-junction PV systems are being compared to traditional silicon flat panel systems which have very stable response due to their insensitivity to the spectrum of incident light and the fact that they are capable of capturing indirect irradiance. This work has been accepted for publication in the IEEE Journal of Photovoltaics and the latest revision is presented in Section 4.2.

In Section 5, a number of software tools that were developed for the Sunlab during this work are described. A database dashboard was created which allows the data collected at various test sites to be visualized in the context of other local measurements and a system's modeled performance. An accelerated engineering solution to detailed balance bandgap optimization calculations was implemented so that efficiency maximizing bandgap combinations can be determined quickly and visualized in real time for a broad range of constraints. Brute force energy yield modeling of realistic CPV systems was accomplished with a versatile equivalent circuit model capable of incorporating semiconductor temperature dependence, a multi-junction external quantum efficiency, its temperature dependence, the concentration factor, optical transfer function of the optics, and the effects of local atmospheric perturbations on the incident spectrum. In a separate tool, acceleration of the brute force method was achieved by incorporating an air mass binning algorithm that takes advantage of measured approximations to accelerate annual energy yield calculations. The time necessary to complete detailed annual energy yield calculations was reduced by more than 3 orders of magnitude in most cases.

1.1 Thesis Outline

This thesis is presented as a collection of journal articles. Chapters 3 and 4 each include two self-contained publications that are presented either as published or as submitted if the publication is still in the journal's review process. Each paper contains its own background, theory, analysis and reference sections that position the work in the context of the concentrating photovoltaics industry. As a result some background concepts may be repeated but usually such repetition is limited to the introduction. References for non-article materials can be found at the end of the thesis in the References section.

Chapter 2 presents background fundamentals necessary to understand the performance limiting physics motivating the pursuit of multi-junction solar cells. This is necessary to fully appreciate the compelling value proposition of III-V semiconductor solar cells. This chapter also explains the physical principles used to model these solar cells in the following chapters. Where it is relevant, general equations are given and the assumptions and approximations made in the later chapters are identified.

Chapters 3.1 and 3.2 present journal articles that discuss a test station and a testing technique that were developed together to perform a root cause analysis of degradation observed during performance monitoring of commercial CPV modules with state of the art triple junction solar cells.

Chapters 4.1 and 4.2 present journal articles that investigate the optimal design point for and energy yield benefit of next generation multi-junction solar cells with up to 8 subcells. The first of these papers attempts to demonstrate as plainly as possible the complexities of multi-junction bandgap optimization for annual energy yield. It addresses these complexities by outlining a novel systematic approach to bandgap selection and comparing it to the ubiquitous approach. The second of these papers uses measured data collected in 2015 to analyze the effect of fluctuating atmospheric parameters, including aerosol optical depth (AOD) and precipitable water (PW), on the design point used to optimize bandgap combinations. A practical approach for the extraction of representative parameters from local historical datasets is provided.

Chapter 5 describes the software tools developed in order to perform the modeling presented in various parts of this thesis. These tools are particularly valuable in terms of their computational efficiency and the ability to visualize the calculations that are being performed in real time.

A conclusion is presented in Chapter 6 in order to summarize the cumulative value of this body of work. The main conclusions are restated. The limitations of the work are acknowledged and where appropriate, next steps are noted.

1.2 Copyright Permissions

1.2.1 Chapter 3.1

The article in this chapter is presented in full and is reprinted with the permission of IEEE Journal of Photovoltaics.

M. D. Yandt, J. P. D. Cook, M. Kelly, H. Schriemer, K. Hinzer, "Dynamic Real-Time I–V Curve Measurement System for Indoor/Outdoor Characterization of Photovoltaic Cells and Modules", IEEE J. Photovoltaics 5 (1), 337-343, (2015). Doi: 10.1109/JPHOTOV.2014.2366690.

1.2.2 Chapter 3.2

The article in this chapter is presented in full and is reprinted with the permission of IEEE Journal of Photovoltaics.

M. D. Yandt, J. P. D. Cook, K. Hinzer, H. Schriemer, "Shutter technique for noninvasive individual cell characterization in sealed CPV modules", IEEE J. Photovoltaics 5 (2), 691-696, (2015). Doi: 10.1109/JPHOTOV.2015.2392943

1.2.3 Chapter 4.1

The article in this chapter is presented in full and is reprinted with the permission of IEEE Journal of Photovoltaics.

M. D. Yandt, K. Hinzer, H. Schriemer, "Efficient Multi-Junction Solar Cell Design for Maximum Annual Energy Yield by Representative Spectrum Selection", IEEE Journal of Photovoltaics, Accepted for publication July 2016.

1.2.4 Chapter 4.2

The article is in review.

M. D. Yandt, K. Hinzer, H. Schriemer, "Representative Atmospheric Parameters for Multi-Junction Solar Cell Design", to be submitted to IEEE Journal of Photovoltaics, March, 2017.

2 Fundamentals of Multi-Junction Solar Cell Design

Since the late 1990's world record solar cell performance has improved by almost one percent in absolute efficiency per year [6]. Conversion efficiencies well above the single junction, 1000 sun limit of 37 percent have been demonstrated for concentrator cells with 3, and most recently 4 junctions (called subcells) [6]-[13]. The most efficient solar cells designed, so far, are multi-junction solar cells (MJSCs) comprised of monolithically grown layers of semiconductor materials with bandgap energies carefully chosen for their absorption properties. These semiconductor layers are engineered with exceptional purity and crystallinity. This allows for dopants to be introduced, while maintaining the near ideal electronic properties of crystalline semiconductors, to create a large area p-n junction in each subcell during the epitaxial growth of the layer. Stacks of p-n junctions, each made in a different semiconductor with different bandgap energy, can thus be ordered vertically in a device and connected with tunnel junctions to provide efficient broadband absorption and charge separation under illumination.

In essence, white light from the sun, comprised of electromagnetic energy at wavelengths between the ultraviolet (~280 nm) and the near infrared (~4 µm), sees a series of slightly less transparent windows as it strikes a MJCS. Short wavelength, high energy photons are absorbed immediately upon entering the cell while longer wavelengths are transmitted through the first layers of the cell until they come to a material with a bandgap lower than their photon energy and are absorbed. This process may be visualized with the help of Figure 1 which will be described shortly.

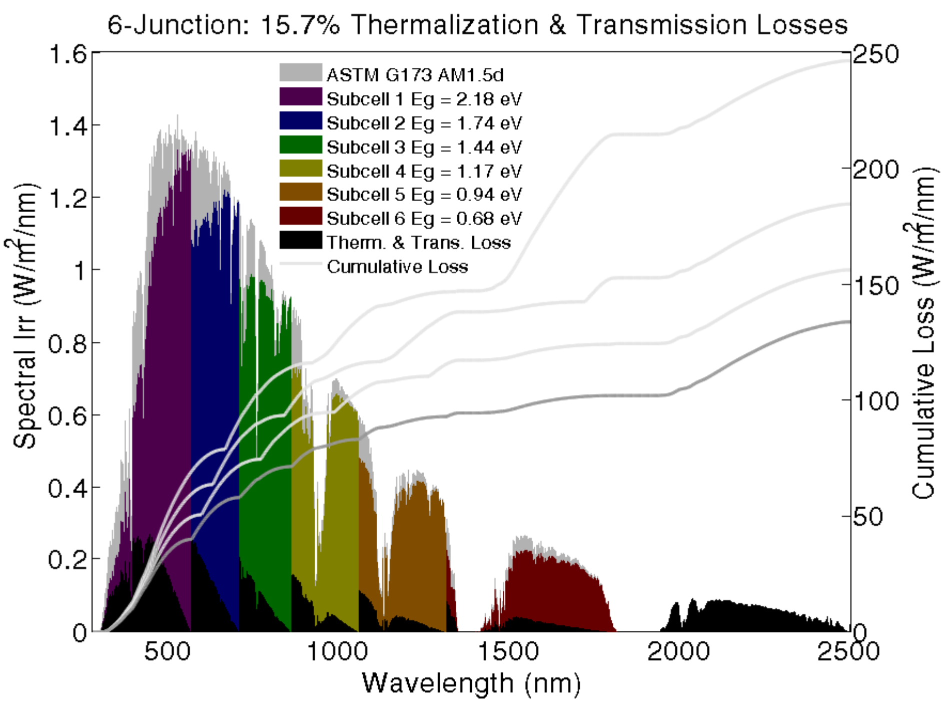

Figure 1: Multi-junction solar cell thermalization and transmission losses as a function of wavelength for ideal subcell bandgap combinations.

In addition to the engineering challenges associated with manufacturing devices comprised of many different materials with different lattice constants and growth properties, is the challenge of choosing the optimal design point in the first place. For the final design, one set of material bandgaps must be chosen to harvest the variety of terrestrial spectra that could be incident on the earth's surface in a given year and geographic location. The bandgap selection process must also account for the optical transfer function of concentrating optics as well as an antireflection coating used to couple as much broadband light as possible into the multi-junction solar cell (MJSC). If cell manufacturing cost fluctuates only marginally with MJSC design, then the levelized cost of energy (total system cost divided by lifetime system energy production) is driven down by the energy per unit area that the cell can produce. The optimal design is thus chosen to maximize the long term energy yield of the deployed system.

Incentive to increase the number of junctions with optimally tuned bandgaps exists because even as manufacturing processes are refined (eliminating parasitic losses) cell designers must still accept fundamental losses due to thermalization and transmission as shown in Figure 1. Multi-junction thermalization and transmission losses represent the most significant fundamental losses experienced in photovoltaic cells. These losses (black) and the power absorbed by each subcell (coloured areas) are depicted here as a function of wavelength for a 6-junction solar cell with bandgaps tuned to optimally harvest the ASTM G173 AM1.5d spectrum (grey). Overlaid are the cumulative thermalization and transmission losses for 3-6 junction cells which sum to 28.2%, 21.4%, 18.2%, and 15.7% of the available power respectively. Since this thesis pursues the theoretical design points that must be targeted in order to maximize annual energy yield, no consideration is given to the manufacturability of the bandgaps presented in the figure. It is recognized, however, that many of the bandgap combinations discussed have not been realized in practice and that it may be very difficult to do so.

From Figure 1 we see that, if only thermalization and transmission losses are considered, the efficiency with which the energy of a photon is harvested depends on the energy proximity to the materials bandgap edge. In the figure all of the photons with energy greater than that of the lowest energy bandgap (~0.68 eV) are collected. Photons with energy lower than 0.68 eV are transmitted through all of the cells and never absorbed. This is known as transmission loss. For photons with energies equaling the band edge, the free charge carriers that are generated by the absorption process are collected at the same energy as the photon that promoted the carrier. Thus no energy is wasted. However, even in this ideal model, photons with slightly higher energy absorbed in the same subcell cannot be collected at the photon energy because, once absorbed, any excess energy (above the bandgap) held by the resulting carrier is quickly coupled into the lattice through vibrations and, effectively, heat production. This process is known as thermalization.

As Figure 1 shows, harnessing more of the available photon energy in each part the solar spectrum can be achieved by strategically increasing the number of material bandgaps. As a result, 4, 5, and 6 junction devices have been proposed and the corresponding benefits to overall power production quantified [9]-[11]. As manufacturing processes that allow for the fabrication of solar cells with more junctions become available, the selection of material bandgaps becomes an ever more central discussion [12]-[13]. Such decisions are based on the local spectral irradiance over a year (which is highly variable), concentration ratio, operating temperature, and on the transmission characteristics of the optics used to concentrate light onto, and couple light into, the cell. These design considerations among numerous others define an optimization problem that has many moving parts. The final two papers in this thesis provide systematic design principals that acknowledge all of these factors appropriately so it is convenient to show how these fundamental inputs are accounted for now.

Broadly speaking, energy yield calculations begin with a number of inputs, the primary one being the spectral irradiance which is the wavelength dependent measurement of the energy source that MJSCs are designed to harvest. Portions of this spectral irradiance are harvested by each subcell and the power produced by the MJSC as a whole is defined by the electrical combination of the series connected subcells. The power produced fluctuates with the spectral irradiance and so it must be integrated over a period of time long enough to account for all possible variations in the spectral irradiance with a step size fine enough to capture influential transitions in spectral irradiance.

Let us first consider the variability of the incident solar radiation (insolation). Figure 2 shows only the daily variation in the spectral irradiance. There are a couple of important observations to be made in addition to the obvious increase in total power that occurs as the sun gets higher in the sky near solar noon.

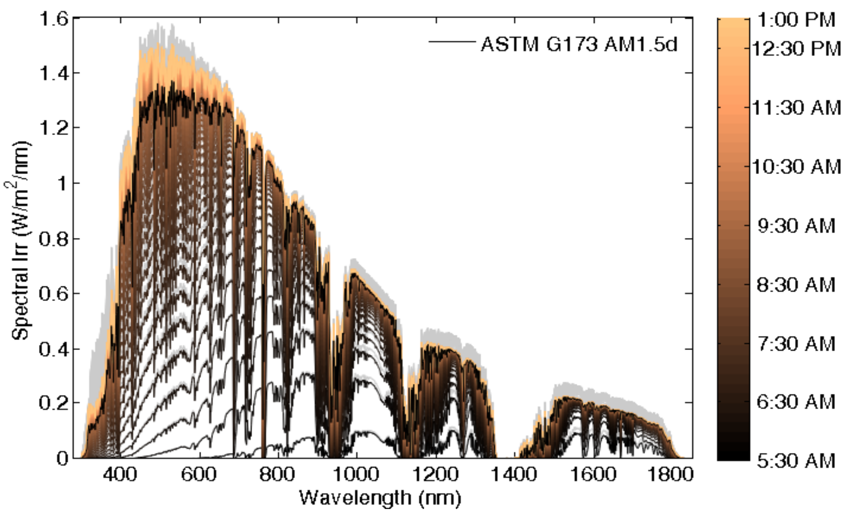

Figure 2: Spectral irradiance simulated using SMARTS2 [14] from sunrise until solar noon on June 21st in Ottawa assuming ASTM G173-03 standard atmospheric inputs. Coloured curves show the spectral irradiance (grey) modified by a 2-layer anti-reflection coating.

The first is the fact that there is a significant blue shift in the colour balance as the sun rises higher in the sky and the air mass decreases. Air mass can be approximated using varying levels of geometric detail but its effects are most simply understood using a flat earth approximation and by assuming that the atmosphere is uniform in thickness and density. These are pretty good approximations for solar zenith angles less than about 80 degrees. They lead to the following trigonometric description of the thickness of the atmosphere, relative to the vertical column, that sunlight must shine through on its way to the surface of the earth:

$$\mathrm{AM} = \frac{1}{\cos(\theta)} \tag{1}$$

where θ is the zenith angle of the sun [15]. Air mass measures the amount of atmosphere that the suns light must penetrate before reaching the earth's surface. If we relax the flat earth approximation which break down as the sun approaches the horizon at large zenith angles the relative air mass can then be found using a homogenious, non-refractive, radially symmetric atmosphere approximation at sea level according to,

$$\mathrm{AM} = \sqrt{\left(\frac{\mathrm{r}_E}{h_{ATM}}\cos(\theta)\right)^2 + 2\frac{\mathrm{r}_E}{h_{ATM}} + 1} - \frac{\mathrm{r}_E}{h_{ATM}}\cos(\theta) \quad (2)$$

where, r_E, is the radius of the earth and, h_{ATM}, is the height of the atmosphere [16]. This formula can be used in conjunction with a solar position calculator [17] to estimate the air mass at any location and point in time. The effect of air mass on the spectral irradiance is the single most important spectral influence throughout the year because it fluctuates drastically on a daily basis and defines the amount of scattering and absorption that occur due to all of the atmospheric constituents. Rayleigh scattering, aerosol extinction, precipitable water absorption, and trace gas absorption are just a few of the mechanisms affected by the air mass. To first order, transmission through the atmosphere for these components (with the exception of water absorption) is given by:

$$T_\lambda = \exp(-\mathrm{AM} \cdot \tau_\lambda) \quad (3)$$

where τ_λ is a dimensionless "optical thickness" and is a measure of the absorbing power of an atmospheric constituent [14],[18]. In general, this optical thickness called turbidity is a function of wavelength which indicates the likelihood of an absorption or scattering event, and also represents, in some way, the concentration and particulate size of the atmospheric constituent.

The second notable feature in Figure 2 is the fact that the terrestrial spectrum has some major absorption dips. The largest of these are due to precipitable water absorption. They will have a huge impact on the implementation of an optimization process whereby we search for the best bandgaps to harvest a particular spectrum. This is discussed in detail in the paper presented in Section 4.1.

The obvious variability in the spectral irradiance means that energy yields must be computed over at least one entire year to account for the associated seasonal and annual changes in solar position and air mass. It should also be noted that the incident spectral irradiance may be modified before it enters a solar cell by any materials on the surface of the solar cell and even in the transition from air to the semiconductor material. The effects of concentrating optics, packaging, and anti-reflection coatings must all be accounted for when a particular system is under investigation.

Once the atmospheric dynamics that affect the insolation are well understood, the material properties of the individual subcells must be described in order to calculate the photo-current that will be generated in each subcell at any given point in time. Photocurrent density is given by:

$$J_{ph} = q\int_{\lambda_1}^{\lambda_2} \frac{Irr(\lambda)}{E_{ph}(\lambda)} \cdot IQE(\lambda, T) \cdot OTF(\lambda, T) \cdot d\lambda \quad (4)$$

where q is the elementary charge, λ_1 and λ_2 bound the solar spectrum, $Irr(\lambda)$ is the spectral irradiance, $E_{ph}(\lambda)$ is the energy of a photon at wavelength λ, $IQE(\lambda, T)$ is the internal quantum efficiency of the absorbing material which is a function of wavelength and temperature, and

$OTF(\lambda, T)$ is the optical transfer function describing wavelength dependent changes in $Irr(\lambda)$ as it enters the solar cell which is also a function of temperature [15].

In Section 4 of this thesis, the desire is to determine the energy yield maximizing design point rather than to accurately model the energy yield of a particular system, so some approximations are warranted. For these purposes, when theoretical materials are considered, the internal quantum efficiency is assumed to be a step function for each subcell. The optical transfer function and cell junction temperature (T) of a particular system would bias the results for a particular system and thus limit the generality of our conclusions so it is not applied with the express understanding that the $OTF(\lambda, T)$ must be taken into consideration when mapping the general results in Section 4 to a particular system. Thus, for the purposes of the investigations presented later, the photocurrent density is computed via:

$$J_{ph_i} = q \int_{E_{g_{i-1}}}^{E_{g_i}} \frac{Irr(\lambda)}{E_{ph}(\lambda)} \cdot d\lambda \tag{5}$$

where E_{g_i} is the bandgap of the i_{th} subcell in wavelength units, (i = 1 being the top subcell and E_{g_0} is the photon energy of λ_1 from Equation 4. This simplified form accounts for all of the physics involved in the absorption of light and the promotion of charge carriers. The next step is to account for the extraction of those carriers from the solar cell in such a way that electrical power can be harvested. We must relate the current produced by the device to the generated photocurrent and the potential energy at which the carriers are extracted from the device. For a p-n junction with parasitic series (R_s) and shunt (R_{sh}) resistances that relation is given by:

$$J = J_{ph} - J_{o,i}\left[exp\left(\frac{q(V+JR_s)}{nk_BT}\right) - 1\right] - \frac{(V+JR_s)}{R_{sh}} \tag{6}$$

where *n* is the ideality factor which describes the type of recombination processes that are occurring in the junction (*n*=1 in the ideal case for direct bandgap semiconductors), k_B is Bolzman's constant, T is the junction temperature, and V is the voltage at which current is extracted [15]. J_o is known as the dark current coefficient or the saturation current which describes recombination processes in the junction and is a function of the materials bandgap energy. In a detailed balance limit, where only radiative recombination is considered, it is given by:

$$J_{o,i} = J_{w,i} \cdot exp\left(\frac{-E_{g,i}}{k_BT}\right) \tag{7}$$

$$J_{w,i} = \frac{2\pi q}{h^3c^2} k_BT\left[{E_{g,i}}^2 + 2k_BTE_{g,i} + 2(k_BT)^2\right] \tag{8}$$

where h is Plank's constant, c is the speed of light, and i is the junction number if several of these I-V characteristics will be added together as in [17]. In the ideal case, parasitic resistances are assumed to be negligible ($\mathrm{R_s} = 0$ and $\mathrm{R_{sh}} = \infty$) which for state of the art cells is a remarkably good approximation. Preforming these calculations for each of the junctions in the ideal 6-junction cell presented in Figure 1 gives the current-voltage (IV) characteristics in Figure 3.

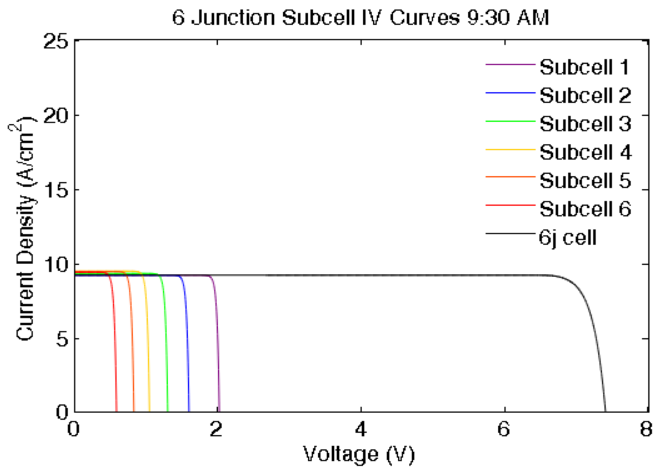

Figure 3: Subcell IV characteristics at the spectral design point (AM1.5d) which occurs at ~9:30 am on June 21st in Ottawa.

In Figure 3 the individual IV curves are added together electrically in series to achieve the black curve which is the combined IV characteristic of the MJSC. The red curve with the lowest open circuit voltage corresponds to the subcell with the lowest bandgap energy and is placed on the bottom of the cell to capture the lowest energy photons. The purple curve with the highest bandgap energy would be placed on the top of the solar cell such that the highest energy photons will be absorbed and the rest will be transmitted to subcells with progressively lower bandgap energies. It is the power we calculate from the maximum power point of this net curve that we will integrate over time to determine the energy production of this ideal cell in a given year.

It is appropriate to discuss the concept of current matching that stems from the series connection of subcells while referring to Figure 3 because one will notice that the 6-junction IV curve produces only as much current as the lowest producing subcell. To first order, overall performance is maximized when no individual subcell is limiting the current of the others. However, there is a subtle tradeoff between current and voltage when a smaller bandgap cell over produces current slightly. This improves the voltage at which carriers can be extracted from the 6-junction cell more than it reduces the current; up to a point. The result is that optimal performance is achieved when lower bandgap cells have slightly higher photocurrents than the subcells above them. At the spectral design point which has been selected intentionally in Figure 3 this effect is noticeable.

Once the power produced by a MJSC model can be extracted, the final step in determining annual energy yield is to integrate the power produced over time according to:

$$E = \int_{t_1}^{t_2} P_{max}(t) \cdot dt \tag{9}$$

where $t_1 - t_2$ = 1 year, P_{max} is the maximum power point of the MJSC at each time step, and dt is the measurement time interval between spectral measurements used as input to the cell model. Figure 4 shows short circuit current density plotted for a single day as a function of time to demonstrate how much variation in subcell photo current occurs and the resulting subcell current balances issues that occur as the air mass changes. As the sun rises and sets, there is little power on the blue end of the spectrum due mostly to preferential Rayleigh scattering of high energy photons. During the middle of the day, the lower bandgap energy subcells limit cell performance.

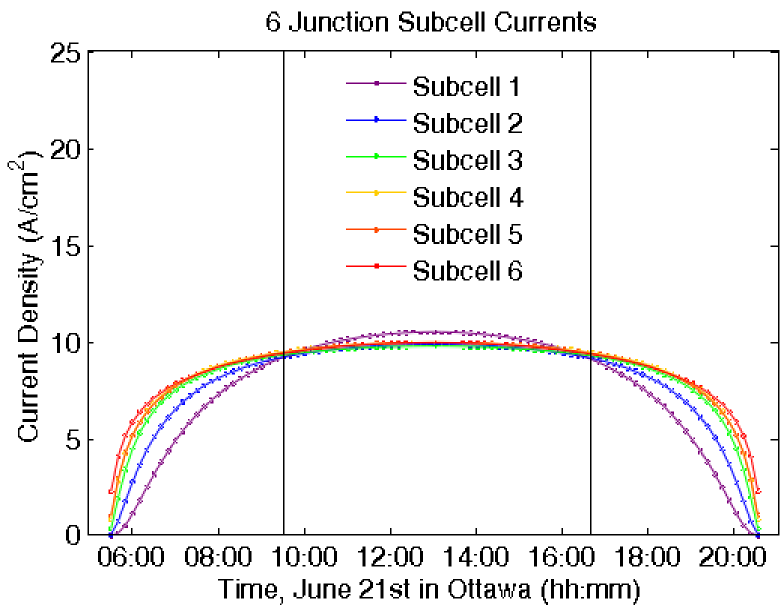

Figure 4: Short circuit current produced by each subcell on a completely sunny summer solstice in Ottawa Canada.

To capture these effects accurately on a daily basis, the integration period must be relatively small. This means that the number of energy calculations required to compute annual energy production is usually large. This process can be extremely computationally intensive depending on the complexity of the solar cell model and the size of the time steps used for the integration. Methods of accelerating this calculation were developed for the calculations performed in Section 4. They are described in detail in the paper presented in Section 4.1.

3 CPV System Characterization

3.1 A Dynamic Real-Time I-V Curve Measurement System

3.1.1 Scope and Impact

The following publication describes the design and implementation of a test station that I used to perform a root-cause analysis of long term performance degradation on a CPV demonstrator installed at the National Research Council Canada. The differentiating feature of this test station is the live picture of the I-V characteristic that it provides. This paper represents the first time that this functionality has been published as a diagnostic tool for photovoltaic performance analysis.

The test station was used for a number of projects at the Sunlab and continues to be an extremely valuable tool because it gives the user an intuitive understanding of a module's electrical response to external dynamics such as changing light conditions, temperature or alignment. During the SME4SME project the live I-V test station allowed us to watch a cell failure occur and correlate it directly with the changing light level on the cell. This observation pointed directly at the cause of the failure because instead of seeing current bypass the cell upon shading as we expected, the cell limited the current of the entire module and then quickly become shunted. This result identified bypass behavior as the culprit for system performance degradation that we were investigating. Separate instantaneous I-V measurements before and after this failure would not have revealed the cause. A faulty connection between bypass diode and carrier was later confirmed for many cells during post mortem.

3.1.2 Author Contributions

Mark D. Yandt: The scientific contributions in this manuscript are entirely my own but were supported, guided or encouraged at times by the other authors. The primary contribution is the demonstration of a live picture of the I-V characteristic of a multi-junction solar cell under varying illuminations conditions. Supporting contributions relate to the complete characterization of the live I-V test station that is presented. These include the effects of inductance, capacitance and other parasitic impedances on the sweep rate of solar cells and modules and the correct implementation of differential voltage measurements to compensate for these effects. I also contribute a systematic methodology to determine when the optimum sweep rate and to determine when parasitics will have an effect on I-V measurements.

Dr. John P. D. Cook: As a visiting researcher, John's knowledge of the literature helped inform the approach taken during station development. His experience and knowledge of existing research and vision for the types of tools that had yet to be explored was his primary contribution. John assisted me many times by connecting or disconnecting the test station terminals to modules while I made measurements. John was the first person to see my results at every step, guided and informed my findings and was an invaluable asset during the consolidation and editing of the presentation in the final manuscript.

Michael Kelly: As a summer student, Michael built the initial circuit model using SPICE software based on the circuit schematics that I designed and provided. Under my direction he implemented a table lookup that allowed the simulation of the diode behavior of a specific solar cell such that we could analyze the effect of the rest of the circuit on the measurement of the device and compare my laboratory measurements to simulations of the same non-ideal device. I would eventually use this model to produce figures 4 (b) & (d).

Dr. Henry Schriemer: As my co-supervisor and a researcher listed on the grant funding the work I performed, Henry guided the direction of the research and assisted in the editing of the final manuscript.

Dr. Karin Hinzer: As my co-supervisor and the principal researcher on the grant funding the work I performed, Karin guided the direction of the research and assisted in the editing of the final manuscript.

3.1.3 Publication

Paper attached on next page. This paper entitled, “Dynamic Real-Time I–V Curve Measurement System for Indoor/Outdoor Characterization of Photovoltaic Cells and Modules” was published in January of 2015.

M. D. Yandt, J. P. D. Cook, M. Kelly, H. Schriemer, K. Hinzer, “Dynamic Real-Time I–V Curve Measurement System for Indoor/Outdoor Characterization of Photovoltaic Cells and Modules”, IEEE J. Photovoltaics 5 (1), 337-343, (2015). Doi: 10.1109/JPHOTOV.2014.2366690.

Dynamic Real-Time *I–V* Curve Measurement System for Indoor/Outdoor Characterization of Photovoltaic Cells and Modules

Mark D. Yandt, John P. D. Cook, Michael Kelly, Henry Schriemer, *Member, IEEE*, and Karin Hinzer, *Member, IEEE*

***Abstract*—A test method that measures the current-voltage *I–V* curve of a photovoltaic (PV) cell or module in real time is presented as a means of characterizing and understanding the inherently variable nature of performance under field conditions. Temperature, incident light intensity, orientation to the light source, incident spectrum, the uniformity of illumination, as well as a diverse set of failure mechanisms, both catastrophic and otherwise, have characteristic effects on the *I–V* curve. Seeing the *I–V* curve change dynamically with these influences allows visual correlation to real-time events. With a live *I–V* curve generated by performing forward and reversed bias sweeps repeatedly, the effect of parasitic inductance and bias sweep rate on the measurement can be demonstrated directly. This technique also ensures that the device junction is held in quasi-thermal equilibrium during the measurement. The relative alignment of optics in a concentrating photovoltaic module is analyzed to demonstrate the value of the live *I–V* curve.**

***Index Terms*—Bidirectional *I–V* measurement, inductive hysteresis, live *I–V* curve, real time, test station, thermal hysteresis.**

I. Introduction

THE photovoltaic (PV) energy industry is under pressure to provide very inexpensive devices with guaranteed performance over a service life of 20 years or more [1]–[4]. Successful commercial technology innovation and development programs depend on effective understanding and control of all issues contributing to performance, manufacturability, long-term reliability, and lifecycle cost [5]–[10]. Effective electrical characterization of PV cells and modules is critical in order to shorten the associated development cycle [11].

The characteristic current–voltage (*I–V*) curve of a solar cell or module is useful in this regard because it is sensitive to many module design issues, such as spectral response, interconnection problems, optical alignment effects, thermal management issues, bypass diode faults, and parasitic impedances [12], [13].

Manuscript received July 15, 2014; revised September 5, 2014 and October 24, 2014; accepted October 25, 2014. Date of publication November 26, 2014; date of current version December 18, 2014. This work was supported by the Natural Sciences and Engineering Research Council of Canada, the National Research Council of Canada, and the Business Development Bank of Canada.

M. D. Yandt, J. P. D. Cook, H. Schriemer, and K. Hinzer are with Sunlab, University of Ottawa, Ottawa, ON K1N 6N5, Canada (e-mail: markyandt@gmail.com; john.cook@uottawa.ca; hschriemer@uottawa.ca; khinzer@uottawa.ca).

M. Kelly was with the Sunlab, University of Ottawa, Ottawa, ON K1N 6N5, Canada, and is now with Ericsson Canada, Inc., Ottawa, ON K2K 2V6, Canada (e-mail: mkelly09@gmail.com).

Color versions of one or more of the figures in this paper are available online at http://ieeexplore.ieee.org.

Digital Object Identifier 10.1109/JPHOTOV.2014.2366690

TABLE I
Time scale of phenomena affecting characteristic *I-V* curve and examples from each category of phenomena.

Time Scale	Range	Examples
Very short	< Seconds	Electrical faults, thermal runaway, diode failures [17], [19]
Short	Seconds	Shutter testing [20]
Intermediate	Seconds–hours	Cloud edges, tracker misalignments, associated cell temp. changes [21]
Long	Hours–days	Insolation variation, ambient temperature variation
Very long	Days–years	Soiling [22]–[24], UV damage [25]

Typically, a unidirectional single-scan *I–V* curve measurement is made by driving the module through a voltage range once, while monitoring current output. The initial and final states, as well as the evolution of the device under test (DUT) and its environment during the test, are not necessarily controlled or captured [14], [15]. However, the *I–V* curve is influenced by continually changing temperature, insolation, orientation to the light source, incident spectrum, and uniformity of illumination, as well as a variety of faults.

The time scale of phenomena affecting *I–V* curves can range from very short to very long (see Table I), while conventional *I–V* acquisition times depend on the particular test station design. Any phenomena varying more rapidly than this acquisition time will not be captured with fidelity. Single events affecting *I–V* response will not be captured with a single-scan test system. In field test situations, longer cable bundles are usually necessary between test station and modules, which cause parasitic resistance and inductance effects and require special treatment. In addition, the idle state between each single scan may not be reproducibly controlled, or apparent to the operator. For example, if the idle state is located at I_{sc}, V_{oc}, or P_{max}, the device will equilibrate at corresponding temperatures, which will affect the subsequent *I–V* curves [16]. This complexity suggests that a dynamic display of the real-time *I–V* curve would be valuable when attempting to distinguish among multiple phenomena that change the *I–V* curve at different rates, especially in field operation, since real-time events can be continuously correlated with real-time *I–V* evolution. We propose a test method for continuous rapid display of the *I–V* curve that permits the operator to investigate fast or transient response phenomena and to correlate these with real-time events.

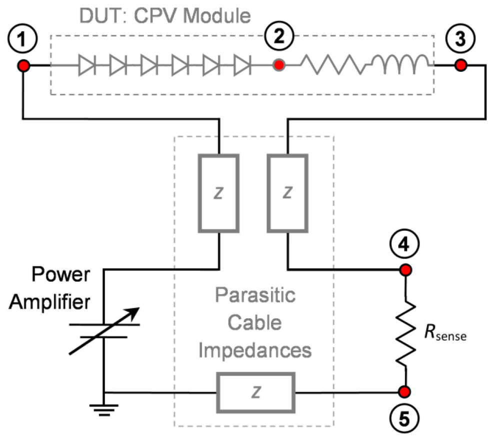

Fig. 1. Schematic of the real time *I–V* test station. The voltage in the bias circuit is measured relative to ground at four points using an oscilloscope in order to achieve two differential measurements and correct for parasitic cable impedances.

II. Experimental System

The test station is intended for both bench and field use to continuously display in real time the characteristic *I–V* curve of the DUT. We use a 200-W four-quadrant dc operational power supply/amplifier (model Kepco 20-10M) with a fast sweep rate (2 V/μs, 0.4 A/μs) to bias the DUT. An external function generator provides a 20 V_{p-p} triangular wave output that feeds the programming input of the Kepco power supply and drives its output voltage through its maximum range of 40 V_{p-p}. A high-speed four-channel digitizing oscilloscope (Agilent Technologies DSO6014A) is employed for the four-point measurements. The DUT is a concentrating PV (CPV) module consisting of six series-connected solar cell receivers each with a bypass diode. It is mounted on a pedestal sun tracker and is connected to the test station by 10-m-long AWG12 cables.

Fig. 1 presents a schematic of the *I–V* test station showing the DUT voltage bias control and five points at which the circuit potential may be monitored. The current through the DUT is determined by a differential voltage measurement from points 4 to 5 across a 0.2-Ω sense resistor $R_{\rm sense}$. A differential voltage measurement from points 1 to 2 yields the voltage across the DUT. However, if the DUT is packaged in a sealed module then the actual potential difference measured incorporates both the DUT and a short length of cable associated with resistance and inductance as if the differential measurement was made from points 1 to 3.

The four time-dependent voltages V_x measured relative to ground with the oscilloscope are shown in Fig. 2(a). Note that the dashed blue and purple curves have been scaled to more clearly show V_1 and V_5 on the same axis as V_3 and V_4. Note also that the polarities of V_3, V_4, and V_5 have been inverted to comply with convention so that the positive power portion of the resulting *I–V* curve is in the first quadrant, as shown in Fig. 2(b), where the module voltage is given by $V_1 - V_3$, and the module current by $|V_4 - V_5|/R_{\rm sense}$.

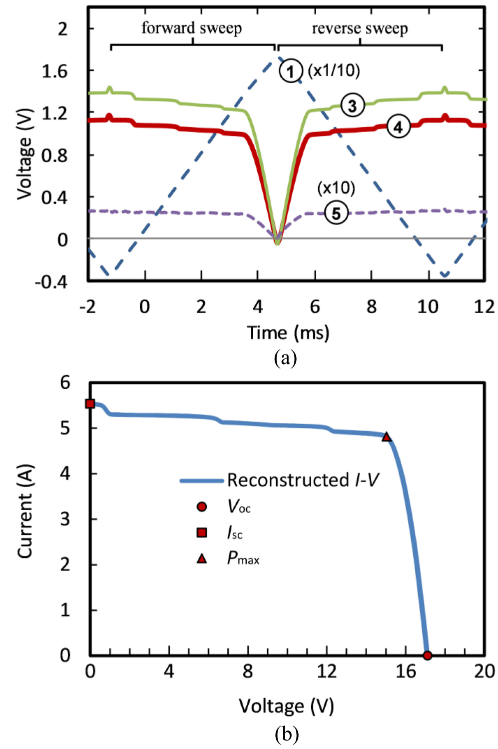

Fig. 2. (a) Time-based measurements made on the four channels of the oscilloscope corresponding to the points indicated in Fig. 1. (b) Reconstructed *I–V* curve with module current $|V_4 - V_5|/R_{\rm sense}$ versus module voltage V_1–V_3. Steps are visible at 0.6, 6.3, and 12.0 V.

The advantage of our approach arises from continuously sweeping the bias across forward and reverse directions. This allows for correlation between the bias sweep rate and any hysteresis in the live measurement. This is important in the field, where long cables are typically required to connect the test station to the PV module and particularly when sense wires for a four-point measurement cannot be placed very close to the DUT because it is sealed inside a module. As discussed below, if the sweep rate is sufficiently high, the DUT is also conveniently held in quasi-thermal equilibrium.

During this discussion, we present data from an alignment study to show the value of visually correlating the real-time adjustment of a particular parameter with its effect on the *I–V* curve. In that investigation, adjustment of module orientation was correlated with the appearance of "steps" in the module *I–V* curve. The added value is not in the instantaneous single scan of the stepped *I–V* curve [see Fig. 2(b)] but rather in the ability to watch how the steps move relative to each other as the module alignment is varied.

Figs. 2(b) and 3 show the reconstructed module *I–V* curve. The steps evident in this particular *I–V* curve are due to mechanical misalignments between the individual optical channels in the module. They are evident because the *I–V* curve was measured during an alignment study for which the module optical axis was adjusted relative to the direct beam, to probe performance at the edge of its acceptance angle. It is challenging to convey in a static figure the intuitive understanding a live *I–V* curve provides as the module alignment is modified. However,

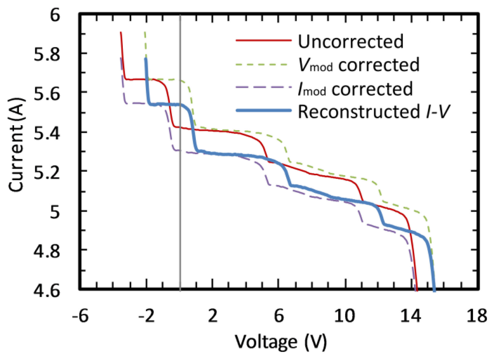

Fig. 3. Effect of parasitic circuit resistances from long cables on module *I–V* measurements. The red uncorrected *I–V* curve includes all series resistance from measurement cables as if it were captured using two-wire measurements of the module voltage and of the current sense resistor voltage. The dashed curves show the implementation of differential measurements around each of these circuit elements independently. The blue curve shows the reconstructed *I–V* curve when differential measurements are implemented for both the module and the sense resistor voltages.

as discussed further in Section III, one can visualize the steps in Fig. 2(b) appearing one at a time out of the dark *I–V* curve as the module comes on-sun, smoothly rising and falling as module alignment is adjusted. Observing the relative movement of steps allows immediate differentiation between different alignment loss phenomena. The resulting insight can be used to improve manufacturing tolerance and performance and to reduce cost.

A. Parasitic Impedance

The effect of the impedance in the connecting wires is mitigated if voltage measurements can be made by connecting directly to the relevant terminals of the DUT and the sense resistor. For field measurements, however, this is often not physically possible, as there are usually built-in module wires whose associated inductances will be in series with the DUT, as exemplified between points 2 and 3 in Fig. 1. Built-in impedances also, in principle, include internal cell capacitance such as that described in [26]–[28], but this is not included in the figure since capacitive effects are negligible in the measurements presented. We distinguish such built-in impedance from the cable impedances shown within the dashed box of Fig. 1 because the effects of the latter can be corrected, while the former cannot.

The *I–V* curves in Fig. 3 show how two differential measurements are used to correct for the voltage drops and phase shifts in the circuit that result from parasitic cable resistances and inductances in the long cables (i.e., the impedances within the dashed box of Fig. 1). The uncorrected curve is what one would measure if the long cables reaching up to the module on the tracker were considered part of the DUT as in a two point measurement, plotting $|V_4|/R_{\rm sense}$versus $V_1 - V_4$. $I_{\rm mod}$ corrected and $V_{\rm mod}$ corrected show the effects of taking differential measurements around only the sense resistor and only the CPV module, respectively; the thick blue curve includes both of these corrections.

Even though it is not possible to correct the effects of impedances that are *inside* the differential measurements, the fact that the *I–V* curve is swept continuously in both directions means that the effects of these impedances (capacitive or inductive) are immediately apparent in our real-time measurement. Even small inductances of relatively short module wires can cause hysteresis in the *I–V* curve between forward and reverse sweeps when the test station is connected to point 3. This hysteresis occurs at higher bias sweep rates, where the circuit current lags the voltage. This distortion would not be immediately obvious using the single unidirectional scan *I–V* technique, but it is explicitly revealed in the bidirectional continuous display approach, and it can be mitigated by simply reducing the sweep rate, thus ensuring an accurate *I–V* measurement. Note also that a real-time measurement provides a lower bound to the sweep rate because the *I–V* curve must appear live to the eye.

Fig. 4 shows the impact of parasitic impedance on the *I–V* measurements of a single unpackaged triple-junction solar cell on a receiver. The *I–V* curves for bias sweep rates from 690 to 6900 V/s were measured under controlled laboratory conditions using a Spectrolab XT-30 high-concentration solar simulator with continuous illumination. Fig. 4(a) shows the measurement results when the sense wires are connected to point 3, as an AWG12 cable provides a small series impedance between points 2 and 3. Fig. 4(c) shows the results for a direct connection of the sense wires to point 2, which is possible in this case because the cell is not protected within a module. The hysteresis seen in the former, primarily due to cable inductance, exists for sweep frequencies greater than 690 V/s. By contrast, no hysteresis is seen in the latter case, as the direct connection has minimal inductance. Capacitive reactance would be observed as voltage lagging current, but we observe the opposite, since inductive reactance dominates as shown in Fig. 4(a).

SPICE simulations of the circuit in Fig. 1 were compared with the measurement results to see if the impedances could be reconstructed. The simulated AWG12 results are shown in Fig. 4(b) for comparison with the measurements of Fig. 4(a). The $R = 20$ mΩ resistance value found is in general agreement with the sum of typical contact ($\sim$5 mΩ per contact) and line resistances (5.2 mΩ/m). The $L = 2$ μH inductance value found is in reasonable agreement with the expected 2.7-μH wire inductance calculated using [29]:

$$L = 2l\left[\ln\left(4l/d\right) - 1 + \frac{\mu}{4} + \frac{d}{2l}\right] \quad (1)$$

where L is in μH, $l = 200$ cm is the wire length, $d = 0.2053$ cm is its diameter, and $\mu = 1$ is the wire's relative magnetic permeability. Likewise, simulations of a direct connection, as shown in Fig. 4(d) using $L = R = 0$, are in agreement with the measured results shown in Fig. 4(c).

B. Effective Junction Temperature

In the single-scan test method, the temperature of the cell-carrier assembly assumes the value dictated by the idle condition of the test station. By contrast, in our dynamic approach, the test station is continuously changing the bias point; therefore, the temperature of the DUT is dictated by the evolution of the power extracted from the cell during repeated sweeps. At low sweep

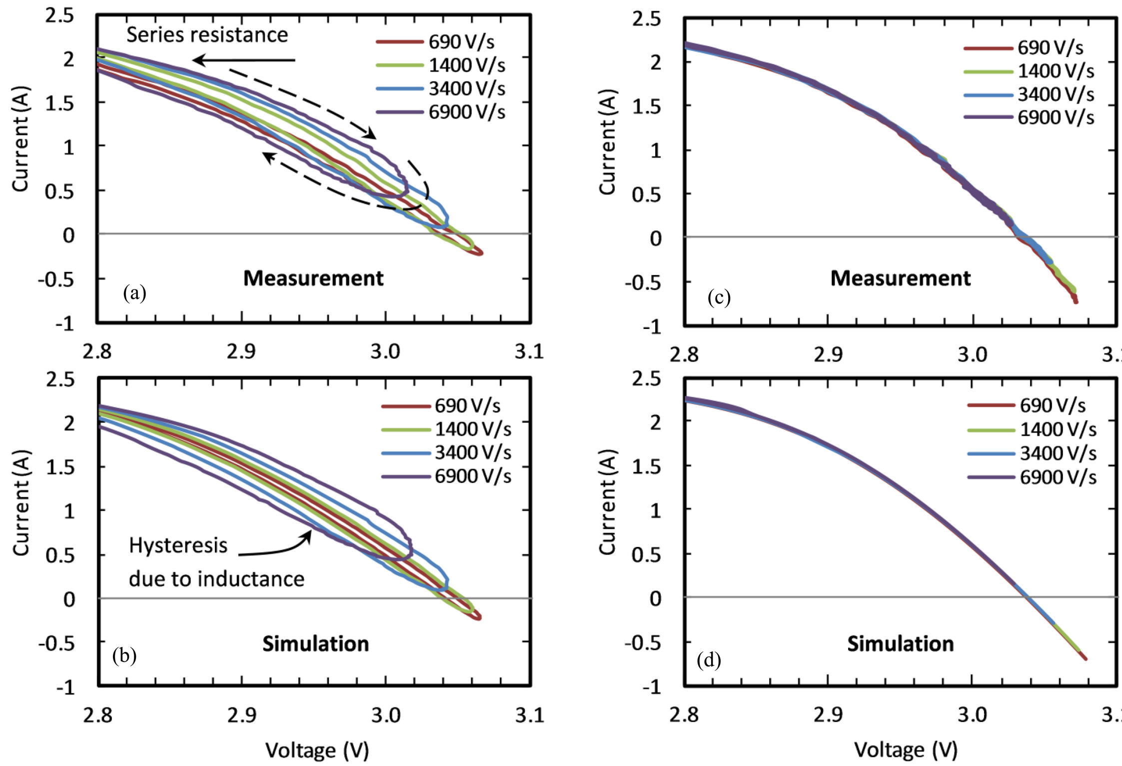

Fig. 4. (a) Measured and (b) simulated *I–V* curves of a triple-junction cell measured at sweep rates between 690–6900 V/s for which the connection between points 2 and 3 was a 200-cm AWG 12 cable. Dashed arrows indicate sweep direction confirming an inductive effect in which the current lags the voltage. (c) Measured and (d) simulated *I–V* curves of a triple-junction cell measured at sweep rates between 690–6900 V/s for a direct connection to point 2.

rates (<500 V/s), small inductances between points 2 and 3 have no significant impact on the cell's *I–V* characteristic, as demonstrated in Fig. 5. However, hysteresis is visible at a bias sweep rate of 0.69 V/s since the cell-carrier assembly's thermal time constant is similar to the sweep rate. At lower sweep rates (<1 V/s in this case, a rate which is dependent on thermal coupling to the heat sink beneath the cell), the temperature of the cell begins to follow bias point changes, with individual *I–V* points recorded at different cell junction temperatures. At higher sweep rates, the junction temperature does not have sufficient time to change before the bias point has scanned through the entire *I–V* curve; thus, quasi-thermal equilibrium is reached.

The average power extracted from the solar cell during testing at any sweep rate can be calculated from the time-weighted average of the power curve within the range of the voltage sweep as explained in [16]. If desired, this can be used to adjust the maximum power point (MPP) to the thermal conditions that prevail during static operation. It is also noteworthy that the solar cell is held at a temperature much closer to its MPP temperature so that the magnitude of the correction required is small compared with that required when a solar cell is idled at open-circuit voltage or at short-circuit current.

III. Applications

The characterization study described previously provides the basis for dynamic display and capture of accurate *I–V* curves over long cable bundles in the field, with proper understanding of reactive parasitics and junction temperature dynamics. Almost all testing applications benefit from such capability, but a few are of particular interest.

The ability to capture and even resolve the dynamics of an operational change or component failure that occurs during a stress test is useful and is a capability that is not easily achieved by other means. Traditional methods (i.e., taking instantaneous *I–V* scans or monitoring a single bias point over time) do not provide a complete time-resolved picture of the *I–V* curve. Live *I–V* capability allows for very short and intermediate length single events that can change any part of the *I–V* curve to be correlated in time with external influences on the cell.

Examples of tests that have the potential to change the *I–V* curve or to cause cell failures include: mechanically bending the module (very short to short time scale), mechanically bending the concentrating optics (very short to short), partially shading cells or groups of cells in strings (short) [11], heating or cooling a cell assembly (intermediate) [30], and moving the module off axis or through the edge of its acceptance angle (intermediate) [31]. It is also possible to resolve and visualize the performance penalty paid when a tracking system updates its pointing direction in discrete coarse steps rather than in a continuous fashion (short to intermediate) [32].

To demonstrate the value of the live *I–V* curve, we expand our explanation of the alignment study first presented in Fig. 2. The "staircase" *I–V* curves in Fig. 2(b) are a result of differences in the distinct *I–V* characteristics of the six individual channels (cell receiver and optics) that comprise the module

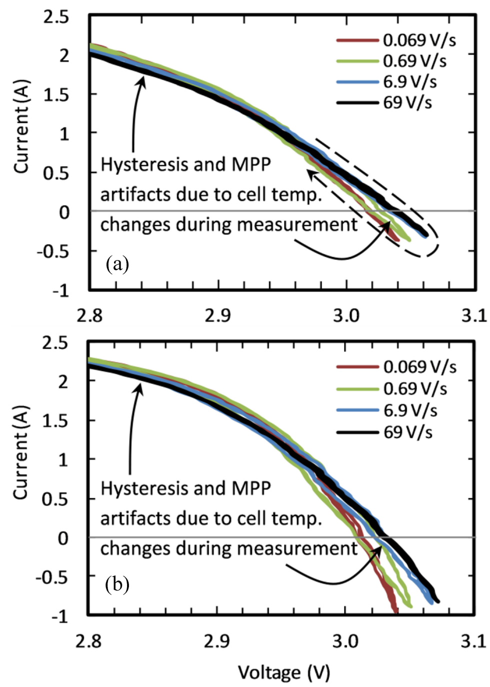

Fig. 5. *I–V* curves of a triple-junction cell measured at sweep rates between 0.069–69 V/s bounding the cell-carrier thermal time constant with (a) connection to point 3 with a 1.2-m AWG 12 cable between points 2 and 3 and (b) direct connection to point 2. Dashed arrow indicates sweep direction. The red curve shows the result of an extremely slow sweep rate in which the MPP and the V_{oc} are increased and decreased, respectively, due to different levels of electrical power extraction (and, hence, cell temperature) during different parts of the measurement.

response. Since this is a CPV module, the concentrating optics must be aligned along their direct normal axis. Differing deviations of individual optical axes from direct normal mean that these acceptance angles are not all mutually coincident. This is confirmed by an alignment study, where the sun is deliberately allowed to walk through the acceptance angle of the module. As the direct beam begins to enter the acceptance angle of the most negatively aligned optic, its light *I–V* curve begins to rise out of the module dark *I–V* curve in real time. As the module comes more fully on sun, *I–V* curves from the other cells begin to contribute. The number of steps in the *I–V* curve changes depending on the number of channels that are adequately aligned. This staircase effect is minimized when the module alignment is optimal. The real acceptance angle can be measured directly by watching the live picture of the *I–V* curve as the module is misaligned relative to any direct beam either on sun or in the lab. Fig. 6 shows a series of snapshots taken every 30 s, while the live *I–V* curve was evolving on screen. It shows that the steps are not evenly spaced in current and that their relative spacing is changing as the module moves off sun. This confirms that the type of misalignment is not the same from one optical channel to the next. The live aspect of the curve is critical because it shows the viewer how fast each step is rising/falling relative to the others indicating the nature of the misalignments. It allows the operator to adjust individual channels (e.g., push on bowing lenses, or twist the whole module) to determine the role (i.e., the

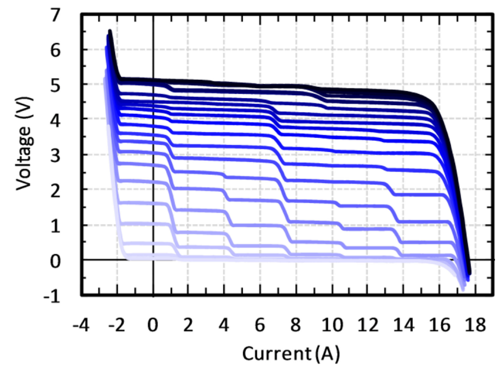

Fig. 6. Snapshots taken as the sun moved off the optical axis of a six-cell CPV module. Tracker alignment was manually frozen, while the live *I–V* characteristics were monitored. The *I–V* curves are shown for module alignments 0° (top) through 2.7° off axis (bottom) in 0.14° increments.

on-screen effect on the module *I–V* curve) that various factors are playing on the optical alignment.

IV. Conclusion

A test station has been presented that permits continuous display of the real-time characteristic *I–V* curve of a solar cell or module. The time evolution of the *I–V* curve resolves the module response to internal and external real-time events. For example, rapid changes arising from electrical intermittencies and component overstress failure can be distinguished from slower component degradation and insolation effects.

The proposed test station also ensures that unknown idle state effects do not arise, since a sufficiently rapid bidirectional scan holds the PV device in a quasi-thermal equilibrium. The value of the bidirectional scan is highlighted and temperature and inductance related hysteresis in the *I–V* curve is characterized, where hysteresis phenomena are already known and characterized in established PV technologies, the optimal scan rate has been previously established, and a single-scan capture is safe. The bidirectional dynamic display addresses the more general situation in new technologies or field installations, where a hysteresis may be operating but is unknown to the test engineer. Inductive parasitic artifacts are quickly and easily recognized in this noninvasive method and can be mitigated by optimizing the sweep rate before recording an *I–V* response. This method has been demonstrated at scan rates from 0.069 through 6900 V/s. With appropriate instrumentation, the method could be extended further to phenomena that are too slow or too fast for the human eye, including, in principle, flash testing.

Acknowledgment

The authors would like to thank F. Szadkowski, M. Armstrong, and M. Swinton of the Canadian Centre for Housing Technology at Natural Resources Canada for scientific and field support.

References

[1] J. E. Haysom, O. Jafarieh, H. Anis, and K. Hinzer, "Concentrated photovoltaics system costs and learning curve analysis," *AIP Conf. Proc.*, vol. 1556, pp. 239–243, 2013.

[2] S. Kurtz, "Opportunities and challenges for development of a mature concentrating photovoltaic power industry," Nat. Renewable Energy Lab., Golden, CO, USA, Tech. Rep., NREL(TP-520–43208 1556, 2013.

[3] D. J. Friedman, R. R. King, R. M. Swanson, J. McJannet, and D. Gwinner, "Editorial: Toward 100 gigawatts of concentrator photovoltaics by 2030," *IEEE J. Photovoltaics*, vol. 3, no. 4, pp. 1460–1463, Oct. 2013.

[4] K. Brankera, M. J. M. Pathaka, and J. M. Pearce, "A review of solar photovoltaic levelized cost of electricity," *Renewable Sustainable Energy Rev.*, vol. 15, no. 9, pp. 4470–4482, 2011.

[5] V. M. Fthenakis and H. C. Kim, "Photovoltaics: Life-cycle analyses," *Sol. Energy*, vol. 85, no. 8, pp. 1609–1628, 2011.

[6] W. E. Deming, *Out of Crisis*. Cambridge, MA, USA: MIT Press, 2000.

[7] J. M. Juran, *Juran on Planning for Quality*. New York, NY, USA: Collier-Macmillan, 1993.

[8] A. F. Sherwani, J. A. Usmani, and Varun, "Life cycle assessment of solar PV based electricity generation systems: A review," *Renewable Sustainable Energy Rev.*, vol. 14, no. 1, pp. 540–544, 2010.

[9] J. H. Wohlgemuth, D. W. Cunningham, P. Monus, J. Miller, and A. Nguyen, "Long term reliability of photovoltaic modules," in *Proc. IEEE 4th World Conf. Photovoltaic Energy Convers.*, May 2006, pp. 2050–2053.

[10] S. Kurtz, J. Granatab, and M. Quintana, "Photovoltaic-reliability R&D toward a solar-powered world," *Proc. SPIE*, vol. 7412, pp. 1–12, Aug. 2009.

[11] F. J. Vorster and E. E. van Dyk, "Current-voltage characteristics of high-concentration, photovoltaic arrays," *Prog. Photovoltaics: Res. Appl.*, vol. 13, no. 1, pp. 55–66, 2005.

[12] K. Emery, "Measurement and characterization of solar cells and modules," in *Handbook of Photovoltaic Science and Engineering*. New York, NY, USA: Wiley, 2003.

[13] C. R. Osterwald, "Standards, calibration and testing of PV modules and solar cells," in *Practical Handbook of Photovoltaics: Fundamentals and Applications*. New York, NY, USA: Elsevier, 2003.

[14] E. Duran, M. Piliougine, M. Sidrach-de-Cardona, J. Galan, and J. M. Andujar, "Different methods to obtain the I-V curve of PV modules: A review," in *Proc. 33rd IEEE Photovoltaic Spec. Conf.*, May 2008, pp. 1–6.

[15] M. Piliougine, J. Carretero, L. Mora-López, and M. Sidrach-de-Cardona, "Experimental system for current voltage curve measurement of photovoltaic modules under outdoor conditions," *Prog. Photovoltaics: Res. Appl.*, vol. 19, no. 5, pp. 591–602, 2011.

[16] M. D. Yandt, J. F. Wheeldon, J. P. D. Cook, R. Beal, A. W. Walker, O. Thériault, H. Schriemer, T. J. Hall, and K. Hinzer, "Estimating cell temperature in a concentrating photovoltaic system," *AIP Conf. Proc.*, vol. 1477, pp. 172–175, 2012.

[17] C. G. Zimmermann, "Thermal runaway in multijunction solar cells," *Appl. Phys. Lett.*, vol. 102, no. 23, pp. 233506-1–233506-4, 2013.

[18] N. G. Dherea, N. Shiradkara, E. Schnellera, and V. Gade, "The reliability of bypass diodes in PV modules," *Proc. SPIE*, vol. 88250I, pp. 1–8, Aug. 2013.

[19] M. Steiner, G. Siefer, and A. W. Bett, "Modeling the thermal runaway effect in CPV modules," *AIP Conf. Proc.*, vol. 1556, pp. 230–233, 2013.

[20] J. P. D. Cook, M. D. Yandt, M. Kelly, J. F. Wheeldon, K. Hinzer, and H. Schriemer, "Shutter array technique for real-time non-invasive extraction of individual channel responses in multi-channel CPV modules," *Proc. SPIE*, vol. 8915, pp. 891509-1–891509-8, Jun. 2013.

[21] N. Bosco, T. J. Silverman, and S. Kurtz, "Modeling thermal fatigue in CPV cell assemblies," *IEEE J. Photovoltaics*, vol. 1, no. 2, pp. 242–247, Oct. 2011.

[22] M. Vivar, R. Herrero, I. Antón, F. Martínez-Moreno, R. Moretón, G. Sala, A. W. Blakers, and J. Smeltink, "Effect of soiling in CPV systems," *Sol. Energy*, vol. 84, no. 7, pp. 1327–1335, 2010.

[23] A. Massi Pavan, A. Mellit, and D. De Pieri, "The effect of soiling on energy production for large-scale photovoltaic plants," *Sol. Energy*, vol. 85, no. 5, pp. 1128–1136, 2011.

[24] M. García, L. Marroyo, E. Lorenzo, and M. Pérez, "Soiling and other optical losses in solar-tracking PV plants in Navarra," *Prog. Photovoltaic: Res. Appl.*, vol. 19, no. 2, pp. 211–217, 2011.

[25] E. L. Meyer and E. E. van Dyk, "Assessing the reliability and degradation of photovoltaic module performance parameters," *IEEE Trans. Reliab.*, vol. 53, no. 1, pp. 83–92, Mar. 2004.

[26] Y. Hishikawa, H. Shimura, and H. Tobita, "Accurate I-V curve measurements of high-capacity c-si solar cells: Effects of I-V testers and new technology for rapid measurement," in *Proc. 28th Eur. Photovoltaic Sol. Energy Conf.*, 2013, pp. 3159–3161.

[27] C. Monokroussos, R. Gottschalg, A. N. Tiwari, G. Friesen, D. Chianese, and S. Mau, "The effects of solar cell capacitance on calibration accuracy when using a flash simulator," in *Proc. IEEE Photovoltaic Energy Convers.*, 2006, pp. 2231–2234.

[28] T. Chayavanich, C. Limsakul, N. Chayavanich, D. Chenvidhya, C. Jivacate, and K. Kirtikara, "Describing dynamic behavior of static IV characteristics of PV modules using dynamic impedance," in *Proc. 21st Eur. Photovoltaic Sol. Energy Conf.*, Sep. 2006, pp. 2464–2465.

[29] F. W. Grover, *Inductance Calculations*. New York, NY, USA: Dover, 2004.

[30] A. B. Maish, "PV concentrator array field performance measurement," *Sol. Cells*, vol. 18, no. 3–4, pp. 363–371, 1986.

[31] H. Mousazadeha, A. Keyhani, A. Javadi, H. Mobli, K. Abriniac, and A. Sharib, "A review of principle and sun-tracking methods for maximizing solar systems output," *Renewable Sustainable Energy Rev.*, vol. 13, no. 8, pp. 1800–1818, 2009.

[32] C. Algora, "Reliability of III–V concentrator solar cells," *Microelectron. Reliab.*, vol. 50, no. 9–11, pp. 1193–1198, 2010.

Mark D. Yandt received the B.Eng.Mgt. degree in engineering physics and management from McMaster University, Hamilton, ON, Canada, and the M.A.Sc. degree in electrical and computer engineering from the University of Ottawa, Ottawa, ON, and is currently working toward the Ph.D. degree with the School of Electrical Engineering and Computer Science, University of Ottawa, studying under K. Hinzer and H. Schriemer.

His research interests include the development, characterization, optimization, and deployment of photovoltaic and concentrating photovoltaic systems. He oversees experimental design and system characterization for a number of projects at the Sunlab that involve the dynamics and reliability of high-concentration photovoltaic systems.

Mr. Yandt received an Ontario Graduate Scholarship (OGS) in 2011 and the Alexander Graham Bell Canada Graduate Scholarship (CGS-D) funded by the Natural Sciences and Engineering Research Council of Canada in 2012.

John P. D. Cook received the B.Sc. degree in chemistry from McGill University, Montreal, QC, Canada, and the Ph.D. degree from the University of British Columbia, Vancouver, BC, Canada, supported by the Killam Predoctoral Scholarship.

He received a Natural Sciences and Engineering Research Council of Canada Overseas Postdoctoral Fellowship to continue studies in electron spectroscopy at the Flinders University of South Australia (1981–1983), achieving the first binary (e, 2e) results on free radical and relativistic molecular targets. He joined Bell-Northern Research in 1984 and began work on characterizing III–V compound semiconductor optoelectronic materials and devices with the Advanced Technology Laboratory, later moving into wafer process development and reliability studies for optical fiber access devices at Nortel Networks, including high-speed photodiodes, integrated laser/back-facet-monitor devices, and high-speed electronics, in scientist and manager roles. In 2006, he began concentrator photovoltaic module development in private industry, and in 2010, he joined Sunlab, the University of Ottawa, Ottawa, ON, Canada, as a Research Associate. His recent work has been supported by the National Science and Engineering Research Council of Canada, Ontario Centers of Excellence, the University of Ottawa, and several industrial partners.

Michael Kelly received the B.A.Sc. degree in electrical engineering from the University of Ottawa, Ottawa, ON, Canada.

He is currently an RF Hardware Engineer at Ericsson Canada, Inc., where he works in the wireless communication department. He had a summer position with the Sunlab in 2013, where he worked closely with M. Yandt on the modeling of electric-circuit parasitic dynamics during the characterization of high-efficiency photovoltaic systems. He went on to complete an award winning undergraduate project in partnership with the Sunlab in which he developed a new test station capable of probing internal cell dynamics.

Henry Schriemer (M'00) received the B.Sc. degree in mathematics and the Ph.D. degree in physics from the University of Manitoba, Winnipeg, MB, Canada, in 1987 and 1997, respectively.

He is currently an Associate Professor of electrical engineering with the University of Ottawa, Ottawa, ON, Canada, where he previously held an NCIT Research Fellowship in photonics from 2003 to 2005. His research interests include engineered complex systems, with a focus on photonic technologies for energy efficiency. His current activities range from the modeling of multijunction concentrator solar cells and systems, reliability studies and accelerated aging, the development of spectral models that incorporate local weather conditions, and the impact of variable generation on the electrical distribution system. Prior to this, he spent several years in the photonics industry, where he is recognized as one of the innovators of strain-engineered planar lightwave circuits. His previous research accomplishments have ranged from the description of optical singularities in photonic crystals to fundamental advances in the design and realization of laterally coupled-distributed feedback lasers. He has authored more than 70 refereed publications. He held a Postdoctoral Fellowship in laser physics and nanophotonics with the Van der Waals-Zeeman Institute, Amsterdam, The Netherlands, where he made the first measurements of significant spontaneous emission inhibition in active photonic crystals.

Karin Hinzer (M'08) received the B.Sc., M.Sc., and Ph.D. degrees in physics from the University of Ottawa, Ottawa, ON, Canada, in 1996, 1998, and 2002, respectively.

She is currently an Associate Professor and the Canada Research Chair in photonic nanostructures and integrated devices and an Associate Professor with the School of Electrical Engineering and Computer Science, University of Ottawa. She has made pioneering contributions to the experimental physics of quantum dots marked by two landmark papers in *Science*. She gained extensive experience in the design and fabrication of group III-V semiconductor devices while with the National Research Council Canada, Nortel Networks, and Bookham. Cost-reduction strategies and liaison with remote fabrication facilities strongly feature in her industry experience. She joined the University of Ottawa in 2007, where she is the founder of the Sunlab, which is a modeling and characterization laboratory specializing in the development of high-efficiency solar cells. Since the laboratory's inception, she has trained more than 80 highly qualified personnel in the field of photovoltaic system and devices. Since 2010, she has been with the Inorganic Photovoltaics Cotheme Leader within the Pan-Canadian Photovoltaic Research Network.

Dr. Hinzer received the Inaugural Canadian Energy Award, with industry partner Morgan Solar, for the development of more efficient solar panels, in 2010.

3.2 Shutter Technique for Noninvasive Individual Cell Characterization

3.2.1 Scope and Impact

This publication explains the value of a shuttering technique used to optically probe selected cells inside sealed commercial modules. When bypass diodes are present, as they are in most CPV systems, the selective illumination of some solar cells while shading (or shuttering) others, separates their I-V characteristics allowing electrical measurements of those cells to be distinguished from the module I-V characteristics.

This was the first time that such a technique had been recommended as a versatile tool for any CPV system fitted with bypass diodes. The main advantage of this technique is that it circumvents the need to cut into sealed commercial modules to perform individual solar cell level electrical diagnostics. Normally, the need for electrical characteristics at any scale smaller than the module level would require the removal of a module from its array, dismounting from a tracker, and relocation of the module to a laboratory environment where careful dismantling of the module can be performed. Such an investigation rarely culminates in the reinstallation of the same module and as such ongoing observation of the module in question is halted. The shutter technique described in the following paper allows root cause analysis to be performed in situ, by connecting an I-V curve measurement system to a whole module. Instead of moving the module to a laboratory, measurements are made by temporarily disconnecting it from the rest of the array via its existing MC4 (or similar) connectors, while it remains on its tracker and on-sun. The module is simply reconnected when the necessary electrical measurements have been recorded and it can continue to produce power within its array.

3.2.2 Author Contributions

Mark Yandt: The scientific contributions in this manuscript are entirely my own but were supported, guided or encouraged at times by the other authors. The primary contribution is the demonstration of shuttering patterns that allow cell-specific parasitics to be identified and measured. Supporting contributions include the demonstration that fitting algorithms can be used to completely deconvolve individual cell characteristics from shutter measurements of entire moduls.

Dr. John P. D. Cook: John designed the first module sized implementation of the simple shutter frame that we used to make shutter measurements so that we could more efficiently implement the shuttering concept in the field. During measurements John would often help me flip the shutters as I made measurements using the live I-V test station presented in Section 3.1.

Dr. Karin Hinzer: As my co-supervisor and the principal researcher on the grant funding the work I performed, Karin guided the direction of the research and assisted in the editing of the final manuscript.

Dr. Henry Schriemer: As my co-supervisor and a researcher listed on the grant funding the work I performed, Henry guided the direction of the research and assisted in the editing of the final manuscript.

3.2.3 Publication

Paper attached as-published on next page. This paper entitled, “Shutter technique for noninvasive individual cell characterization in sealed CPV modules” was published in March of 2015.

M. D. Yandt, J. P. D. Cook, K. Hinzer, H. Schriemer, “Shutter technique for noninvasive individual cell characterization in sealed CPV modules”, IEEE J. Photovoltaics 5 (2), 691-696, (2015). Doi: 10.1109/JPHOTOV.2015.2392943

Shutter Technique for Noninvasive Individual Cell Characterization in Sealed CPV Modules

Mark D. Yandt, John P. D. Cook, Karin Hinzer, *Member, IEEE*, and Henry Schriemer, *Member, IEEE*

***Abstract*—An optical shutter technique for quality control and degradation analysis of concentrating photovoltaic (CPV) modules is presented. Shuttering configurations are described and used to determine individual component degradation or failure in field-exposed commercial modules. Cells are shuttered in specific patterns, intentionally engaging internal bypass diodes, and current–voltage (*I–V*) curves are measured at the housing terminals of the sealed module. Individual cell characteristics may be qualitatively determined by contrasting module *I–V* responses to different shutter configurations and quantitatively determined by fitting an extended equivalent circuit model to the shutter data.**

***Index Terms*—Bypass diode, component failure analysis, concentrator photovoltaic, concentrated photovoltaic (CPV) field testing, CPV module testing, *I–V* measurement, optical shutter array.**

I. Introduction

THE marketability of concentrated photovoltaic (CPV) systems depends not only on price but on demonstrated reliability as well [1]. To that end, assessing system performance over time to identify root causes of degraded power output is essential to validate this innovative technology in the competitive energy marketplace. It is a basic tenet of failure analysis to perform nondestructive testing whenever possible. However, CPV modules are often fabricated in arrays of channels that are optically in parallel and electrically in series and sealed inside weatherproof housings; all channels are optically accessible, but there are only two terminals for electrical access to all cells. While testing of individual components before module assembly is standard practice, after assembly and in subsequent field deployment, there has been no general technique to access, for example, individual channel and cell performance. We report a shutter technique that facilitates the isolation of individual cell electrical response within a sealed CPV module. This is achieved by optically masking the other cells in the series string before measuring a current–voltage (*I–V*) curve at the module terminals using an *I–V* test station. A dynamic real-time *I–V* test station that shows a live picture of the *I–V* curve, such as that described in [2], is extremely valuable in this context. This rapid trouble-shooting method does not require breaking into the wiring of sealed and encapsulated modules, nor dismounting them from their tracker. It allows identification of abnormal individual channels arising from problematic photovoltaic cells, abnormal bypass diodes, individual channel optical misalignments, interconnect issues, parasitic impedances, and thermal issues. We will demonstrate the application of this technique to assess the first two of these concerns.

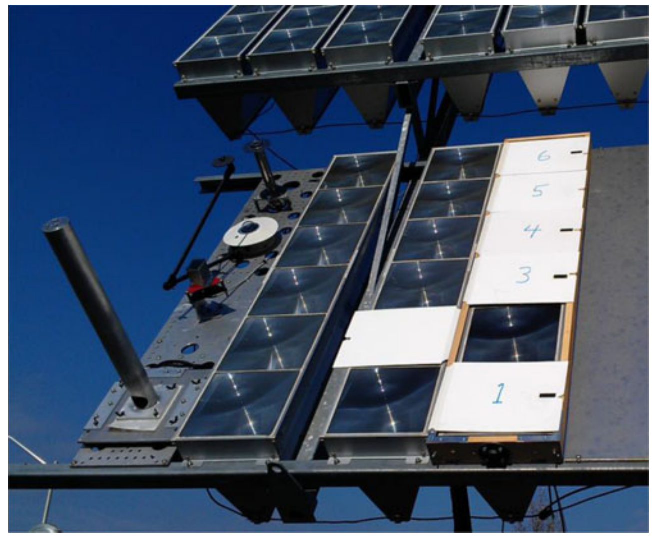

Fig. 1. Six-channel Fresnel-based CPV modules on the SUNLAB SUNRISE tracker [3]. The rightmost module is fitted with shutters designed to allow complete blocking or complete illumination of channels in any combination. Here, only channel 2 is illuminated. Remote shutter operation is not shown.

Fig. 1 shows a number of CPV modules on a fully instrumented tracker [3]. Each module is comprised of a series-connected string of six individual channels (i.e., a triple-junction solar cell with a bypass diode and its two-stage Fresnel concentrating optic). Since an *I–V* measurement across the entire module yields the series sum of the individual cell responses, it can be difficult to diagnose anomalous behavior from the shape of this full-module *I–V* curve. To ascribe anomalous behavior to any particular cell is generally impossible, unless one can deconvolve the individual *I–V* curves by sequentially shading or illuminating individual cells in the module.

Various shading techniques have been used to extract individual cell degradation factors for silicon flat panels, but these required either the removal of the bypass diode [4] (compromising the nondestructive test) or the employment of partial shading to avoid voltage shunts [5]. Bypass diodes protect

Manuscript received October 20, 2014; revised December 12, 2014; accepted January 7, 2015. This work was supported by the Canadian Centre for Housing Technology at Natural Resources Canada, the Natural Sciences and Engineering Research Council of Canada, the National Research Council of Canada, and the Business Development Bank of Canada.

M. D. Yandt is with the Department of Electrical and Computer Engineering, SUNLAB, University of Ottawa, Ottawa, ON K1N 6N5, Canada (e-mail: markyandt@gmail.com).

J. P. D. Cook, K. Hinzer, and H. Schriemer are with the SUNLAB, University of Ottawa, Ottawa, ON K1N 6N5, Canada (e-mail: jpdcook@magma.ca; khinzer@uottawa.ca; hschriemer@uottawa.ca).

Color versions of one or more of the figures in this paper are available online at http://ieeexplore.ieee.org.

Digital Object Identifier 10.1109/JPHOTOV.2015.2392943

TABLE I
IDENTIFIABLE PATHOLOGIES

Module Name	Shutter Configuration	Observable Pathologies
Module A (see Fig. 2)	"Progressive-shuttered"	Model verification (All ideal parameters describing the fully functional module)
Module B (see Fig. 4)	"Single-open"	Individual shunt resistances (R_{shunt}) & Individual series resistances (R_{series})
Module C (see Fig. 6)	"Single-closed"	Individual shunt resistances (R_{shunt}) & Individual diode resistances (R_{diode})

Summary of shutter configurations and the reasons they are used.

low-current-producing cells from experiencing large reverse bias by allowing current from higher producing cells to flow around them with only a small potential drop. Module behavior with bypass diodes under partial shading conditions is well understood [6]–[13], and CPV modules are often equipped with a bypass diode around each cell. This allows CPV channels to operate nearly independently, and thus, we may exploit this fact, deliberately engaging them in order to isolate individual cell characteristics.

II. SHUTTER TECHNIQUE

One of many possible shutter configurations is shown in Fig. 1. This simple, inexpensive, portable design consists of opaque panels ("shutters") hinged on a frame that supports the shutters in registration with the Fresnel lens array. The shutters completely occult the primary optics and can be remotely operated. The shutter technique then consists of comparing the system *I–V* responses when successive optical channels are shuttered or, conversely, when successive channels are unshuttered.

We use the term "shuttered" to describe the artificial shading of channels in a CPV module with these opaque panels and define terms for various sets of shutter pattern combinations as follows:

1) "full-open," where all shutters are open;
2) "full-closed," where all shutters are closed;
3) "progressive-shuttered," starting from "full-open" and closing shutters one at a time in succession until "full-closed" is reached, whereupon the module dark *I–V* curve can be measured (we use the term "partial shutter" to refer to an individual shutter which is part way open);
4) "single-open," where all shutters but one are closed, in which the module essentially behaves as a single photodiode in series with five bypass diodes;
5) "single-closed," where all shutters but one are open.

Before attempting to understand the *I–V* response of a degraded module, we first study a fully functional module. Table I lists the pathologies that these shutter combinations identify. Before attempting to understand the *I–V* response of a degraded module, we first study a fully functional module. Fig. 2 shows a set of "progressive-shutter" measurements made on a fully functional module (Module A). Corresponding simulation results derived from a calibrated equivalent circuit model [14] of the six different shuttering conditions are also shown. System voltage is reduced in regular increments as the *I–V* curve moves stepwise to the left under progressive shuttering. There is no hysteresis in shutter operating order: The complementary view has the *I–V* response arising out of the dark *I–V* curve as cells are progressively unshuttered, stepwise to the right, and the same response is obtained for the same combination of shutters.

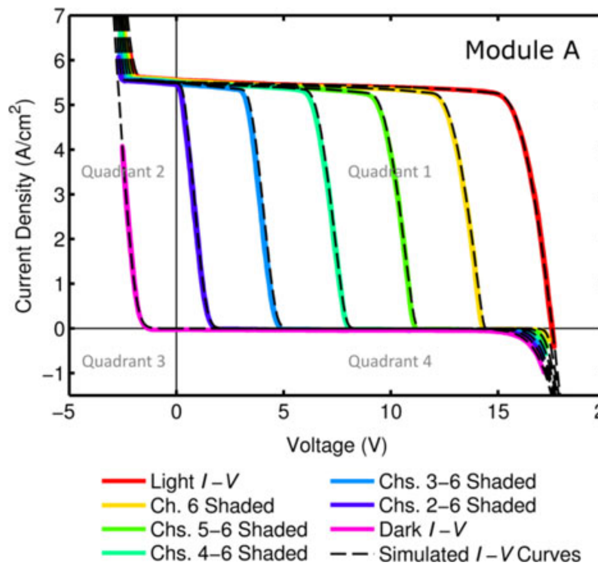

Fig. 2. "Progressive shutter" measurements on Module A demonstrating full functionality. Simulation results for the various shuttered conditions are shown with dashed lines.

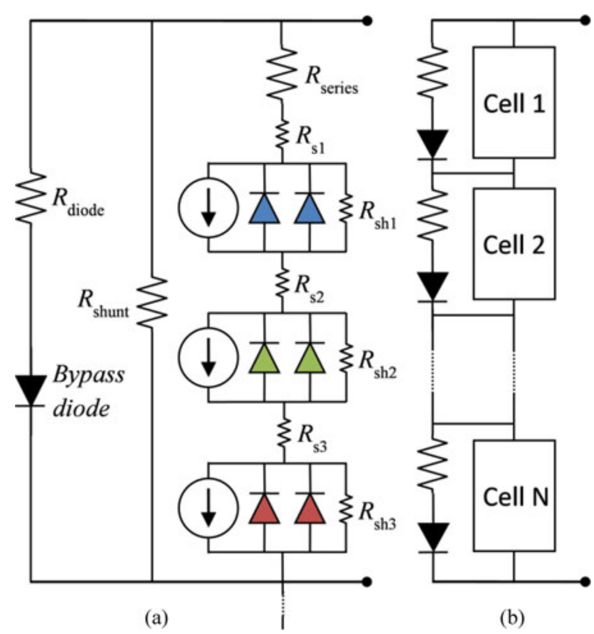

Fig. 3. (a) Equivalent circuit model for a single triple-junction solar cell with two diodes for each subcell. (b) Equivalent circuit model for a module composed of *N* series-connected cells with individual bypass diodes.

Fig. 3 illustrates the equivalent circuit model that is fitted to the shutter measurements. This extended model incorporates a two-diode model [15] for each subcell, with associated series and shunt resistances, as shown in Fig. 3(a); the full model for the module has all $N = 6$ CPV cells, each with its bypass diode, as seen in Fig. 3(b). The modeling parameters extracted from

TABLE II
MODULE MODEL FIT RESULTS

Module Name	Shutter Configuration	Fitted Parameters
Module A (see Fig. 2)	"Progressive-shuttered"	$R_{\rm shunt} > 50\ \Omega$ $R_{\rm diode} < 0.025\ \Omega$ $R_{\rm series} < 0.025\ \Omega$
Module B (see Fig. 4)	"Single-open"	$R_{\rm shunt} = 0.25$, 15, 0.23 and 3 Ω for cells 1, 3, 4, and 5, respectively, $R_{\rm diode} < 0.025\ \Omega$ $R_{\rm series} < 0.025\ \Omega$
Module C (see Fig. 6)	"Single-closed"	$R_{\rm shunt} = 6$, 0.32 and 0.26 Ω for cells 2, 3, and 5, respectively, $R_{\rm diode} = 0.58$, 0.75, >0.32, 0.40, >0.26 and 0.06 Ω, for cells 1, 2, 3, 4, 5, and 6, respectively, $R_{\rm series} < 0.025\ \Omega$

Summary of shutter configurations and extracted parameters.

fits of the model to the various shutter measurements allow individual cell responses to be reconstructed, with parameter magnitudes identifying the origins of anomalous cell behavior: $R_{\rm series}$, $R_{\rm shunt}$, and $R_{\rm diode}$ were the relevant fitting parameters as shown in Table II. $R_{\rm series}$ quantifies electrical contact through the slope of the shutter measurement between the maximum power point and $V_{\rm OC}$. $R_{\rm shunt}$ quantifies leakage currents (shunts) around either cell or bypass diode by the slope of the line between the bypass turn-on and the maximum power point. These two parameters for each cell can best be extracted from individually illuminated channels. $R_{\rm diode}$ for each cell must be determined by reversing the shutter pattern and illuminating five cells at a time. This isolates the effect $R_{\rm diode}$ for a single cell between the maximum power point and $V_{\rm OC}$. The well-understood temperature dependences of cell and diode [14], [15] were also included in the model.

The agreement between measurement and simulation shown in Fig. 2 gives us confidence that we understand how the shutter technique behaves on a fully functional module under normal operating conditions. We may thus proceed to more stringent validation and application.

III. TECHNIQUE VALIDATION

To validate the shutter technique, we next apply it to a module with degraded cell response but functioning bypass diodes (Module B). We first extract the individual *I–V* curves from a set of "single-open" shutter measurements, as shown in Fig. 4(a). The "single open" response curves in Fig. 4(a) are very obviously different. The *I–V* curves of cells 1 and 4 do not appear to have a maximum power point knee in their curve at all, while that of cell 5 is somewhat reduced. Cells 2, 3, and 6 appear to be performing well. Dashed curves are fits of the module equivalent circuit model to the shuttered module responses. Table II presents the extracted fitting parameters.

Module B was then opened up, the individual cells isolated electrically, and their *I–V* curves measured. The results are shown by the corresponding colored curves in Fig. 4(b). These curves are overlaid by dashed curves representing the individual cell responses extracted numerically from the fits to the shutter measurements. Agreement between these two results is observed for all curves. The slight differences may be attributed to

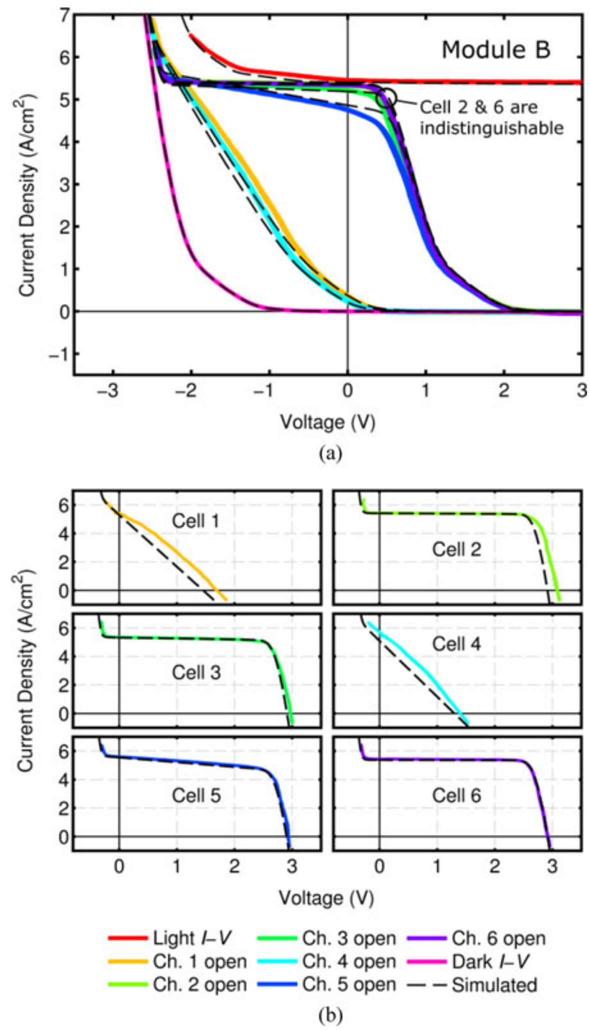

Fig. 4. (a) Set of "single-open" shutter measurements on Module B demonstrating noninvasive isolation of individual cell *I–V* curves. Dashed curves are fits using simulation. (b) Individual cell *I–V* characteristics obtained from fits in (a), compared with direct measurements on the opened module (solid curves). Note that cell 2 and cell 6 have nearly identical performance and thus their curves overlap in (a).

limiting the multiparameter optimization process during fitting and to cell temperature variation during isolated cell measurements. A distributed equivalent circuit model as described in [16] could be used to better fit the shutter measurements if more detailed information is desired. It is seen that cells 1 and 4 are severely shunted and that cell 5 is moderately shunted. A slight shunt is also visible in the cell 3 response. Cells 2 and 6 are well behaved, with the former having slightly higher $V_{\rm OC}$ than the later because the cell had yet to come up to its operating temperature when the direct measurement was taken. Having now established the viability of the approach, we can now proceed to a more stringent application of the shutter technique.

IV. TECHNIQUE APPLICATION

The shutter technique is now applied to a module with degraded cell response caused by malfunctioning bypass behavior (Module C). In Fig. 5, the *I–V* characteristic of Module C is com-

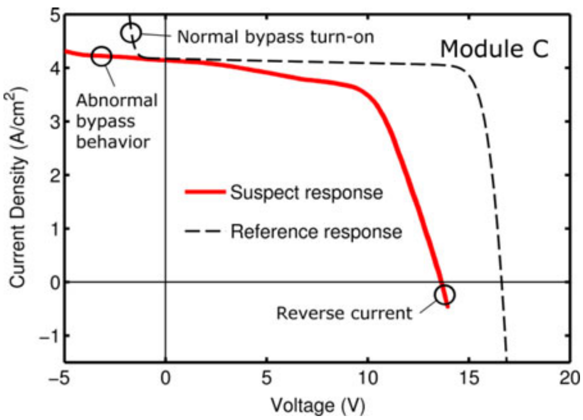

Fig. 5. Characteristic *I–V* curve of Module C compared with reference *I–V* curve simulated for the same ambient conditions. Degradation is apparent, but the reason for the poor module characteristics is not obvious.

pared with the expected *I–V* curve simulated using the equivalent circuit model under the same ambient conditions. Comparison of the two curves shows that Module C has indeed degraded, warranting shutter measurements.

There are two possible issues of concern that should be considered before proceeding with shutter measurements. In quadrant 4, current is able to flow under forward bias greater than V_{OC}, which happens when no cells have failed in open circuits and when no blocking diodes are present. This is important to check because if a cell has failed in open circuit, then any *I–V* measurements, especially of dark *I–V* curves, can produce a dangerously large reverse bias on the bypass diode of the affected receiver. Note that modules with blocking diodes will also prevent reverse current from flowing, yielding an *I–V* curve that is indistinguishable from that of a module with a cell that has failed open.

In quadrant 2, the *I–V* curve of Module C does not show the expected turn-on of the bypass diodes in reverse bias (cf., Fig. 2, Quadrant 2), which suggests bypass diode issues. To isolate the performance of each bypass diode, a "single-closed" *I–V* curve set may be recorded. To ensure that no cell damage is caused when cells with potentially defective bypass diodes are shaded, it is important to first verify that sufficient bypass diode turn-on is visible in quadrant 2, if not in the light *I–V* curve, than in the dark *I–V* curve. If no bypass diode turn-on is observable in the dark *I–V* curve, than at least one disconnected bypass diode is confirmed. The shuttering procedure needed to identify the channel(s) with disconnected bypass diode(s) depend(s) on the module's internal circuit. Bypass diode turn-on is not visible in Fig. 5, but some bypass diode function was confirmed; therefore, the module was put back on sun and each channel was initially partially shuttered by about 5% to lightly engage its bypass diode. In all cases, the diode did permit current to bypass the partially shaded cell; therefore, full shuttering could safely proceed.

Fig. 6(a) shows a set of "single-closed" shutter measurements on Module C, plus the "full-open" and "full-closed" *I–V* curves. As before, dashed curves are fits to the shuttered

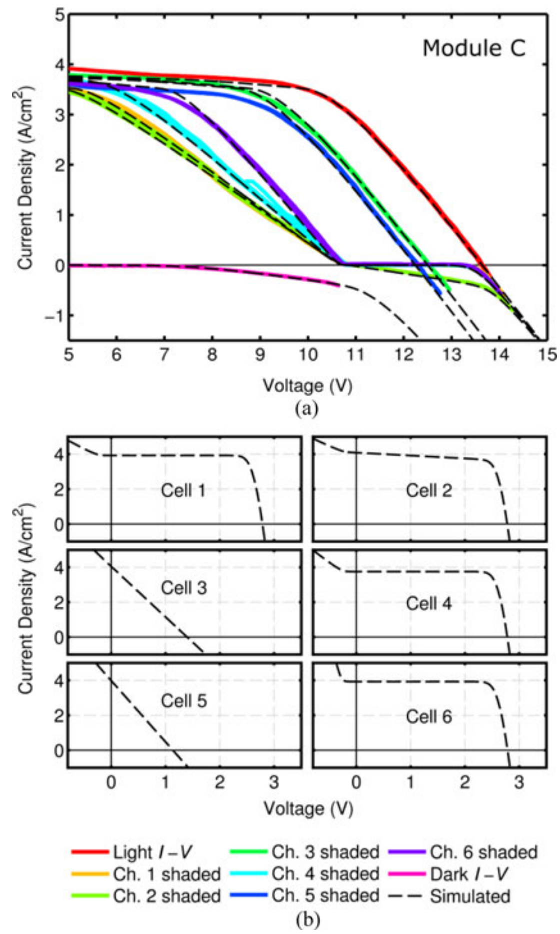

Fig. 6. (a) Set of "single-closed" shutter measurements, including "full-open" and "full-closed," performed on Module C. Dashed lines represent simulated fits to the measurements. (b) Individual cell *I–V* characteristics obtained from fits in (a) more clearly revealing the impact of bypass diode failure modes.

module responses, using the equivalent circuit model, to enable subsequent extraction of individual cell characteristics. Table II presents the extracted fitting parameters.

It is possible to qualitatively extract the individual performance issues of each channel directly from the shutter measurements of Fig. 6(a). For channel 6, the slope of the falling edge of the *I–V* curve (between the MPP and V_{OC}) is similar to that of the light *I–V* curve, and the shift in V_{OC} is as expected, confirming normal behavior. Channels 1, 2, and 4 show the anticipated shifts in V_{OC}, but the falling edge of their *I–V* curves (where their respective bypass diodes are operating) exhibit slopes less than channel 6. This indicates the presence of an abnormal diode resistance, R_{diode}, in series with the parallel bypass diode. It is not in series with the solar cell because the reduced slope only occurs in the portion of the *I–V* curve where the bypass diode is engaged and it does not occur below V_{OC} in the fourth quadrant. In addition, when channel 2 is shuttered, the *I–V* curve immediately below V_{OC} exhibits a bias-dependent reverse current. This is caused by an abnormal shunt resistance in parallel with cell 2. Channels 3 and 5 show an abnormally small leftward shift from the fully illuminated module response and no slope discontinuity at zero current, implying that large shunts exist in parallel with these cells.

Semiquantitative descriptions characterizing the severity of the failure modes may be found from the individual channel responses by fitting the parameterized equivalent circuit model to the shutter measurements of Fig. 6(a). These *I–V* responses, shown in Fig. 6(b), are determined by the same method as described in Section III. They reveal with greater clarity the abnormalities discussed above. Notably, cells 3 and 5 are severely shunted (i.e., their *I–V* curves show a nonzero slope between I_{sc} and the maximum power point), with R_{shunt} values of 0.32 and 0.26 Ω, respectively; cell 2 exhibits a less significant R_{shunt} of 6 Ω. It is also interesting to observe the shape of the reverse-biased portion of the *I–V* curves. Except for cell 6, all the rest of the cells show parasitic bypass behavior (i.e., abnormally weak diode turn-on). Resistances in series with the bypass diodes, R_{diode}, were 0.58, 0.75, 0.40, and 0.06 Ω, for cells 1, 2, 4, and 6, respectively. The *I–V* curves of cells 3 and 5 were too shunted to extract R_{diode} values, but from the shape of the characteristics, we can conclude that these values must be greater than their respective shunt resistances. Subsequent examination of these bypass diodes confirmed that the diodes themselves were still operable but that the component attach bond material between diode and carrier had degraded.

V. Conclusion

A noninvasive technique using a simple, inexpensive, portable shutter frame has been presented, where individual cell responses were measured for sealed modules containing an internal array of series-connected cells with individual bypass diodes. This technique allows localization and identification of specific component and material degradation without reopening modules for spot probing and can be employed either in the field or on the manufacturing floor. Employed in the latter, it would permit infant failures or process issues at the individual cell level to be characterized without damaging the modules and can reduce the need for destructive module investigation.

In the measurements and modeling presented, we compared modules of identical manufacture that exhibit very different illuminated *I–V* characteristics after long field exposure. Two complementary shuttering arrangements were used, depending on which parameters were to be extracted. Sequentially shuttering all but one channel isolated the *I–V* curve of that cell, allowing its series and shunt resistances to be extracted. Conversely, shuttering one channel at a time forced its bypass diode into operation and allowed that particular diode to be analyzed. Shunt resistances for each channel could be extracted from either shuttering arrangement since current flows through a shunt resistance, regardless of whether the channel is operating in forward or reverse bias.

Application of our shutter technique to other module systems requires specific knowledge of their particular series–parallel cell arrangement and bypass/blocking diode configuration. Modules with more cells, for example, often have a combination of internal series and parallel connections, which will result in fully functioning "progressive shuttered" measurements that look different from those shown in Fig. 2. This has an impact on the required capability of the *I–V* test station. If many bypass diodes are in series, the test station will have to measure well into the second quadrant to perform "single open" shutter measurements. To measure "single closed" shutter measurements, the test station must be capable of sinking the on-sun power of the module. While the form of the *I–V* response depends on the specific series–parallel configuration, information similar to that discussed above is generally accessible, even for modules that are quite different from those presented here. However, the presence of blocking diodes may limit access to cell-specific information under certain circumstances, and severely damaged circuit components (like severe shunts) may mask other issues.

Acknowledgment

The authors acknowledge scientific and field support from F. Szadkowski, M. Armstrong, and M. Swinton of the Canadian Centre for Housing Technology at Natural Resources Canada.

References

[1] J. E. Haysom, O. Jafarieh, H. Anis, and K Hinzer, "Concentrated photovoltaics system costs and learning curve analysis," in *Proc. 9th Int. Conf. Concentrator Photovoltaic Syst.*, 2013, vol. 1556, pp. 239–243.

[2] M. D. Yandt, J. P. D. Cook, M. Kelly, H. Schriemer, and K. Hinzer, "Dynamic real-time *I–V* curve measurement system for indoor/outdoor characterization of photovoltaic cells and modules," *IEEE J. Photovoltaics*, vol. 5, no. 1, pp. 321–327, Jan. 2015.

[3] M. D. Yandt, J. F. Wheeldon, C. E. Valdivia, S. Chow, O. Theriault, A. Johnson, F. Szadkowski, M. Zrmstrong, L. Motte, T. Cassidy, I. Sivilla, J. Berrios, S. G. Wallace, S. Fafard, M. Swinton, F. Shepherd, J. Cook, and K. Hinzer, "A new on-sun test facility at the sunrise quantum-dot-enhanced CPV module demonstration system," in *Proc. 7th Int. Conf. Concentrating Photovoltaics Syst.*, 2011, vol. 1407, pp. 224–227.

[4] L. De Bernardez and R. H. Buitrago, "Dark *I–V* curve measurement of single cells in a photovoltaic module," *Prog. Photovoltaic, Res. Appl.*, vol. 14, pp. 321–327, 2006.

[5] G. B. Alers, J. Zhou, C. Deline, P. Hacke, and S. R. Kurtz, "Degradation of individual cells in a module measured with differential *IV* analysis," *Prog. Photovoltaic, Res. Appl.*, vol. 19, pp. 977–982, 2011.

[6] F. J. Vorster, E. E. van Dyk, and A. W. R. Leitch, "Investigation on the *I-V* characteristics of a high concentration photovoltaic array," in *Proc. Conf. Rec. 29th IEEE Photovoltaic Spec. Conf.*, 2002, pp. 1604–1607.

[7] V. Quaschning and R. Hanitsch, "Numerical simulation of current-voltage characteristics of photovoltaic systems with shaded solar cells," *Solar Energy*, vol. 56, no. 6, pp. 513–520, 1996.

[8] A. Dolara, G. C. Lazaroiu, S. Leva, and G. Manzolini, "Experimental investigation of partial shading scenarios on PV (photovoltaic) modules," *Energy*, vol. 55, pp. 466–475, 2013.

[9] F. J. Vorster and E. E. van Dyk, "Current-voltage characteristics of high-concentration photovoltaic arrays," *Prog. Photovoltaics, Res. Appl.*, vol. 13, pp. 55–66, 2005.

[10] E. Karatepe, M. Boztepe, and M. Colak, "Development of a suitable model for characterizing photovoltaic arrays with shaded solar cells," *Sol. Energy*, vol. 81, pp. 977–992, 2007.

[11] A. B. Or and J. Appelbaum, "Performance analysis of concentrator photovoltaic dense-arrays under non-uniform irradiance," *Sol. Energy Mater. Sol. Cells*, vol. 117, pp. 110–119, 2013.

[12] T. Cooper, M. Pravettoni, M. Cadruvi, G. Ambrosetti, and A. Steinfeid, "The effect of irradiance mismatch on a semi-dense array of triple-junction concentrator cells," *Sol. Energy Mater. Sol. Cells*, vol. 116, pp. 238–251, 2013.

[13] J. W. Bishop, "Computer simulation of the effects of electrical mismatches in photovoltaic cell interconnection circuits," *Sol. Cells*, vol. 25, pp. 73–89, 1988.

[14] M. D. Yandt, J. F. Wheeldon, J. P. D. Cook, R. Beal, A. W. Walker, O. Thériault, H. Schriemer, T. J. Hall, and K. Hinzer, "Estimating cell temperature in a concentrating photovoltaic system," in *Proc. 8th Int. Conf. Concentrator Photovoltaic Syst.*, vol. 1477, pp. 172–175, 2012.

[15] Y. Sakurada and Y Ota, "Simulation of temperature characteristics of InGaP/InGaAs/Ge triple-junction solar cell under concentrated light," *Jpn. J. Appl. Phys.*, vol. 50, no. 4, p. 04DP13, 2011.

[16] P. Sharma, A. W. Walker, J. F. Wheeldon, K. Hinzer, and H. Schriemer, "Enhanced efficiencies for high-concentration, multijunction PV systems by optimizing grid spacing under nonuniform illumination using a distributed resistance model," *Int. J. Photoenergy*, vol. 2014, p. 582083, 2014.

Mark D. Yandt received the B.Eng.Mgt. degree in engineering physics and management from McMaster University, Hamilton, ON, Canada, and the M.A.Sc. degree in electrical and computer engineering from the University of Ottawa, Ottawa, ON, where he is currently working toward the Ph.D. degree with the School of Electrical Engineering and Computer Science, studying under K. Hinzer and H. Schriemer.

His research interests include the development, characterization, optimization, and deployment of photovoltaic and concentrating photovoltaic systems. He oversees experimental design and system characterization for a number of projects at the Sunlab that involve the dynamics and reliability of high-concentration photovoltaic systems.

Dr. Yandt received an Ontario Graduate Scholarship in 2011 and the Alexander Graham Bell Canada Graduate Scholarship (CGS-D), funded by the Natural Sciences and Engineering Research Council of Canada, in 2012.

John P. D. Cook received the B.Sc. degree in chemistry from McGill University, Montreal, QC, Canada, and the Ph.D. degree from the University of British Columbia, Vancouver, BC, Canada, supported by the Killam Predoctoral Scholarship.

He received a Natural Sciences and Engineering Research Council of Canada Overseas Postdoctoral Fellowship to continue studies in electron spectroscopy with the Flinders University of South Australia (1981–1983), achieving the first binary (e, 2e) results on free radical and relativistic molecular targets. He joined Bell-Northern Research in 1984 and began work on characterizing III–V compound semiconductor optoelectronic materials and devices with the Advanced Technology Laboratory, later moving into wafer process development and reliability studies for optical fiber access devices at Nortel Networks, including high-speed photodiodes, integrated laser/back-facet-monitor devices, and high-speed electronics, in scientist and manager roles. In 2006, he began concentrator photovoltaic module development in private industry, and in 2010, he joined Sunlab, the University of Ottawa, Ottawa, ON, Canada, as a Research Associate. His recent work has been supported by the National Science and Engineering Research Council of Canada, Ontario Centers of Excellence, the University of Ottawa, and several industrial partners.

Karin Hinzer (M'08) received the B.Sc., M.Sc., and Ph.D. degrees in physics from the University of Ottawa, Ottawa, ON, Canada, in 1996, 1998, and 2002, respectively.

She is currently an Associate Professor and the Canada Research Chair in photonic nanostructures and integrated devices and an Associate Professor with the School of Electrical Engineering and Computer Science, University of Ottawa. She has made pioneering contributions to the experimental physics of quantum dots marked by two landmark papers in *Science*. She gained extensive experience in the design and fabrication of group III–V semiconductor devices while with the National Research Council Canada, Nortel Networks, and Bookham. Cost-reduction strategies and liaison with remote fabrication facilities strongly feature in her industry experience. She joined the University of Ottawa in 2007, where she is the Founder of the Sunlab, which is a modeling and characterization laboratory specializing in the development of high-efficiency solar cells. Since the laboratory's inception, she has trained more than 80 highly qualified personnel in the field of photovoltaic system and devices. Since 2010, she has been with the Inorganic Photovoltaics Cotheme Leader within the Pan-Canadian Photovoltaic Research Network.

Dr. Hinzer received the Inaugural Canadian Energy Award, with industry partner Morgan Solar, for the development of more efficient solar panels in 2010.

Henry Schriemer (M'00) received the B.Sc. degree in mathematics and the Ph.D. degree in physics from the University of Manitoba, Winnipeg, MB, Canada, in 1987 and 1997, respectively.

He is currently an Associate Professor of electrical engineering with the University of Ottawa, Ottawa, ON, Canada, where he previously held an NCIT Research Fellowship in photonics from 2003 to 2005. His research interests include engineered complex systems, with a focus on photonic technologies for energy efficiency. His current activities range from the modeling of multijunction concentrator solar cells and systems, reliability studies and accelerated aging, the development of spectral models that incorporate local weather conditions, and the impact of variable generation on the electrical distribution system. Prior to this, he spent several years in the photonics industry, where he is recognized as one of the innovators of strain-engineered planar lightwave circuits. His previous research accomplishments have ranged from the description of optical singularities in photonic crystals to fundamental advances in the design and realization of laterally coupled-distributed feedback lasers. He has authored more than 70 refereed publications. He held a Postdoctoral Fellowship in laser physics and nanophotonics with the Van der Waals-Zeeman Institute, Amsterdam, The Netherlands, where he made the first measurements of significant spontaneous emission inhibition in active photonic crystals.

4 Multi-Junction Solar Cell Bandgap Optimization

4.1 Efficient MJSC Design for Max. Annual EY by Representative Spectrum Selection

4.1.1 Scope and Impact

There has been much work done to relax lattice matching constraints and develop manufacturing processes that allow more ideal bandgap combinations to be realized in multi-junctions solar cells. Techniques include the incorporation of nitrides, quantum wells, quantum dots, porosification and/or wafer bonding. This energy is invested because there is clear benefit to increasing the number of subcells, or better positioning their bandgap energies, leading to reduced thermalization and transmission losses which impose fundamental limits on cell efficiency. This added manufacturing flexibility relaxes some of the constraints that cell designers must work within, allowing 3, 4, 5, and even 6 junction solar cells to be conceived. It also broadens the design space that traditional triple junction solar cells have been confined to.

As CPV companies attempt to maximize the value of their systems, they attempt to maximize the energy yield their system produces while minimizing cost. However, choosing bandgap combinations that take full advantage of state of the art cell manufacturing processes is a complex multidimensional optimization problem involving fluctuating ambient conditions that vary geographically. It is not trivial to determine the bandgap combination that will maximize annual energy yield even if there are no manufacturing constraints and as a result this topic is of interest to some of the Sunlab's industrial partners. This paper addresses this optimization problem in a systematic fashion taking full advantage of the traditional approach to bandgap selection in which conversion efficiency of a particular representative spectrum is prioritized. The approach presented relies of a number of measured approximations to shorten the length of time it takes to perform energy yield calculations and thus compare design alternatives according to their modeled annual energy yield. The sensitivity of annual energy yield to the design point is investigated and the results are compared to conventional optimization schemes.

4.1.2 Author Contributions

Mark Yandt: The scientific contributions in this manuscript are entirely my own but were supported, guided or encouraged at times by the other authors. The primary contribution is the method by which systematic determination of the optimal bandgap combinations can be determined as a function of latitude. The results are then compared to standard approached of estimating optimal cell designs in the industry and their effectiveness is quantified under clear sky conditions.

Dr. Karin Hinzer: As my co-supervisor and the principal researcher on the grant funding the work I performed, Karin guided the direction of the research and assisted in the editing of the final manuscript.

Dr. Henry Schriemer: As my co-supervisor and a researcher listed on the grant funding the work I performed, Henry guided the direction of the research and assisted in the editing of the final manuscript.

4.1.3 Publication

Paper attached on next page. This paper was accepted for publication on July 6th and a revision of the paper was resubmitted having addressed the reviewer’s comments on July 27th, 2016.

Efficient Multijunction Solar Cell Design for Maximum Annual Energy Yield by Representative Spectrum Selection

Mark D. Yandt, Karin Hinzer, *Member, IEEE*, and Henry Schriemer, *Member, IEEE*

***Abstract*—We describe a systematic approach to multijunction solar cell (MJSC) design that unambiguously identifies the spectrum to be used in cell optimization such that local annual energy yield is maximized. A set of candidate spectra is generated from air mass (AM) values ranging from AM1d to AM5d. Each candidate spectrum is used to find the bandgap combination that maximizes cell efficiency and its energy yield is then calculated using an efficient data reduction approach. The bandgap combination that maximizes annual energy yield identifies the representative spectrum. We do this for cells with up to eight junctions across all clear-sky latitudes and compare our results to other cell optimization approaches. Our representative spectrum selection (RSS) approach is robust and highly tolerant of variations in latitude, particularly when compared to the standard AM1.5d approach which, at midlatitudes, cannot be used without suffering an increasingly severe yield penalty. Comparison against the 50% cumulative energy AM (50% AM) design approach is enabled by using the same design conditions (sea level and ASTM standard atmosphere) in order to unambiguously associate each 50% AM value with a cell design spectrum. We find that our RSS approach always produces cells with slightly higher annual energy yields than are achieved by the corresponding 50% AM designs. While both approaches show similar yields for devices with few junctions, we find yield enhancements approaching 1% for cell designs with many junctions, emphasizing the need to consider the spectral variability of the local solar resource. This consideration is systematically enabled by our RSS approach, addressing a deficiency in the previous design approaches.**

***Index Terms*—Air mass (AM), annual energy yield, bandgap optimization, elevation, latitude, multijunction solar cell (MJSC), representative spectrum.**

I. Introduction

MULTIJUNCTION solar cells (MJSCs) with >40% efficiency are now common. For those manufacturers who have the processing capability to target very specific junction bandgap combinations [1]–[5], one challenge that remains is to determine performance-maximizing design points, a topic that has received much investigation [6]–[10]. It is well known that combinations that yield record conversion efficiency under standard test conditions (STC: 25 °C with a 1000 W/m^2 ASTM G173-03 AM1.5d spectrum) do not necessarily maximize the net present value of concentrating photovoltaic (CPV) power stations [11]–[13]. As early as 2008, Amonix showed improved annual energy yields when optimizing two junction cells for location-specific air masses (AMs) higher than AM1.5 [14]. Semprius Inc. presented field results in 2015 on systems where modules were optimized for AMs near 2.1, finding broader daily efficiency curves [5]. Later, Garcia *et al.* [15] argued that complete annual spectral datasets need to be available for a site to optimize MJSC design for maximum energy production. Wang and Barnett showed that series connected two terminal 3JSCs may suffer up to 9% more loss than a multiterminal device in which current matching was not a requirement [7]. Chan *et al*. realized the importance of determining a systematic method of determining a representative spectrum for the purpose of accurately predicting energy yield and developed a spectral weighting system to do so [10]. Phillips *et al.* tested several manufacturable cell designs and compared their energy performance to an ideal cell in two interesting locations to determine the penalty paid due to nonideal cell designs [8]. These investigations all speak to the spectral effects that must be taken into consideration but none provide a systematic methodology of determining the broad trends in the ideal cell design as a function of junction number or AM.

Designing to a complete set of spectra is computationally intensive and it does not easily permit the effect of location-specific parameters to be comprehensively assessed. We present a systematic method to identify a design spectrum that defines the optimal MJSC bandgap combination. The method extends the representative spectrum approach, typically used to design cells for maximum efficiency under STC [16], to a selection process for maximizing annual energy yield at any location. We will demonstrate this approach as a function of latitude given a standard set of atmospheric conditions to facilitate comparison to the traditional approaches. Ultimately, however, this process can incorporate existing local datasets to inform the selection of a local representative spectrum.

We begin by choosing a set of well-defined clear sky direct beam spectral candidates. We choose sea-level spectra between air masses AM1d and AM5d as our candidates since these typically span the design space. Each spectral candidate is used to

Manuscript received May 31, 2016; revised July 27, 2016 and October 15, 2016; accepted December 2, 2016. Date of publication January 9, 2017; date of current version February 16, 2017. This work was supported by the Natural Sciences and Engineering Research Council of Canada for funding programs.

M. D. Yandt is with the Department of Electrical and Computer Engineering, Sunlab, University of Ottawa, Ottawa, ON K1N 6N5, Canada (e-mail: markyandt@gmail.com).

K. Hinzer and H. Schriemer are with the Sunlab, University of Ottawa, Ottawa, ON K1N 6N5, Canada (e-mail: khinzer@uottawa.ca; hschriemer@uottawa.ca).

Color versions of one or more of the figures in this paper are available online at http://ieeexplore.ieee.org.

Digital Object Identifier 10.1109/JPHOTOV.2016.2638040

find the bandgaps that maximize its conversion efficiency; using that MJSC, the energy yield is then calculated as the clear sky local solar resource evolves over the year. We then select as the representative spectrum that candidate which gives the highest annual energy yield.

Annual energy yield is computed assuming clear skies and standard atmospheric conditions that are not specific to any location. The AM as a function of time is the only location-specific parameter in this study and is based solely on an input latitude and elevation. While AM is only one of many factors that influence local spectral color balance [17], it is the fastest and most consistently changing spectral condition, and drives the broad trends in the optimization problem. Presently neglecting any other local variation in atmospheric constituents [17], we clearly illustrate the efficacy of our representative spectrum selection (RSS) approach by performing the yield analysis across all latitudes at sea level for MJSC designs with up to eight junctions. These results are then compared against other cell optimization approaches applied with the same assumptions.

Even though local atmospheric conditions are not incorporated in this analysis, we find it useful to illustrate the approach using the latitude and elevation of two real locations, Ottawa, Canada, and Boulder, USA. We, thus, perform the analysis as we would if we were going to take the next step and incorporate local atmospheric conditions. This can be done by specifying locally representative atmospheric constituents and scaling the solar resource as a function of AM to account for cloud cover, but we leave this for future work. For now, we compare the spectral differences in these locations due solely to AM and attempt to systematically quantify the influences of this primary input.

II. Bandgap Optimization

The candidate spectra (direct beam plus circumsolar) were generated using SMARTS2 [18] with the ASTM G173-03 standard input file, changing only the AM. Spectra were simulated at sea level with a pressure of 1013.25 mbar. They were input to a modified version of *mjOpt* [19], which uses an equivalent circuit model (single diode per subcell) within a detailed balance algorithm to determine optimal bandgap combinations for any specified MJSC. *MjOpt* is a revision of *etaOpt*, originally designed by Fraunhofer in Mathematica as an implementation of the detailed balance calculations first published by Shockley and Queisser [20], [21]. Given an input spectrum, *mjOpt* is used to determine the set of bandgaps that maximize the conversion efficiency for each input spectrum. A concentration of 1000× and a cell operating temperature of 60 °C were assumed during bandgap optimization.

Fig. 1 shows the spectral irradiance for three illustrative AM spectra (left axis) on which eight horizontal shaded bands are superimposed, each containing optimal bandgap combinations for the indicated MJSC over the range of AM design values. Within each band, there is a color graduation (from light blue to black) for each subcell that maps the optimized bandgap energy to the AM used for its optimization (right axis color bar). Note that for each AM design value, the set of bandgaps for the most efficient MJSC all have the same color; i.e., they can be

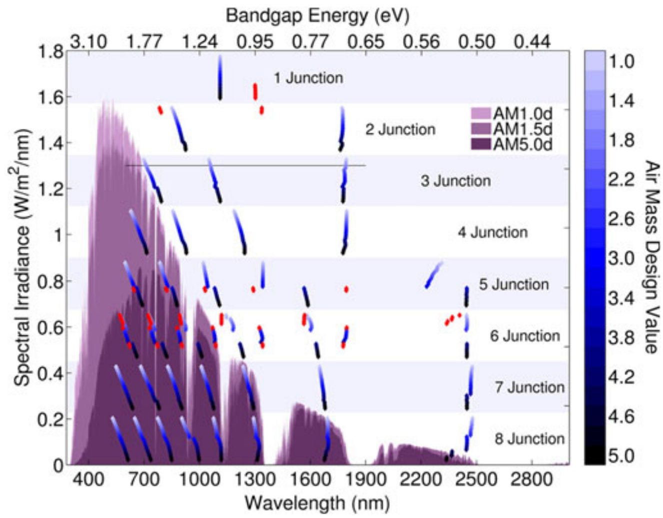

Fig. 1. Bandgap determinations for 1–8 junction solar cells that maximize conversion efficiency for the air mass spectra identified by color code (right axis). Red symbols are efficiency maximizing determinations that do not maximize energy yield. They are replaced by bandgap values that provide local conversion efficiency maxima with higher annual energy yields.

identified by the intersection of the color-graded curves with a horizontal line, as is shown for the 3-junction device.

Except for the single-junction device, choosing a different AM design value leads to notable differences in the set of optimal bandgaps. This is most apparent for higher energy subcells, where the typically negative slope of the color-graded line usually lowers bandgap energies due to an increasing red shift at higher AMs. However, this is not a general observation, due to the presence of absorption lines in the AM spectra.

Efficiency-maximizing bandgap combinations are sometimes constrained by absorption lines in the spectral design point to values that are suboptimal for long-term energy production. These are the anomalous bandgap values in Fig. 1, shown in red. As an illustration, consider the single junction device. The optimal bandgap remains unchanged at ∼1.1 eV (∼1100 nm) for AM design values up to 3.6, even though the spectrum becomes increasingly red rich. Normally, a red shift in spectral color balance results in a bandgap decrease because the increase in current harvested dominates the slight decrease in cell voltage. However, the absorption line at energies just below 1.1 eV means that no additional current can be collected by decreasing the bandgap energy until the red shift becomes quite severe. This occurs at an AM design value of 3.8, where the optimal bandgap undergoes a step change to another local efficiency maxima at ∼0.95 eV (∼1300 nm).

The above explanation is general and holds for the optimization of devices with more junctions as well. This also explains the pronounced discontinuities in the color-graded curves, especially for the 5- and 6-junction devices. With increasing AM, there is a transition from one stable optimization region to another. The regions of well-defined global maxima are typically separated by a transition region where multiple local maxima have similar magnitudes, which render definitive identification of global maxima ambiguous. It is here where anomalous bandgap combinations are found. We resolve the ambiguity by replacing global maximum combinations (the red data) with local maximum combinations if the latter give a higher annual energy yield. In the 3, 4, 7, and 8-junction cases, there are no absorption lines near the optimal bandgap positions and thus no transition between local maxima in this general case. These results can be tuned by the application of an optical transfer function, modifying the candidate spectral inputs, or the addition of constraints on bandgaps, accounting for manufacturability. These well-defined bandgap sets were then used as inputs to our energy yield calculations to uniquely identify the representative spectrum for each location.

III. Annual Energy Yield

A. Computational Approach

Direct energy yield calculation requires a spectrum to be generated (or measured) for each time interval in the year. Each spectrum must be input to an equivalent circuit model for the MJSC under consideration to determine its power production and the results then integrated over the year. This is computationally intensive because the time resolution must be on the order of minutes if the effect of changing AM is to be accurately captured. However, assuming clear skies and constant ambient conditions, the same spectral conditions will occur repeatedly throughout the year. Using local AM as a spectral proxy, a discrete distribution of the total direct beam energy in fixed AM intervals ("bins") may be enumerated from the time series. Energy yield calculations may then be done across a small number of AM bins rather than across a vast number of time intervals.

We use AM as a proxy for describing spectral changes because it is the fastest and most consistently changing spectral condition and drives the broad trends in the optimization problem. In this case, the absolute energy yield produced by our system, which is influenced by the dynamic levels of many atmospheric constituents, is not of interest. We are only interested in determining, based on the relative differences in energy yield produced, which method of choosing a representative spectrum gives the best results. Therefore, we assume ASTM G173 standard atmospheric conditions and neglect local weather patterns to show a self-consistent comparison to the 50% AM approach.

To illustrate the efficacy of the AM proxy approach, we compare brute force calculations of the annual direct beam energy for Boulder (USA) on 5 min time intervals (19 hour run time) with calculations for the same spectral conditions discretized across 0.5 AM intervals (4 min run time). The relative difference in annual energy yield is ~0.1%. To facilitate the high time resolution we require, we now move to 30 s time stamps for our calculations because the time cost is low. Compared to the brute force approach, the AM binning approach reduces the run time by ~3 orders of magnitude since the repeated conditions in the ~526 000 30-s daylight time stamps are eliminated by collection into ~750 bins of 0.05 AM width.

Binning of AM occurrences is performed by first finding the sun's refraction-corrected zenith angle for each 30-s time stamp at the location in question [22]. The relative air mass AM_0 at each time step is then determined from the zenith angle using the homogeneous, nonrefractive, radially symmetric, spherical atmosphere approximation [23]. To accommodate

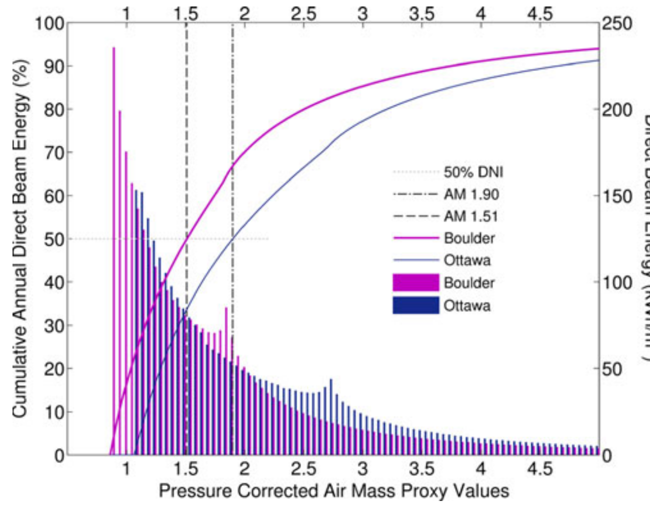

Fig. 2. Cumulative and binned clear-sky solar resource as a function of absolute (pressure corrected) AM in Boulder, USA, and Ottawa, Canada. The 50% AM value for each location is indicated by a dashed line.

the effect of elevation, the relative AMs are pressure corrected as $\mathrm{AM} = (P/P_0)\mathrm{AM}_0$, where the pressure at an elevation h above sea level is calculated using the barometric formula as $P = P_0 \exp(-Mgh/kT)$, where P_0 is the pressure at sea level, M is the average molar mass of the air, g is the acceleration due to gravity, k is Boltzmann's constant, and T is the atmospheric temperature (fixed here at 0 °C). Once the pressure-corrected AM is determined for each time stamp, the number of time steps in each AM bin is found for the year. The number of counts is multiplied by the time step and by the simulated direct normal irradiance to find the direct beam energy in that AM interval.

To illustrate the AM binning approach, we consider the local solar resource for Boulder, USA (Lat. 40.02, El. 1655 m) and for Ottawa, Canada (Lat. 45.42, El. 70 m). The AM dependence of the direct beam energies for both locations is shown in Fig. 2 by their histograms (right axis). There is the expected trend toward less incident energy at higher AMs, with peaks around solar noon at summer and winter solstices. Note that the distance between the primary (summer) and secondary (winter) peaks is much less for Boulder than Ottawa due to its lower latitude, and that very little energy is incident at AMs greater than AM5 regardless of the latitude.

The binned direct beam energies may be successively aggregated to provide cumulative direct beam energies. These results are shown by the two curves in Fig. 2 (left axis), normalized by their respective total beam energies. Since the curve for Boulder is to the left of the curve for Ottawa, lower AM components dominate its energy response. This is primarily due to its lower latitude, but its higher elevation also acts to shift cumulative energy toward lower AMs (principally due to the pressure correction).

The cumulative direct beam energy curve also enables a pressure-corrected AM value to be associated with the midpoint in the energy content of the local solar resource. The concept of a "50% AM" value was introduced by Emery *et al.* in an effort to determine a reference spectrum more generally suitable for characterizing concentrator cells than the AM1.5d STC spectrum [24]–[26]. In this regard, it suffers from some ambiguity since locations with the same 50% AM value may differ in their spectral characteristics. The dependence of 50% AM values on latitude and elevation has been more comprehensively discussed by Verlinden and Lasich [27].

Our computational approach avoids spectral ambiguity. Each candidate spectrum employed to find an optimum MJSC bandgap set is uniquely associated with a generating AM value in SMARTS2, with all spectra based on the same standard input file and clear-sky sea-level conditions. We will proceed below to find, from the set of candidate spectra, a unique and unambiguous representative spectrum that may be labeled by its AM design value. Computationally, this is done by exploiting the data reduction approach that maps time throughout the year to a discrete distribution of AM proxy values. The power produced by the MJSC from the spectrum associated with each AM interval is determined using an equivalent circuit model with one diode per subcell, each with perfect quantum efficiency, no luminescent coupling between subcells, and junction operating temperatures corresponding to that for which the bandgaps were optimized (i.e., 60 °C). It should be noted that luminescent coupling is expected to mitigate some of the penalty associated with current mismatch between subcells and, therefore, may reduce the sensitivity of the energy yield to the choice of representative spectrum. The annual energy yield is found by summing the individual energy yields from all AM bins.

B. Representative Spectrum

We now exploit our computational approach to illustrate, for the Boulder and Ottawa locations, how representative spectra are determined. We caution that these results still assume clear skies and ASTM standard atmospheric conditions. The application of local measurements will calibrate the results such that absolute energy yield predictions can be achieved but at this point we would like to demonstrate the methodology and the differences that appear due to AM variation and the number of subcells only. The optimized bandgap data of Fig. 1, which are general for all locations, define specific MJSC equivalent circuit models identified by their AM design value. A discrete distribution of AM proxy values (similar to that of Fig. 2, but without the pressure correction) is created for each location. The local spectrum associated with each AM proxy value is then generated by SMARTS2 (which accounts for elevation) as model input to determine power production. This is then multiplied by the number of counts in the AM bin and by the time interval to give the energy yield for the AM proxy value. Summation across all AM bins then gives the annual energy yield for the particular MJSC specified by that AM design value. These are the colored solid symbols in Fig. 3(a) for Boulder, and Fig. 3(b) for Ottawa; the solid, colored lines are guides to the eye through MJSC designs with the same number of junctions. Annual energy yields (left axis) for each AM design value are also given as average daily energy yields (right axis). For all devices, Boulder has higher overall energy yields than Ottawa, as a result of its greater solar resource, but the general trends in the energy yield curves are the same for both locations.

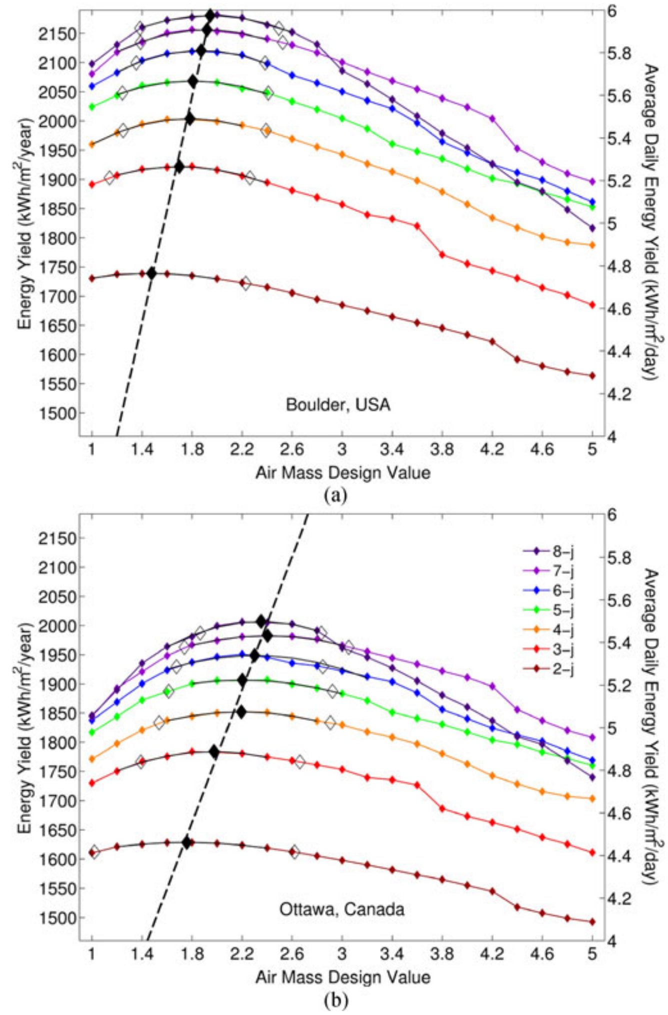

Fig. 3. Solid, colored diamonds indicate annual energy yields for (a) Boulder and (b) Ottawa calculated using the bandgap combinations in Fig. 1 that were designed using the candidate representative spectra denoted by their AM design values. Solid, colored lines connect cell designs of the same junction number. Open diamonds indicate 1% fall-off in yield. Solid black diamonds with dashed fit line indicate representative spectra.

For fixed AM design value, devices with more junctions typically harvest more light, but the magnitude of this increase successively diminishes. The 8-junction cell is the only device that does not universally show this increase, and then only for the higher AM design values. This likely denotes a failure in the bandgap optimization process as the complexity of the design space increasingly inhibits accurate identification of the global efficiency maximum.

For each MJSC, the solid black diamond shows the interpolated energy yield maximum at the optimal AM design value which identifies the representative spectrum. As indicated by the dashed lines for both locations, we observe that maximum annual energy yields scale almost linearly with AM design value as the number of junctions is increased. We expect this direction of trend because more junctions mean more capacity to take advantage of lower energy photons which cannot be prioritized when maximizing conversion efficiency with fewer junctions.

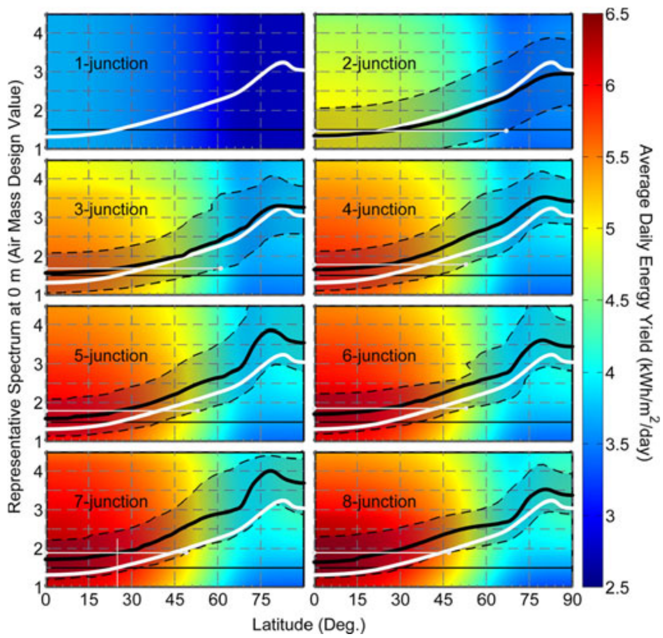

Fig. 4. Color maps of the clear-sky energy yield at sea level as a function of latitude and AM design value for the indicated MJSCs. The solid black curves denote the dependence of the representative spectrum on latitude while the solid white curves give the corresponding dependence for 50% AM values. The dashed curves delimit the regions of 1% deviation from energy yield maxima. AM1.5 is highlighted by a horizontal black line.

To our knowledge, this is the first time this trend has been resolved from the noise and quantified.

Note that the maximum energy yield trend lines differ significantly in slope, with greater departure from the vertical at higher latitudes. This is relevant in the context of energy yield sensitivity to AM design value, and is first seen in the individual energy yield curves. In Fig. 3, the open diamonds span the range of AM design values for which annual energy yields depart from the MJSC maximum by no more than 1%—an ad hoc metric by which we may quantify energy yield sensitivity. Annual energy yields at each location are seen to be very insensitive to design, even for devices with many junctions. There does, however, appear to be a design dependence on location that warrants more consideration.

IV. Design Assessment

A. Design Tolerance and Dependence on Latitude

We have mentioned above that a significant range of AM design values is spanned by a 1% deviation from any local annual energy yield maximum. We now address how tolerant our RSS approach is to location, specifically the latitude. We use sea-level conditions and the ASTM standard atmosphere in all circumstances in order to also enable spectrally unambiguous 50% AM values for comparative design assessment. For all latitudes, we again identify as the representative spectrum that AM design value which maximizes MJSC annual energy harvest, and we perform all calculations in the manner previously described.

Fig. 4 shows color maps of average daily energy yield (right axis, color bar) as a function of AM design value and latitude for each MJSC under consideration; the single junction case is included for completeness. Bold black curves show the dependence of the representative AM design value (left axis) on latitude; each curve is bounded by a semitransparent region whose dashed boundaries denote 1% deviations from energy yield maxima.

Fig. 4 also enables qualitative comparison between the different design approaches. Bold white curves show the dependence of the 50% AM value (calculated at sea level with the ASTM G173 standard atmosphere) on latitude. The 50% AM values universally underestimate our representative AM design values over all latitudes but typically remain within the boundaries of the 1% deviations from energy yield maxima. Similar comparison may be made with the AM1.5d design spectrum, denoted by the horizontal black lines. This design value is below the representative AM design values over all latitudes, except for the 2JSC, where it is slightly above for latitudes below 25°. While the AM1.5d approach appears well within the boundaries of our 1% deviations at low latitudes, the improvements identified by our RSS approach appear much more significant at the higher latitudes and for cells with greater number of junctions.

TABLE I
Comparative Design Tolerance to Latitude (Degrees from Equator)

No. of Junctions	2	3	4	5	6	7	8
Canonical Rep. Spect.	67°	61°	53°	53°	53°	49°	47°
AM1.5	68°	50°	42°	40°	35°	32°	30°

In order to better assess design tolerance, we define the canonical representative spectrum for each MJSC to be associated with its AM design value at latitude ∼25°. This latitude is chosen as the reference since it is the intersection of the 50% AM values with the AM1.5 line. To use a canonical cell design at other latitudes means less energy will be harvested, compared to a cell designed with the latitude-specific representative spectrum. The maximum extent in latitude associated with a 1% loss penalty then spans the range indicated by the horizontal white lines in Fig. 4 for each MJSC under consideration. The results are summarized in Table I, where comparison is made with cells designed to the AM1.5d spectrum. We see that our RSS approach leads to designs that are more tolerant to site location as junction number is increased. However, the impact will only be noted at midlatitudes for the emerging CPV systems using cells with four or more junctions. Further insights may be given by more quantitative design comparisons.

B. Quantitative Comparison of Design Approaches

We compare annual energy yields calculated using our RSS approach with those calculated using the AM1.5d and the 50% AM design approaches. Since we find better energy harvesting under all circumstances, the comparison is enabled by calculating an energy yield enhancement given by the energy yield difference normalized by the energy yield of the alternative approach. In Fig. 5(a), we see that the enhancement, relative to the

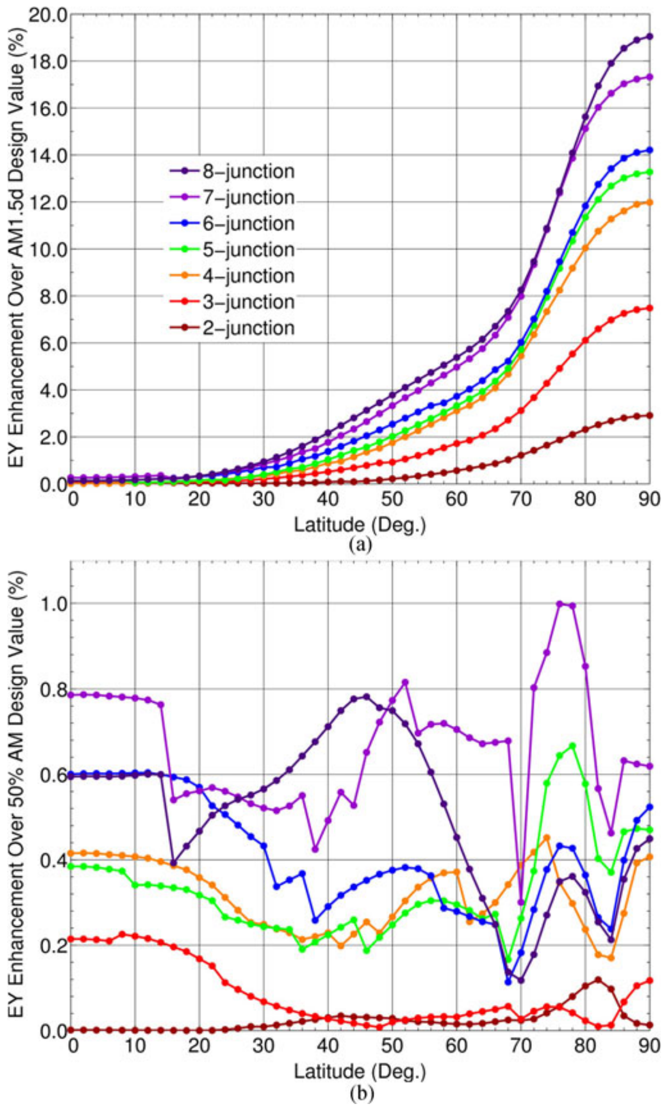

Fig. 5. Improvement in relative energy yield using representative spectrum selection rather than (a) the AM1.5d spectrum, or (b) the 50% AM spectra.

AM1.5d approach, is less than 1% for latitudes less than ∼30°, but it then strongly increases with both latitude and junction number. For these higher latitudes, the enhancement typically increases monotonically with the increase in the number of junctions due to the MJSC's increasing sensitivity to current balance. By midlatitudes (∼45°), the improvements range from about 1% (3JSC) to about 3% (8JSC). The gains are more dramatic at the higher latitudes, but here the solar resource is small and CPV is far less likely to see deployment, so comparison is not justified.

Fig. 5(b) shows that the enhancements, relative to the 50% AM approach, are typically less than 1%. The comparative energy yield data show little dependence on latitude for low junction number. By contrast, at higher junction number, greater fluctuations in the latitude dependence are noted. This is due to the small difference between large values accentuating the effect of cell design sensitivity to spectral content on the current balance. It is an inherent consequence of our ability to capture the cell sensitivity to spectral conditions. Thus, although the 50% AM design approach does come close to our results, it lacks the methodological effectiveness that our RSS approach demonstrates in addressing cell response to spectral variations.

V. Conclusion

Through systematic tests of candidate AM spectra and an efficient data reduction approach predicated on proxy AM spectra, we identified the representative spectrum that should be used to optimize MJSC design for maximum annual energy yield at each location. We have undertaken a full tolerance analysis and compared our RSS approach with AM1.5d and 50% AM cell design approaches across all latitudes for cells with 2–8 junctions. Relative to the AM1.5d approach, we find enhanced yields that strongly increase with both latitude and junction number. As a consequence, MJSCs designed to a single canonical representative spectrum can generally be used across a broader range of latitudes than those designed using the AM1.5d spectrum. For MJSCs with four or more junctions used at midlatitudes, the AM1.5d approach cannot be used without suffering an increasingly severe yield penalty. However, while it is important to note that both approaches substantially agree at low latitudes for cells with few junctions, which has been the design context to date, it is equally important to note that our RSS approach is very timely, since 10 MW of utility scale CPV is planned for deployment in Canada (Vulcan, AB, latitude 50.4 °N) [28].

While our results are better than the 50% AM approach, the improvement is negligible at low junction number, and still sub-1% at high junction number. However, the 50% AM approach suffers from design ambiguity when the clear-sky sea-level constraint is removed. Since its spectrum must be determined for the specific local condition, the same value can represent fundamentally different spectra. By contrast, our RSS approach relies on a fixed set of pre-identified unique spectral candidates. Although not a fully general optimization approach, because the set we use broadly characterizes local spectral content, it provides an unambiguous means of establishing design sensitivity to parameter variations.

We have developed an approach to systematically assess the design impact of spectral variations in the local solar resource on annual energy yield. While our methodology has been demonstrated across all latitudes at sea level using simulated spectral conditions under a clear-sky standard atmosphere, it may also be used to assess the impact of variations in local atmospheric conditions and elevation.

References

[1] K. Toprasertpong *et al.*, "Absorption threshold extended to 1.15eV using InGaAs/GaAsP quantum wells for over-50%-efficient lattice-matched quad-junction solar cells," *Prog. Photovolt.: Res. Appl.*, vol. 24, no. 4, pp. 533–542, 2015, doi: 10.1002/pip.2585.

[2] R. R. King *et al.*, "Solar cell generations over 40% efficiency," *Prog. Photovolt.: Res. Appl.*, vol. 20, pp. 801–815, 2012, doi: 10.1002/pip.1255.

[3] G. S. Kinsey *et al.*, "Advancing efficiency and scale in CPV arrays," *IEEE J. Photovolt.*, vol. 3, no. 2, pp. 840–843, Apr. 2013.

[4] F. Dimroth *et al.*, "Development of high efficiency wafer bonded 4-junction solar cells for concentrator photovoltaic applications," in *Proc. 40th IEEE Photovolt. Spec. Conf.*, Denver, CO, USA, 2014, pp. 840–843.

[5] K. Ghosal *et al.*, "Ultra high efficiency HCPV modules," in *Proc. 42nd IEEE Photovolt. Spec. Conf.*, New Orleans, LA, USA, 2015, pp. 1–3.
[6] M. J. O'Neill, A. J. McDanal, and P. A. Jaster, "Development of terrestrial concentrator modules using high-efficiency multi-junction solar cells," in *Conf. Rec. 29th IEEE Photovolt. Spec. Conf.*, 2002, pp. 1369–1372.
[7] X. Wang and A. Barnett, "The effect of spectrum variation on the energy production of triple-junction solar cells," *IEEE J. Photovolt.*, vol. 2, no. 4, pp. 417–423, Oct. 2012.
[8] S. P. Philipps *et al.*, "Energy harvesting efficiency of III–V triple-junction concentrator solar cells under realistic spectral conditions," *Sol. Energy Mater. Sol. Cells*, vol. 94, pp. 869–877, 2010.
[9] A. L. Dobbin *et al.*, "How important is the resolution of atmospheric data in calculations of spectral irradiance and energy yield for (III–V) triple-junction cells?," in *Proc. 6th Int. Conf. Concentrating Photovolt. Syst., AIP Conf. Proc.*, 2010, pp. 303–306.
[10] N. Chan *et al.*, "Variation in spectral irradiance and the consequences for multi-junction concentrator photovoltaic systems," in *Proc. 35th IEEE Photovolt. Spec. Conf.*, 2010, pp. 003008–003012.
[11] J. E. Haysom, O. Jafarieh, H. Anis, and K Hinzer, "Concentrated photovoltaics system costs and learning curve analysis," in *Proc. 9th Int. Conf. Concentrator Photovolt. Syst., AIP Conf. Proc.*, vol. 1556, 2013, pp. 239–243.
[12] S. Tomosk, D. Wright, K. Hinzer, and J. E. Haysom, "Analysis of present and future financial viability of high concentrating photovoltaic projects," in *High Concentrator Photovoltaics: Fundamentals, Engineering and Power Plants*, P. Pérez-Higueras and E. F. Fernández, Eds. New York, NY, USA: Springer, Aug. 2015, ch. 16.
[13] J. E. Haysom, O. Jafarieh, H. Anis, K. Hinzer, and D. Wright, "Learning curve analysis of concentrated photovoltaic systems," *Prog. Photovolt.: Res. Appl.*, vol. 23, pp. 1678–1686, 2015.
[14] G. S. Kinsey and K. M. Edmondson, "Spectral response and energy output of concentrator multijunction solar cells," *Prog. Photovolt.: Res. Appl.*, vol. 17, pp. 279–288, 2009.
[15] I. Garcia *et al.*, "Field spectra binning for energy production calculations and multijunction solar cell design," in *Proc. 42nd IEEE Photovolt. Spec. Conf.*, New Orleans, LA, USA, 2015, pp. 1–3.
[16] W. Guter *et al.*, "Current-matched triple-junction solar cell reaching 41.1% conversion efficiency under concentrated sunlight," *Appl. Phys. Lett.*, vol. 94, 2009, Art.ID. 223504.
[17] N. L. A. Chan, H. E. Brindley, and N. J. Ekins-Daukes, "Impact of individual atmospheric parameters on CPV system power, energy yield and cost of energy," *Prog. Photovolt.: Res. Appl.*, vol. 22, pp. 1080–1095, 2013, doi: 10.1002/pip. 2376.
[18] C. Gueymard, *SMARTS2, A Simple Model of the Atmospheric Radiative Transfer of Sunshine: Algorithms and Performance Assessment*. Orlando, FL, USA: Florida Solar Energy Center, Univ. Central Florida, Publication number: FSEC-PF-270-95, Dec. 1995.
[19] G. Arbez *et al.*, "4 Junction dilute nitride solar cell optimization: Comparing current matching approaches in detailed balance algorithms," in *Proc. IEEE 39th Photovolt. Spec. Conf.*, Tampa, FL, USA, Jun. 2013, pp. 2073–2077.
[20] A. Bett, "etaOpt," Fraunhofer-Institut für Solare Energiesysteme ISE. [Online]. Available: http://www.ise.fraunhofer.de/de/ geschaeftsfelder/iii-v-und-konzentrator-photovoltaik/themen/iii-v-epitaxie-und-solarzellen/fue-leistungen/simulation/etaopt. Accessed in: Aug. 2015.
[21] W. Shockley and H. J. Queisser, "Detailed balance limit of efficiency of p-n junction solar cells," *J. Appl. Phys.*, vol. 32, pp. 510–519, 1961.
[22] I. Reda and A. M. Andreas, "Solar position algorithm for solar radiation application," *Sol. Energy*, vol. 76, pp. 577–589, 2004.
[23] E. Schoenberg, "Theoretische photometrie, Über die Extinktion des Lichtes in der Erdatmosphäre," in *Handbuch der Astrophysik. Band II, erste Hälfte*. Berlin, Germany: Springer, 1929.
[24] K. Emery, D. Myers, and S. Kurtz, "What is the appropriate reference spectrum for characterizing concentrator cells," in *Proc. 29th IEEE Photovolt. Spec. Conf.*, 2002, pp. 6–10.
[25] D. Myers, K. Emery, and C. Gueymard, "Proposed reference spectral irradiance standards to improve concentrating photovoltaic system design and performance evaluation," in *Proc. 29th IEEE Photovolt. Spec. Conf.*, 2002, pp. 923–926.
[26] D. Myers, K. Emery, and C. Gueymard, "Revising and validating spectral irradiance reference standards for photovoltaic performance evaluation," *J. Sol. Energy Eng.*, vol. 126, no. 1, pp. 567–574, 2004.
[27] P. J. Verlinden and J. B. Lasich, "Energy rating of concentrator PV systems using multi-junction III–V solar cells," in *Proc. IEEE 33rd Photovolt. Spec. Conf.*, San Diego, CA, USA, May 2008, pp. 1–6.
[28] Climate Change and Emissions Management Corporation, Alberta Solar One. [Online]. Available: http://ccemc.ca/project/alberta-solar-one/. Accessed in: July 2016.

Mark D. Yandt received the B.Eng.Mgt. degree in engineering physics and management from McMaster University, Hamilton, ON, Canada, in 2008, the M.A.Sc. degree in electrical and computer engineering from the University of Ottawa, Ottawa, ON, Canada, in 2012, and is currently working toward the Ph.D. degree in the School of Electrical Engineering and Computer Science, University of Ottawa, studying under K. Hinzer and H. Schriemer.

He oversees experimental design and system characterization for a number of projects at the Sunlab that involve the dynamics and reliability of high-concentration photovoltaic systems. His research interests include the development, characterization, optimization, and deployment of photovoltaic and concentrating photovoltaic systems.

Mr. Yandt received an Ontario Graduate Scholarship in 2011 and the Alexander Graham Bell Canada Graduate Scholarship funded by the Natural Sciences and Engineering Research Council of Canada in 2012.

Karin Hinzer (M'08) received the B.Sc., M.Sc., and Ph.D. degrees in physics from the University of Ottawa, Ottawa, ON, Canada, in 1996, 1998, and 2002, respectively.

She is currently an Associate Professor and the Canada Research Chair in photonic nanostructures and integrated devices and an Associate Professor in the School of Electrical Engineering and Computer Science, University of Ottawa. She has made pioneering contributions to the experimental physics of quantum dots marked by two landmark papers in *Science*. She gained extensive experience in the design and fabrication of groups III–V semiconductor devices while with the National Research Council Canada, Nortel Networks, and Bookham. Cost-reduction strategies and liaison with remote fabrication facilities strongly feature in her industry experience. In 2007, she joined the University of Ottawa, where she is the Founder of the Sunlab, which is a modeling and characterization laboratory specializing in the development of high-efficiency solar cells. Since the laboratory's inception, she has trained more than 80 highly qualified personnel in the field of photovoltaic system and devices. Since 2010, she has been with the Inorganic Photovoltaics Cotheme Leader within the Pan-Canadian Photovoltaic Research Network.

Dr. Hinzer received the Inaugural Canadian Energy Award, with industry partner Morgan Solar, for the development of more efficient solar panels, in 2010.

Henry Schriemer (M'00) received the B.Sc. degree in mathematics and the Ph.D. degree in physics from the University of Manitoba, Winnipeg, MB, Canada, in 1987 and 1997, respectively.

He is currently an Associate Professor in electrical engineering with the University of Ottawa, Ottawa, ON, Canada, where he previously held an NCIT Research Fellowship in photonics from 2003 to 2005. Prior to this, he spent several years in the photonics industry, where he is recognized as one of the innovators of strain engineered planar lightwave circuits. He has held a Postdoctoral Fellowship in laser physics and nanophotonics at the van der Waals-Zeeman Institute, Amsterdam, The Netherlands, where he made the first measurements of significant spontaneous emission inhibition in active photonic crystals. He has authored more 90 refereed publications. His recent activities have ranged across the photovoltaics landscape, with an emphasis on design and simulation, test and measurement, local solar resource assessment, and energy yield analysis. His present focus is on energy management for smart grids. His previous research accomplishments have ranged from the description of optical singularities in photonic crystals to fundamental advances in the design and realization of laterally-coupled distributed feedback lasers.

4.2 Representative Atmospheric Parameters for Multi-Junction Solar Cell Design

4.2.1 Scope and Impact

This paper addresses the most significant assumptions that were made in the previous work. In that work, energy yield calculations were accelerated in order to compare a carefully selected set of alternative bandgap combinations. The acceleration was facilitated by assuming that the atmospheric content, and therefore the terrestrial spectrum at a given air mass did not fluctuate day to day or throughout the year. This allowed us to use air mass as a proxy for time and to bin the repeated occurrences of each air mass so that energy calculations did not have to be made multiple times for the same air mass values which occur daily. This accelerated energy yield calculation accounts for latitude and air mass and thus the two primary factors influencing the insolation. We were, thus, able to perform a general analysis as a function of latitude to show the broad geographical trends using the representative spectrum selection approach. However, it also required us to assume a single set of representative atmospheric parameters for input to the absorption models when in reality these atmospheric parameters fluctuate throughout the day and year. We recognized this assumption meant that we could only rely on the trends we had identified and not specifically on the representative spectra determined for a particular location. We now demonstrate not only that representative parameters are sufficient to accurately determine the energy yield maximizing representative spectrum, but also show how those parameters can be extracted from local historical data sets.

We apply the representative spectrum approach outlined in the previous paper and use measured data to demonstrate how the approach can be used to determine the local representative spectrum and the energy yield maximizing bandgap combinations in Ottawa. Ottawa is chosen for a couple of reasons but the primary reason is that a complete annual dataset of spectral irradiance date is available to validate our calculations. Using this measured dataset to confirm our conclusions, we show that local representative atmospheric parameters can be used to determine local representative spectra using the representative spectrum approach in lieu of spectral irradiance data. Having demonstrated the validity of using representative parameters and showing how they should practically be chosen, we look at the effect of changing those parameters on the representative spectrum. We assess the effects of aerosol absorption and precipitable water absorption which are the next most influential factors after latitude and air mass.

Understanding the effect these atmospheric parameters have on optimal cell designs allows us to predict local energy ratings and the differences in those energy ratings for locations with different average atmospheric AOD_{500} or PW. We provide coefficients that allow for the mapping of both representative spectrum and energy yield as a function of representative AOD_{500} and PW changes.

4.2.2 Author Contributions

Mark Yandt: The scientific contributions in this manuscript are entirely my own but were supported, guided or encouraged at times by the other authors. The primary contribution is the demonstration that representative atmospheric parameters can be used to predict energy yield maximizing bandgap combinations for MJSCs. This means that it is not necessary to consider the independent contributions of temporally unstable atmospheric constituents throughout the year. An important supporting contribution is the method by which those representative atmospheric parameters should be chosen from historical climatic data.

Dr. Karin Hinzer: As my co-supervisor and the principal researcher on the grant funding the work I performed, Karin guided the direction of the research and assisted in the editing of the final manuscript.

Dr. Henry Schriemer: As my co-supervisor and a researcher listed on the grant funding the work I performed, Henry guided the direction of the research and assisted in the editing of the final manuscript.

4.2.3 Publication

Paper attached on next page. This paper is about to be submitted to IEEE Journal of Photovoltaics.

Representative Atmospheric Parameters for Multi-Junction Solar Cell Design

Mark D. Yandt, Karin Hinzer, *Member, IEEE,* and Henry Schriemer, *Member, IEEE*

***Abstract* —The representative spectrum selection *(RSS)* approach is applied systematically to determine efficiency maximizing multi-junction solar cell (MJSC) bandgap combinations that also maximize energy yield in Ottawa, Canada. The technique is performed using a complete, validated dataset of spectral irradiance measurements collected in 2015 and compared to the same calculation using simulated spectra and constant (non-fluctuating) representative atmospheric parameters. We thus test the concept of *representative atmospheric parameters* and show that a single set of parameters is sufficient to predict energy yield maximizing design points in a particular location even though, in reality, these parameters fluctuate during the day and year. We demonstrate that these representative parameters can be gleaned from historical data sets by identifying the 50% cumulative DNI values.**

Representative spectra, for 1-8 junction SCs, are then determined as a function of aerosol optical depth (AOD) and precipitable water (PW). Coefficients that describe the change in the energy yield and representative spectrum as a function of changing representative AOD and PW from one location to another are presented.

***Index Terms*— Representative spectrum, Air mass, Annual energy yield, Multi-junction solar cell, Bandgap optimization, Aerosol optical depth, Precipitable water, Elevation, Latitude.**

I. Introduction

MANY next generation multi-junction solar cells (MJSCs) have 4 or more junctions and are more than 40% efficient [1]-[5]. The cost of these technologies is offset using relatively large area concentrating photovoltaic (CPV) systems to glean the advantages of very small area, high efficiency solar cells. It has been shown by Kurtz *et al.* [6] that stable long-term performance ratios of 90-95% are achievable for CPV modules if, among other primary considerations such as a relatively large acceptance angle and temperature stable optical efficiency, the system is optimized for an air mass that is well matched to the deployment location. To demonstrate that these conditions have been met, systems have to be deployed for years at a time to collect sufficient data over all seasonal conditions. Since this time cost is large, it is critical that the effects of local ambient dynamics are well understood so that their impact on the system may be addressed at the design stage.

Tuning system variables for local field performance instead of for standard test conditions (ASTM G173-03 AM1.5d spectrum [7]-[9], 25ºC cell temperature and 1000 W/m2) is, economically speaking, how one endeavors to maximize a power plant's net present value [10]-[12] at a given price point. The level of detail required to perform this tuning is still under discussion [5],[6],[13]-[15]. We investigate the systematic application of the conventional representative spectrum approach to bandgap optimization in order to determine a more optimal MJSC design point as a function of atmospheric content. This realization facilitates the mapping of cell recipes over geographical areas with similar enough annual spectral content. We first describe the conventional representative spectrum approach.

In this work we consider a *true* representative spectrum to be one that is completely defined (easily reproduced or simulated) and that accounts for all variations in the local spectra it represents such that MJSC bandgap combinations chosen to maximize its conversion efficiency also maximize annual energy yield. In one sense, the 2003 ASTM G173-03 AM1.5d spectrum that was adopted as a testing standard for concentrator MJSCs is representative because it "more closely represents" the AM1.5d direct normal irradiance (DNI) spectrum in regions where CPV systems are likely to be deployed [6]. The justification for AM1.5 is the fact that 50% of the annual direct beam energy is delivered at pressure corrected air masses below (or above) 1.5 for many locations in the continental USA [6]. This spectrum is well defined but does not attempt to function as a *true* representative spectrum in any particular location. Verlinden and Lasich [15] determined pressure corrected 50% air masses as a function of latitude and elevation arguing that these air masses can be used to define local spectra for which MJSCs should be optimized to maximize local energy yield. In this case, local information is incorporated into the representative spectrum selection process but the 50% air mass metric alone does not completely define a spectrum unless representative atmospheric parameters are also specified. Nevertheless, if the appropriate representative atmospheric inputs are available, it is possible to define a spectrum.

Manuscript received xx October 2016. The authors acknowledge support from the Natural Sciences and Engineering Research Council of Canada for funding programs that supported this research.

M. D. Yandt is with the Department of Electrical and Computer Engineering, Sunlab, University of Ottawa, Ottawa, ON K1N 6N5, Canada (e-mail: markyandt@gmail.com).

K. Hinzer, and H. Schriemer are with the Sunlab, University of Ottawa, Ottawa, ON K1N 6N5, Canada (e-mail: khinzer@uottawa.ca; hschriemer@uottawa.ca).

Color versions of one or more of the figures in this paper are available online at http://ieeexplore.ieee.org.

Digital Object Identifier xx.xxxx/JPHOTOV.2016.xxxxxxx

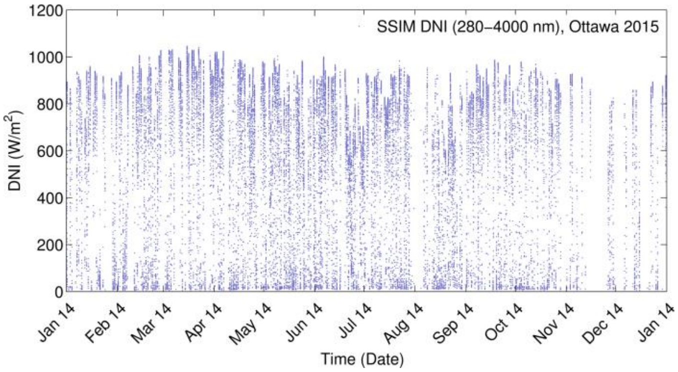

Fig. 1. DNI measured using the SolarSIM-D1 from Spectrafy Inc. [22]

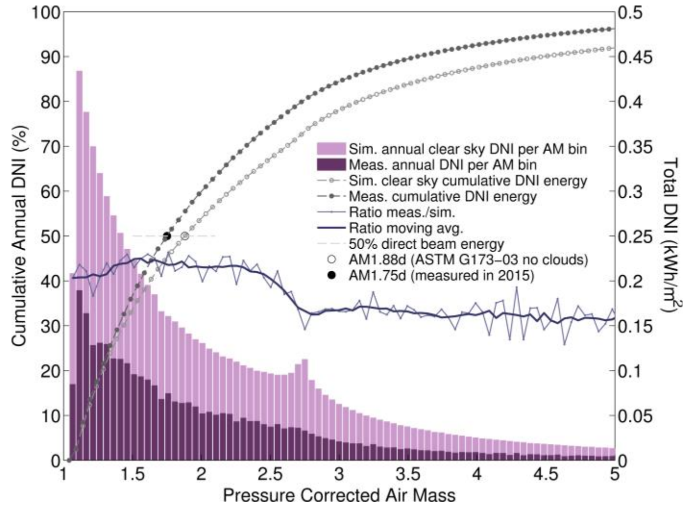

Fig. 2. Clear sky simulated DNI compared to measured DNI as a function of pressure corrected air mass.

Typically, such a spectrum is then used in a detailed balance calculation to identify the bandgap combination that maximizes its conversion efficiency. It remains unclear if the 50% DNI point and the representative atmospheric parameters supplied have led to a true representative spectrum also maximizing local annual energy yield. The ability to determine true local representative spectra and describe them with a single metric that was a function of changing local atmospheric parameters would allow comparison of spectral content between locations. This would speak to the range of optimal spectral design points that exist and how many different cell recipes are necessary to minimize design related energy yield penalties across all potential deployment locations. Then we can analyze the cost benefit of creating new recipes.

To address these drawbacks, we use a systematic application of the traditional representative spectrum approach to find efficiency maximizing bandgap combinations for a broad set of well-defined representative spectrum candidates between AM1d and AM5d. Since air mass is the only parameter that varies between candidate spectra, and all other parameters are well defined, the air mass labels of the candidates become a proxy by which we describe the spectral variations of interest. We then use these candidate bandgap combinations and local spectral irradiance measurements as inputs to simulate local annual energy yields for each candidate representative spectrum. The bandgap combination that results in the highest energy yield, thus, identifies the candidate that is the truest representative spectrum. We then simulate the local spectra input to the energy yield calculation and perform these calculations as a function of latitude, aerosol optical depth (AOD_{500}), and precipitable water (PW) to quantify the effect on the representative spectrum.

By this method we pursue the observation made by Chan et al. [23] that if average values for atmospheric extinction parameters are close to the specified constant values in the simulation, the availability of additional parameters for each time step does not result in large differences in energy yield calculations. This suggests that by identifying representative atmospheric parameters for a given location we can determine true local representative spectra and quantify the energy yield penalty of choosing a different candidate representative spectrum. The use of representative atmospheric parameters also allows us to use the much more efficient air mass binning method [13] to perform energy yield calculations. We will test this assertion for Ottawa, for which we have a complete measured spectral irradiance dataset that we can use to validate our results. We show that there *are* representative parameters that result in nearly the same energy yield and representative spectrum trends as a function of the number of subcells. We also show how one might select such parameters from independent local data sets. Using these local representative parameters for Ottawa we quantify the red shift in the representative spectrum for cells with more junctions and confirm these results using measured spectral data. We thus demonstrate how local representative spectra can be determined and how the variation in that spectrum as a function of the number of subcells can be compared to local representative spectra in other locations.

II. Quantifying the Local Spectral Resource

Local solar resource data for Ottawa, Canada were obtained for a full year, at 5 minute intervals, beginning 14 January 2015 using the SolarSIM-D1 from Spectrafy Inc.. Ottawa was chosen because these high accuracy spectral irradiance datasets were available which were carefully screened and validated [24]. Ottawa also has highly variable atmospheric conditions which provide a stringent test of our hypothesis. The SolarSIM-D1 measures optical power in 6 carefully chosen wavelength bands and then uses a parameterized transmittance model to perform real-time spectral reconstruction and quantitative determination of atmospheric constituents. It provides PW, AOD_{500}, Angström parameters for 3 wavelength regions (α_1, α_2, α_3, β_1, β_2, β_3), O_3, and a variety of trace gas concentrations [22]. The alpha and beta parameters define a modified Angstöm approach in which the aerosol transmission is defined by:

$$T_a = \exp(-m_a \tau_a) \quad (1)$$

$$\tau_a = \beta_i (\lambda / 1\ \mu m)^{-\alpha_i} \quad (2)$$

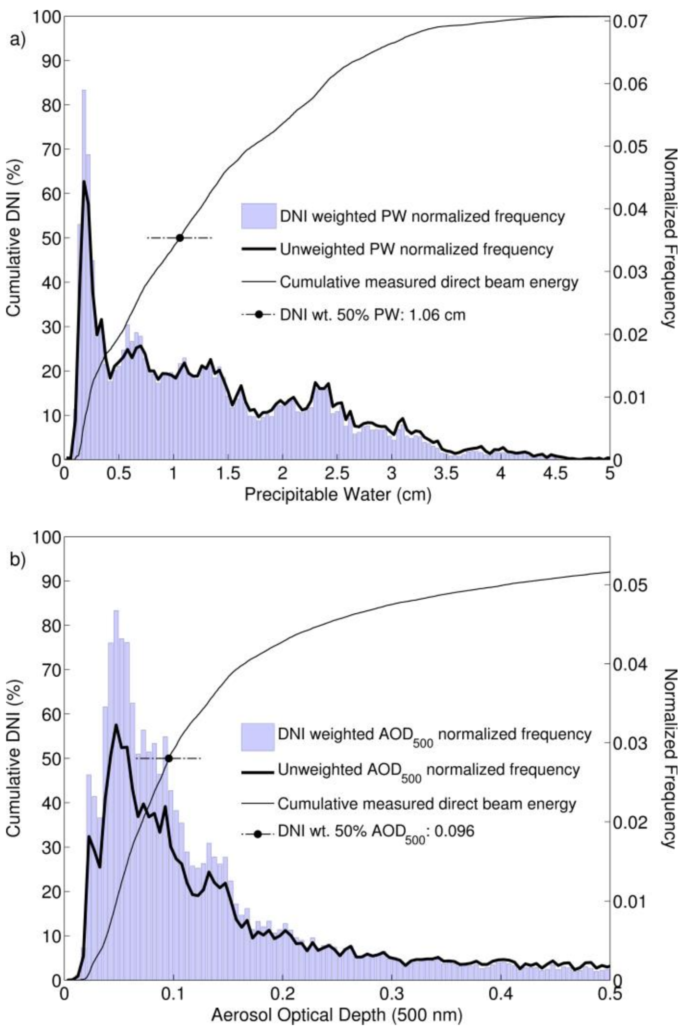

Fig. 3. Normalized frequency distribution (right axis) and cumulative DNI (left axis) for a) PW and b) AOD_{500}.

where m_a is the aerosol air mass, λ is the wavelength in μm, β_i are the Angström coefficients, α_i are the Angström exponents and i indicates the wavelength region from: 1: $\lambda <$ 500 nm, 2: 500 nm $< \lambda <$780 nm, and 3: $\lambda >$ 780 nm.

The DNI data determined from the SSIM spectra are shown in **Figure 1**. The difference between the measured (weather and cloud cover inherently included) and simulated (clear sky, no clouds) direct beam spectral irradiance is summarized in **Figure 2**. The differences are shown explicitly as a function of air mass (horizontal axis). On the left axis we show cumulative direct beam energy to demonstrate the change in the 50% air mass that a weather pattern including cloud cover causes in Ottawa. On the right axis the total DNI is shown for each 0.05 unit air mass bin. Superimposed is a moving average (blue solid line) of the ratio of measured to simulated DNI in the bins. The ratio is shown as a percentage also on the left axis.

The most obvious difference between the measured and simulated data sets in **Figure 2** is that in the total DNI. The effect of cloud cover on the available DNI in Ottawa is quantified by the difference in height between the light and dark bars. The ratio of measured to simulated DNI is provided

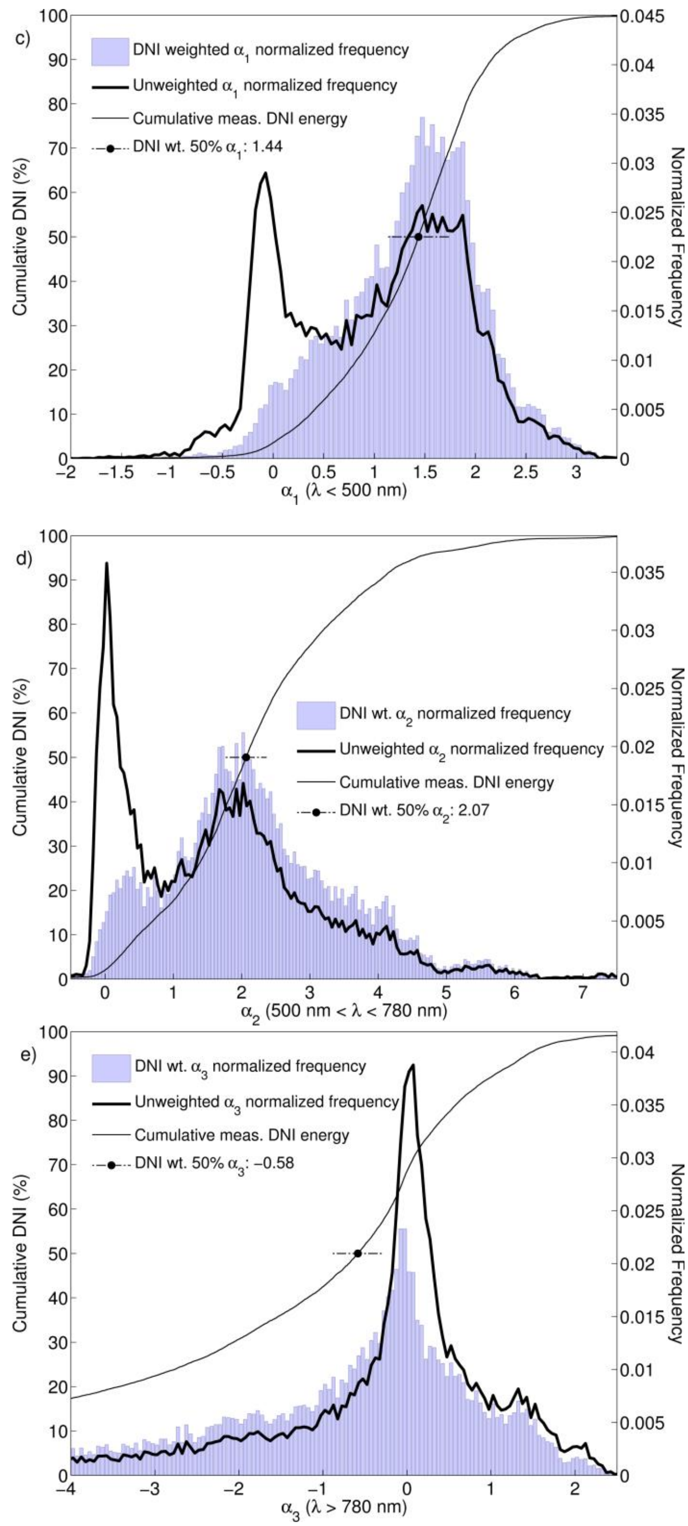

Fig. 3. Normalized frequency distribution (right axis) and cumulative DNI (left axis) for c) α_1, d) α_2, and e) α_3.

to show that weather patterns preferentially reduce the DNI for certain air masses. In Ottawa, this is due to relatively cloudy conditions in the late fall and winter which preferentially affect the higher air mass values (> AM2.7) that occur during that portion of the year.

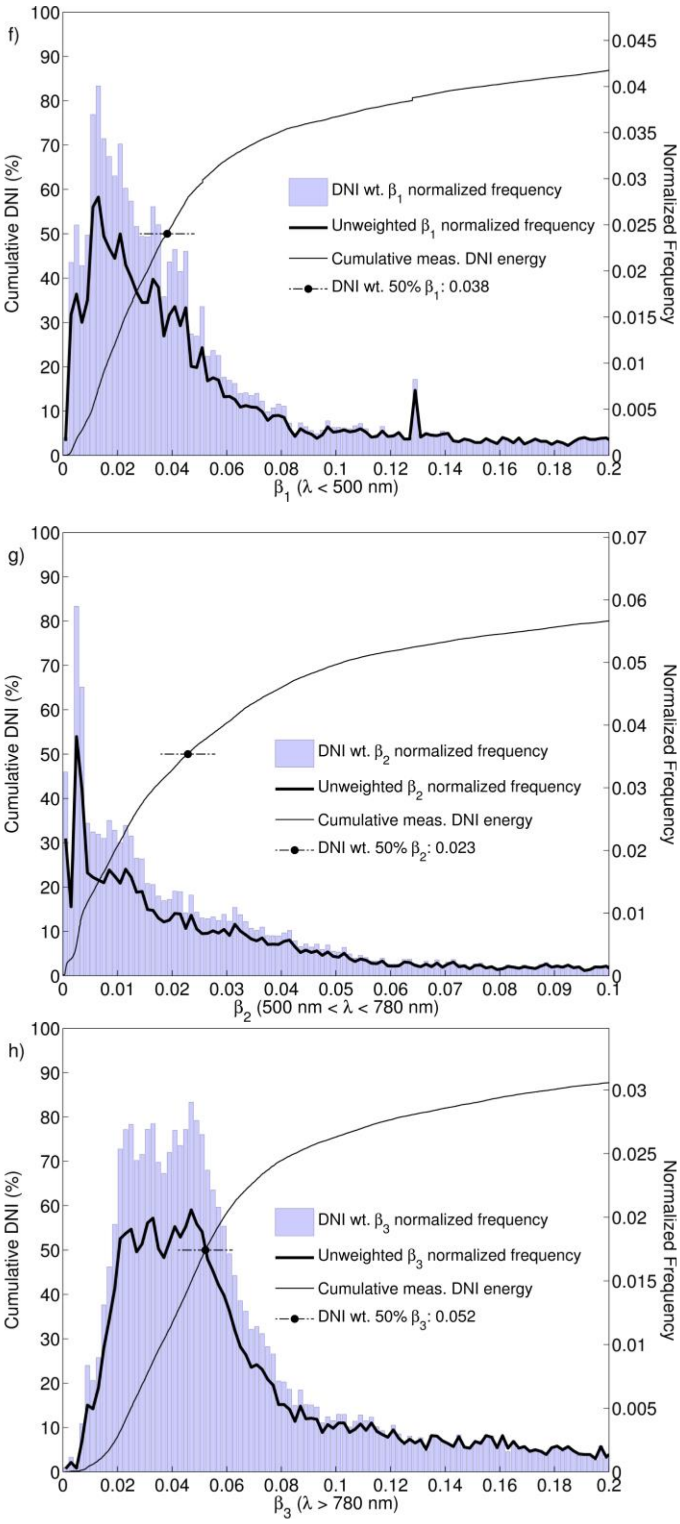

Fig. 3. Normalized frequency distribution (right axis) and cumulative DNI (left axis) for f) β_1, g) β_2, and h) β_3.

Atmospheric parameters as determined from SSIM measurements are presented in **Figure 3** for (a) precipitable water, (b) aerosol optical depth at 500 nm, (c) extinction exponent α_1, (d) extinction exponent α_2, and (e) extinction exponent α_3. Ozone and other trace gas concentrations were also included in the calculation but had a small effect and are not shown. On the right axes, the bold black curves are the normalized frequency distributions, whereas the histograms are frequency distributions arising from weighting the data by their DNI values. On the left axes, the thin black lines show how cumulative DNI evolves with the atmospheric parameter in question.

It is notable that the normalized distribution of PW in Figure 3a is very broad and extremely asymmetric. This indicates a very high variation in PW in Ottawa exemplifying the most difficult case for which to extract a representative parameter. This is typical in Ottawa due to the variation in the atmospheric content over four distinct seasons. The asymmetry quantifies the relative proportion of dry and humid conditions. The AOD_{500} frequency distribution has a single strong peak at relatively low AOD_{500}. This is a result of relatively clean clear skies experienced throughout the year in Ottawa. In the frequency distributions of the Angström exponents we observe the most significant effect of DNI weighting. This occurs because these exponents result from fits of the Angström model to power measurements at the boundaries of the wavelength regions. Thus the exponents approach zero as partial cloud cover becomes more opaque. Weighting by DNI suppresses peaks that occur for low DNI resulting in distributions that tell us about the atmospheric parameters when energy can actually be harvested. It is notable that α_3 has a distribution that includes negative values. A negative extinction exponent is unphysical over wavelength but these values do capture interesting spectral phenomena that occur in the wavelength region of the measurements used to determine α_3. Nevertheless, an α_3 of 0.01 is imposed for wavelengths greater than 1150 nm if α_3 is negative. Finally, β frequency distributions show similar form to that of AOD_{500}.

The DNI weighted 50% values identified in the frequency distributions were determined to be the most representative values (average and median values were also considered) for each parameter by comparing to energy yield calculations performed with and without representative atmospheric parameters. This comparison is shown in the next section.

III. Representative Spectrum Selection Proceedure

The MJSC design that maximizes annual energy yield is determined using the representative spectrum selection procedure [13]. In summary, ideal MJSC bandgap combinations were determined for 21 clear sky candidate representative spectra resulting in 21 cell designs that are uniquely referenced by the air mass of the spectrum for which they were optimized. The energy yield in Ottawa is then computed for each of these cell designs and the design yielding the highest energy production identifies the truest representative spectrum.

The candidate spectra (AM1d - AM5d) were produced using SMARTS2 [16] with the ASTM G173-03 standard input file (at sea level), changing only the air mass. They were used as inputs to a modified version of *mjOpt* [17]-[19], which has an equivalent circuit model within a detailed balance algorithm that was used to determine optimal MJSC bandgap combinations. A concentration of 1000x and a cell operating temperature of 60°C were used. These bandgap combinations

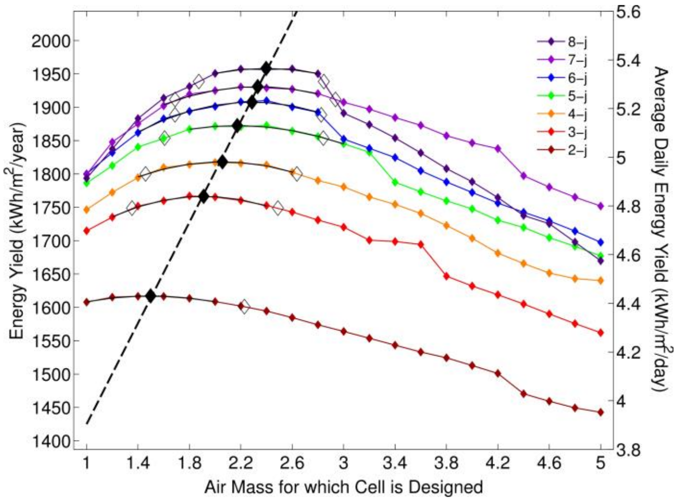

Fig. 4. Clear sky representative spectra for 2-8 junction MJSCs in Ottawa. Annual energy yields as a function of candidate cell design were computed using the AM binning method, assuming no cloud cover and using the representative atmospheric parameters for Ottawa identified in Figure 3.

span the interesting design space and the energy yield these MJSC designs produce is what we compare henceforth.

Annual energy yield is computed for each of the 21 cell designs using one of two approaches. A brute force approach in which local measured spectra are the primary input is used to account for all local irradiance variations in order to validate, by comparison, the use of representative atmospheric parameters in the representative spectrum selection approach we have proposed. The brute force approach requires a large carefully validated data set and is computationally intensive.

The alternative approach treats air mass as the only changing influence on the terrestrial spectrum (all other parameters values are held constant and considered representative) and, in doing so, reduces the simulation time by several orders of magnitude. Computationally intensive brute force energy yield calculations are circumvented by grouping one year's worth of time steps into air mass bins using a solar position calculator [20]. A single energy yield calculation is then performed for the clear sky spectrum at the central air mass of each bin and the results for each bin are added together to get the annual energy yield.

Figure 4 shows clear sky energy yield (left axis: annual; right axis: average daily, or equivalent peak hours per day) in Ottawa for each of the 21 cell designs that correspond to representative spectra. The solid colored data points are the computed values and the lines are guides to the eye. The solid black points are the maxima of 2nd degree fits to the energy yield curve peaks and the open diamonds indicate the 99th percentiles of the energy yield. In **Figure 4** we have tested all 21 members of the set of potential spectral design-points to determine which results in a bandgap combination that maximizes annual energy yield for cells with 1-8 junctions.

The spectra that correspond to each air mass bin employ the various representative atmospheric parameter sets as inputs to SMARTS to generate spectra for a local atmosphere instead of a standard atmosphere. It should be noted that SMARTS does not incorporate a 3 region Angstrom model and that the 2 region approach it provides is not sufficient to quantify local representative spectrum trends. One must turn off all aerosol models in SMARTS and manually apply at least a 3 parameter Angstrom transmission profile as described above to quantify these trends accurately.

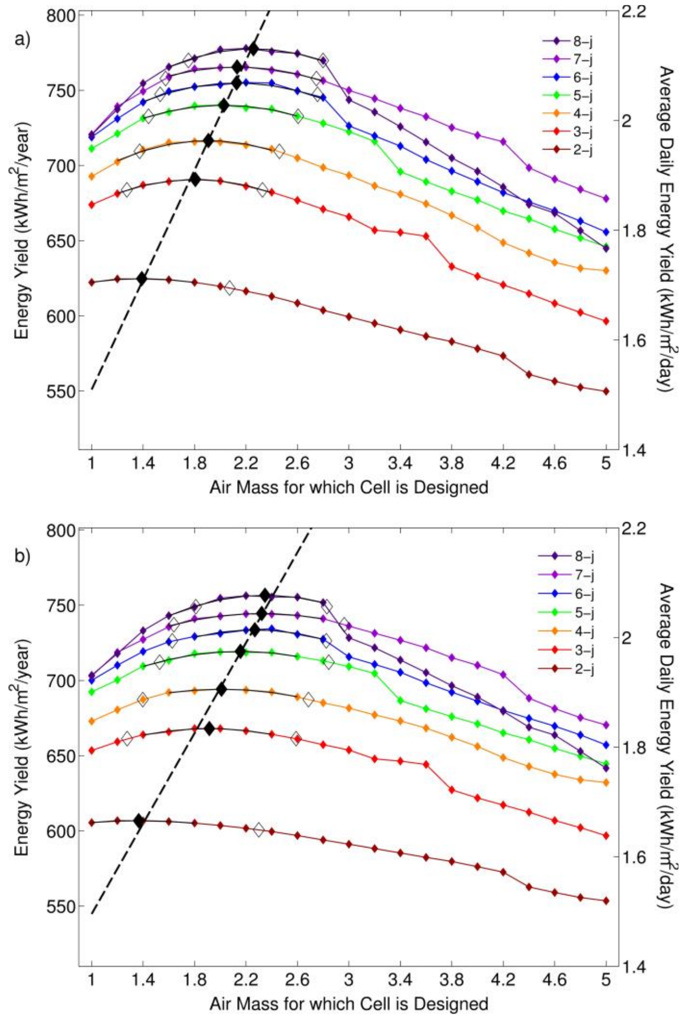

Fig. 5. True representative spectra for 2-8 junction MJSCs in Ottawa. Annual energy yields as a function of candidate cell design were computed a) using the AM binning method, incorporating the effect of cloud cover as a function of AM from Figure 2 and assuming representative atmospheric parameters are constant all year long, and b) using measured spectra which inherently incorporate the influence of all atmospheric dynamics on the irradiance.

It is important to note that the energy yield calculations presented in **Figure 4** are for clear skies and do not consider weather patterns or cloud cover. When using the air mass binning method, weather patterns and cloud cover are accounted for in the final step before summing the energy produced in each air mass bin. This is achieved by scaling the energy produced at each air mass according to the ratio of clear sky to measured DNI presented in **Figure 2**. The resulting energy yield calculations are shown in Figure 5a and discussed in the following section.

IV. Assessment of Representative Parameter Validity

We now proceed with a comparison of representative spectrum trends identified using representative atmospheric parameters vs. those identified using a complete set of measured spectra.

We have used measured spectra in a brute force energy yield calculation with each candidate bandgap combination to determine which would produce the highest annual energy yield in Ottawa. Energy yield calculations were performed for 24,237 unique measured spectra (5 minute time steps) for each of the 21 bandgap combinations, for 1-8 junction MJSC designs. The use of measured spectra means we require no assumptions about atmospheric content. These results are presented in **Figure 5b.**

We have used SMARTS simulated spectra with the representative atmospheric parameters identified in **Figure 3** (but a manually applied aerosol transmission) in conjunction with the air mass binning method and the cloud cover correction from **Figure 2** to compute energy yields in **Figure 5a**.

Figure 5 takes the same format as **Figure 4** but, with all local atmospheric dynamics accounted for in **Figure 5a**, we can now compare the results directly to those of the brute force energy yield calculations in **Figure 5b**.

The plots in **Figure 5** are remarkably similar validating the use of representative parameters as determined in **Figure 3** for representative spectrum selection and ideal bandgap targets for local energy yield optimization. Two subtle expected differences are noticeable however. The first is the 2-3% increase in energy yield predicted in **Figure 5a** vs. **Figure 5b** for cells designed for lower air masses. Less variability in the local spectra when using representative parameters results in low AM designs being more optimal, more of the time. Higher air mass cell designs produce less energy overall but are less sensitive to atmospheric dynamics and thus produce nearly the same energy yield in both plots. The second is the slight decrease in slope of the dashed fit line which relates the energy yield peaks & the representative spectra to the number of junctions in the MJSC. The decrease in slope is a result of a greater shift towards higher air mass representative spectra for cells with more junctions when there is more variability in the local spectrum. This is expected because MJSCs with more subcells are more sensitive to fluctuations in spectral balance which are at play in the brute force calculation. The difference in the trend line between **Figure 5a** and **Figure 5b** and is negligible for the 2-junction case and less than 0.2 AM units in the 8-junction case which amounts to about 2 tenths of a percent change in energy yield. This further validates the use of representative atmospheric parameters in a binned AM calculation as an alternative to a brute force calculation.

V. Coefficients for Representative AOD and PW

If we accept that representative atmospheric parameters are able to capture the broad trends influencing representative spectrum selection for optimal local cell design then it becomes interesting to investigate the independent effect of changing any single representative atmospheric parameter. Such information would allow one to quantify the impact of uncertain atmospheric measurements on the representative spectrum and on the energy yield. We have completed such an investigation by computing annual energy yield for each cell design dozens of times changing only one representative local atmospheric parameter at a time and mapping the effect on the representative spectrum and on the total energy yield.

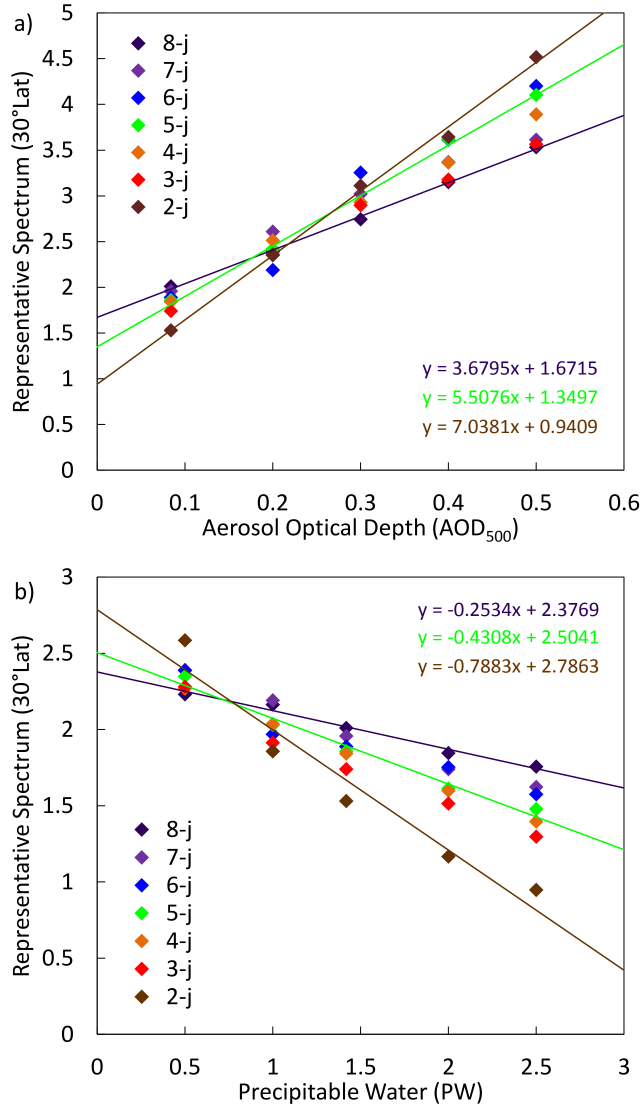

Fig. 6. Representative spectrum as a function of a) AOD with PW of 1.419 cm and b) PW with AOD of 0.084 at 500 nm. The USSA std. ref. atmosphere was used in SMARTS2 to define all other representative atmospheric parameters.

Figure 6 shows the representative spectra for 1-8 junction designs as a function of changing (a) AOD_{500}, and (b) PW. Black trend lines through the 2, 5, and 8 junction results summarize the trend differences for cell designs with different spectral sensitivity.

Several observations can be made from these two plots. First, we note that we have placed linear trend lines through data points that are not necessarily expected to demonstrate linear relationships with the changing representative parameters. The fact that these relationships are close to linear over common ranges of AOD and PW has great empirical significance. It means that there is a very simple (linear) way to map optimal cell designs and energy yield predictions from one location to another simply by estimating the change in representative atmospheric parameters. Increasing representative AOD_{500} results in more scattering on the blue end of the spectrum and progressively higher AM cell designs. Increasing PW results in deeper, wider, absorption dips on the low energy side of the spectrum and progressively lower AM cell designs. In both cases the trends are stronger for cells with fewer junctions, an effect that is partially offset by a greater sensitivity to the design point for MJSCs with more junctions. It is notable that because the optimal 6-junction bandgaps are close to absorption lines, the 6-junction results are much less linear with changing AOD and PW than the other designs.

Nevertheless, the slopes of the linear trend lines can be extracted to determine coefficients for changing AOD and PW. These trends are also weak functions of latitude and are summarized as such in Table 1.

Figure 7 shows annual energy yield for 1-8 junction designs as a function of changing (a) AOD_{500}, and (b) PW. Black trend lines through the results for different numbers of junctions highlight the diminishing energy yield returns for increasing the number of junctions and show the relative impact of AOD and PW on EY for typical ranges. The very slight increase in energy yield observed in the 1-j case in Figure 7b highlights an artifact of the method by which weather patterns are accounted for in the AM binning calculation. Higher PW means the simulated clear sky DNI have less total energy relative to the measured DNI in Figure 2 resulting in a slightly higher ratio as a function of air mass. While this artifact affects the absolute energy estimated, it does not affect identification of the representative spectrum.

VI. Conclusions

We have applied the representative spectrum selection approach in Ottawa and quantified the impact of local spectral information on the calculation. A complete data set of spectral measurements made in 2015 was employed to validate the hypothesis that a set of representative atmospheric parameters could be used to yield the same energy yield and representative spectrum trends. Chan et. al. [23] show results that indicate representative parameters are easier to identify in locations like Rogers Dry Lake where the atmosphere is more consistent throughout the year than it is in Ottawa. While this may be true, we find that even for highly variable atmospheric constituents (such as PW in Ottawa) the value corresponding to 50% cumulative DNI is sufficiently representative to yield the same energy yield and representative spectrum trends as a brute force calculation with a complete set of spectral data.

Finally, we determined coefficients that allow for the mapping of representative spectra (and thus cell designs) and energy yield predictions from one location to another using empirical correlations to representative atmospheric constituents. The coefficients relating the representative spectrum to changes in representative PW and AOD_{500} are tabulated because these are the atmospheric constituents with the greatest impact on the choice of cell design but the methodology works for any parameter affecting the irradiance.

TABLE I
Representative Spectrum Air Mass Coefficients for Aerosol Optical Depth and Water Optical Thickness

	AMu/AODu				AMu/PWcm			
Lat.	0°	15°	30°	45°	0°	15°	30°	45°
2-J	6.4	6.6	7.0	7.2	-0.74	-0.76	-0.79	-0.82
5-J	4.6	4.9	5.5	6.0	-0.40	-0.41	-0.43	-0.44
8-J	3.3	3.4	3.7	4.2	-0.28	-0. 27	-0.25	-0.18

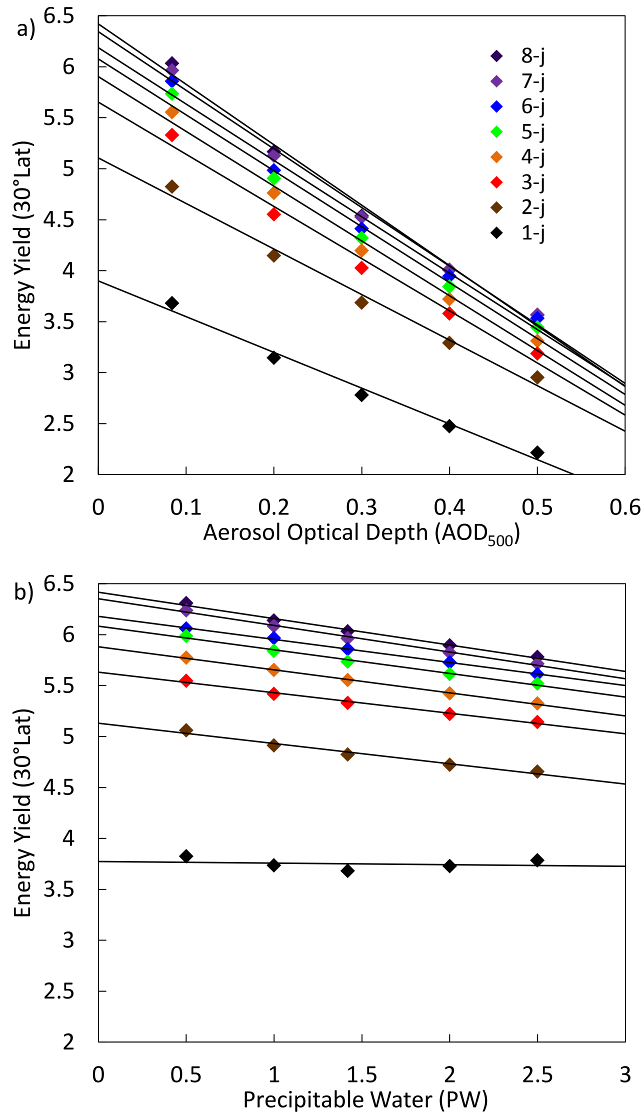

Fig. 7. Annual energy yield as a function of a) AOD, and b) PW. The USSA std. ref. atmosphere was used in SMARTS2 to define all other representative atmospheric parameters.

Acknowledgements

The authors acknowledge Viktar Tatsiankou and Spectrafy for providing the spectral irradiance data used to perform benchmark energy yield calculations for Ottawa.

References

[1] K. Toprasertpong, H. Fujii, T. Thomas, M. Führer, D. Alonso-Álvarez, D. J. Farrell, K. Watanabe, Y. Okada, N. J. Ekins-Daukes, M. Sugiyama,

Y. Nakano, "Absorption threshold extended to 1.15eV using InGaAs/GaAsP quantum wells for over-50%-efficient lattice-matched quad-junction solar cells", *Prog. Photovolt: Res. Appl.* 2015, doi: 10.1002/pip.2585.
[2] R. R. King, D. Bhusari, D. Larrabee, X.-Q Liu, E. Rehder, K. Edmondson, H. Cotal, R. K. Jones, J. H. Ermer, C. M. Fetzer, D. C. Law, N. H. Karam, "Solar cell generations over 40% efficiency." *Prog. Photovolt: Res. Appl.*, 2012, 20:801–815. doi: 10.1002/pip.1255.
[3] G. S. Kinsey, W. Bagienski, A. Nayak, M ingguo Liu, R. Gordon, V. Garboushian, "Advancing Efficiency and Scale in CPV Arrays", *IEEE Journal of Photovoltaics*, vol. 3, no. 2, 2013 pp. 840-843.
[4] F. Dimroth, T. N. D. Tibbits, P. Beutel, C. Karcher, E. Oliva, G. Siefer, M. Schachtner, A. Wekkeli, M. Steiner, M. Wiesenfarth, A. W. Bett, R. Krause, E. Gerster, M. Piccin, N. Blanc, M. Muñoz Rico, C. Drazek, E. Guiot, J. Wasselin, C. Arena, T. Salvetat, A. Tauzin, T. Signamarcheix, T. Hannappel, "Development of high efficiency wafer bonded 4-junction solar cells for concentrator photovoltaic applications", *40th IEEE Photovoltaic Specialist Conference*, Denver, CO, 2014, pp. 840-843.
[5] K. Ghosal, B. Fisher, D. Lilly, J. Gabriel, S. Seel, S. Burroughs, "Ultra High Efficiency HCPV Modules", *42nd IEEE Photovoltaic Specialist Conference*, New Orleans, LA, 2015.
[6] S. Kurtz, M. Muller, D. Jordan, K. Ghosal, B. Fisher, P. Verlinden,J. Hashimoto, D. Riley, "Key parameters in determining energy generated by CPV modules", Prog. Photovolt: Res. Appl. 2015; 23:1250–1259, DOI: 10.1002/pip.2544.
[7] K. Emery, D. Myers, and S. Kurtz, "What is the Appropriate Reference Spectrum for Characterizing Concentrator Cells", *29th IEEE Photovoltaic Specialist Conference*, 2002, pp. 6-10.
[8] D. Myers, K. Emery, and C. Gueymard, "Proposed reference spectral irradiance standards to improve concentrating photovoltaic system design and performance evaluation", *29th IEEE Photovoltaic Specialist Conference*, 2002, pp. 923-926.
[9] D. Myers, K. Emery, and C. Gueymard, "Revising and Validating Spectral Irradiance Reference Standards for Photovoltaic Performance Evaluation", J. Sol. Energy Eng. 126(1), 2004, pp. 567-574.
[10] J. E. Haysom, O. Jafarieh, H. Anis, and K Hinzer, "Concentrated photovoltaics system costs and learning curve analysis," 9th International Conference on Concentrator Photovoltaic Systems (CPV-9), AIP Conference Proceedings, vol. 1556, 2013, pp. 239-243.
[11] S. Tomosk, D. Wright, K. Hinzer, J. E. Haysom, Analysis of Present and Future Financial Viability of High Concentrating Photovoltaic Projects, Chapter 16, *High Concentrator Photovoltaics: Fundamentals, Engineering and Power Plants*. Editors: P. Pérez-Higueras, E. F. Fernández, Springer Green Energy and Technology. Due: Aug. 2015.
[12] J. E. Haysom, O. Jafarieh, H. Anis, K. Hinzer and D. Wright, "Learning curve analysis of concentrated photovoltaic systems," Prog. Photovolt: Res. Appl. (2014), pip. 2567.
[13] M. Yandt, K. Hinzer, H. Schriemer. "Efficient Multi-Junction Solar Cell Design for Maximum Annual Energy Yield by Representative Spectrum Selection", accepted IEEE JPV, June 2016.
[14] I. Garcia, W. E. McMahon, A. Habte, J. F. Geisz, M. A. Steiner, M. Sengupta, D. J. Friedman, "Field Spectra Binning for Energy Production Calculations and Multijunction Solar Cell Design", *42nd IEEE Photovoltaic Specialist Conference*, New Orleans, LA, 2015.
[15] P. J. Verlinden, J. B. Lasich, "Energy rating of Concentrator PV systems using multi-junction III–V solar cells", *IEEE 33rd Photovoltaic Specialists Conference*, San Diego, USA, May 2008 pp. 1-6.
[16] C. Gueymard, "SMARTS2, A Simple Model of the Atmospheric Radiative Transfer of Sunshine: Algorithms and performance assessment", Florida Solar Energy Center, University of Central Florida, Publication number: FSEC-PF-270-95, Original Publication December 1995.
[17] G. Arbez, A. Walker, M. Wilkins, J. F. Wheeldon, A. Trojnar, R. Li, K. Hinzer, H. Schriemer, "4 Junction Dilute Nitride Solar Cell Optimization: Comparing Current Matching Approaches in Detailed Balance Algorithms", *IEEE 39th Photovoltaic Specialists Conference*, Tampa, USA, June 16-21st , 2013.
[18] A. Bett, "etaOpt", Fraunhofer-Institut für Solare Energiesysteme ISE, http://www.ise.fraunhofer.de/de/ geschaeftsfelder/iii-v-und-konzentrator-photovoltaik/ themen/iii-v-epitaxie-und-solarzellen/fue-leistungen/ simulation/etaopt, accessed August 2015.
[19] W. Shockley, H. J. Queisser, "Detailed Balance Limit of Efficiency of p-n Junction Solar Cells", Journal of Applied Physics 32, pp.510-519, (1961).
[20] I. Reda, A. M. Andreas, "Solar Position Algorithm for Solar Radiation Application", Measurement & Instrumentation Team, Solar Radiation Research Laboratory, National Renewable Energy Laboratory, 2003.
[21] C. Gueymard, "Users Manual; SMARTS code, version 2.9.5 for Windows", Solar Consulting Services, USA, December 2005 revised 2006.
[22] V. Tatsiankou, K. Hinzer, J. Haysom, H. Schriemer, K. Emery, and R. Beal, "Design principles and field performance of a solar spectral irradiance meter", Solar Energy 133, 94–102 (2016).
[23] N. L. A. Chan, H. E. Brindley, N. J. Ekins-Daukes. "Impact of individual atmospheric parameters on CPV system power, energy yield and cost of energy", Prog. Photovolt: Res. Appl. 2014; 22(10) 1080–1095, DOI: 10.1002/pip.2376
[24] J. E. Haysom, P. McVey-White, L. de la Salle, K. Hinzer and H. Schriemer, "Multi-year Ground-based Irradiance Dataset in a Northern Urban Climate" (6 pages), 43rd IEEE Photovoltaic Specialists Conference, Portland, OR, USA, June 5-10, 2016.

Mark D. Yandt received the B.Eng.Mgt. degree in engineering physics and management from Mc-Master University, Hamilton, ON, Canada, and the M.A.Sc. degree in electrical and computer engineering from the University of Ottawa, Ottawa, ON, and is currently working toward the Ph.D. degree with the School of Electrical Engineering and Computer Science, University of Ottawa, studying under K. Hinzer and H. Schriemer.

His research interests include the development, characterization, optimization, and deployment of photovoltaic and concentrating photovoltaic systems. He oversees experimental design and system characterization for a number of projects at the Sunlab that involve the dynamics and reliability of high-concentration photovoltaic systems.

Mr. Yandt received an Ontario Graduate Scholarship (OGS) in 2011 and the Alexander Graham Bell Canada Graduate Scholarship (CGS-D) funded by the Natural Sciences and Engineering Research Council of Canada in 2012.

Karin Hinzer (M'08) received the B.Sc., M.Sc., and Ph.D. degrees in physics from the University of Ottawa, Ottawa, ON, Canada, in 1996, 1998, and 2002, respectively.

She is currently an Associate Professor and the Canada Research Chair in photonic nanostructures and integrated devices and an Associate Professor with the School of Electrical Engineering and Computer Science, University of Ottawa. She has made pioneering contributions to the experimental physics of quantum dots marked by two landmark papers in Science. She gained extensive experience in the design and fabrication of group III-V semiconductor devices while with the National Research Council Canada, Nortel Networks, and Bookham. Cost-reduction strategies and liaison with remote fabrication facilities strongly feature in her industry experience. She joined the University of Ottawa in 2007, where she is the founder of the Sunlab, which is a modeling and characterization laboratory specializing in the development of high-efficiency solar cells. Since the laboratory's inception, she has trained more than 80 highly qualified personnel in the field of photovoltaic system and devices. Since 2010, she has been with the Inorganic Photovoltaics Cotheme Leader within the Pan-Canadian Photovoltaic Research Network.

Dr. Hinzer received the Inaugural Canadian Energy Award, with industry partner Morgan Solar, for the development of more efficient solar panels, in 2010.

Henry Schriemer (M'00) received the B.Sc. degree in mathematics and the Ph.D. degree in physics from the University of Manitoba, Winnipeg, MB, Canada, in 1987 and 1997, respectively.

He is currently an Associate Professor of electrical engineering with the University of Ottawa, Ottawa, ON, Canada, where he previously held an NCIT Research Fellowship in photonics from 2003 to 2005. His research interests include engineered complex systems, with a focus on photonic technologies for energy efficiency. His current activities range from the modeling of multi-junction concentrator solar cells and systems, reliability studies and accelerated aging, the development of spectral models that incorporate local weather conditions, and the impact of variable generation on the electrical distribution system. Prior to this, he spent several years in the photonics industry, where he is recognized as one of the innovators of strain-engineered planar lightwave circuits. His previous research accomplishments have ranged from the description of optical singularities in photonic crystals to fundamental advances in the design and realization of laterally coupled-distributed feedback lasers. He has authored more than 70 refereed publications. He held a Postdoctoral Fellowship in laser physics and nanophotonics with the Van der Waals-Zeeman Institute, Amsterdam, The Netherlands, where he made the first measurements of significant spontaneous emission inhibition in active photonic crystals.

5 Software Tools Developed

5.1 Database Video Dashboard

A database dashboard was developed with Jafar Mohamed within the APECS project as a means of visualizing our measured datasets and to compare modeled system performance based on those measurements. This tool facilitated comparison of measured spectral irradiance in Ottawa throughout the year to simulated spectra generated using SMARTS2. It also compared the integrated DNI from these spectra to the measured DNI from the APECS test site. Finally, individual cell performance at every two minute time step and the cumulative annual energy yield were plotted in order to visualize the effect of our measurements on integrated system performance. This dashboard allowed date ranges to be selected for analysis and automatically created videos of the changing data in the data base so that the changing ambient conditions and their effect on a CPV system could be visualized.

5.1.1 Contributions

Mark Yandt: I approached Jafar about this collaborative project to achieve a couple of goals. Having had difficulty performing quality control on ongoing measurements that I needed for my research, I was hoping to develop a way to quickly sanity check the measured data that was being collected on an ongoing basis. I intended this video interface to allow the Sunlab to quickly visualize and sanity check the gigabytes of data that were, by this time, being measured at the APECS test site. Before this interface existed there was no way to efficiently look at the data being collected to see if it made sense or if there was an instrumentation malfunction that needed attention. Snow cover, electrical faults, and network issues often went undetected for too long resulting in missed measurements and a low quality data set.

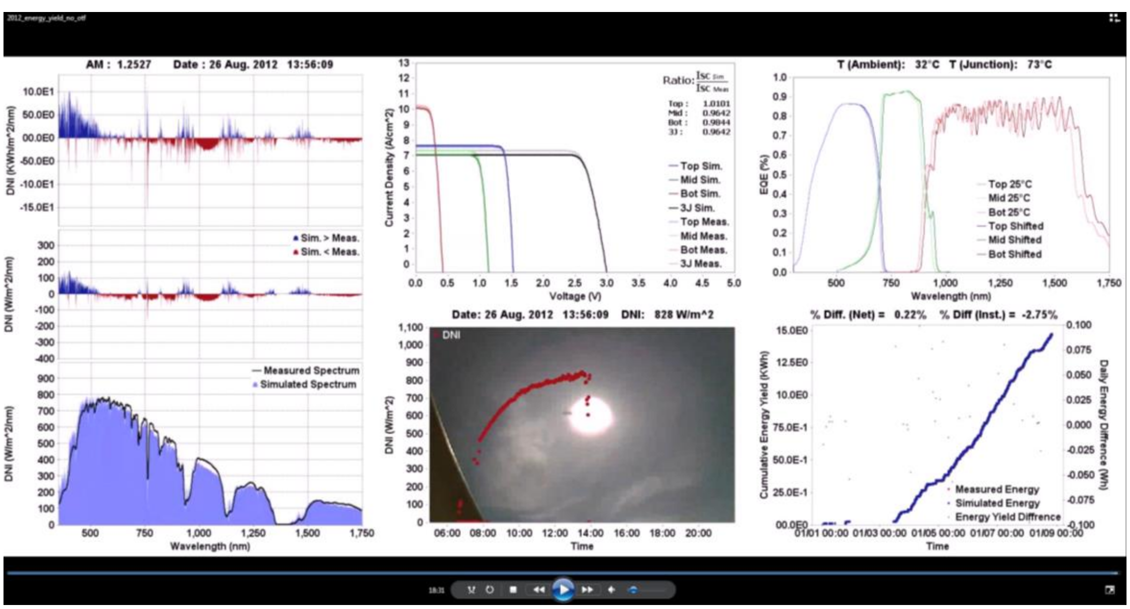

Figure 5: Database dashboard video output showing the cumulative effect of one year worth of measured data on a CPV system had it been deployed at our test site.

Finally, I wanted to be able to quantify the benefit of having local measurements to input into an energy yield model. I built and calibrated an equivalent circuit model (top center in Figure 5) that could use the regular insolation measurements from the test site as input to calculate energy yield over time. The model had the ability to simulate the expected spectral irradiance (blue solid spectrum presented with the measurement in the bottom left of Figure 5 using SMARTS2 based on user specified atmospheric parameters to facilitate comparison to the measurements. I implemented a temperature dependent external quantum efficiency (top right in Figure 5) to emulate the material behavior of a real triple junction solar cell. I then designed the layout and colour scheme and specified the plots that needed to be included in the dashboard.

Jafar Mohammed: Jafar used his software background to efficiently access the data in the database, make the necessary calculations and then restore the outputs that we would later store in a second database. He optimized the test site database decreasing our analysis time from days to hours making annual energy yield calculations feasible in a relatively short period of time. He eventually converted the whole model that I had built in MATLAB into JAVA to facilitate threading and increase the calculation speed even further. A video like that shown by screen shot in Figure 5 with one year worth of data could be packaged in less than two hours.

5.2 Bandgap Optimization

A detailed balance bandgap optimization algorithm previously developed by the Sunlab, *mjOpt* [7] was revised to take advantage of a faster method of calculating cell efficiency given an input spectrum and a set of semiconductor bandgaps. The new method takes advantage of an approximate solution to calculate a cell's ideal conversion efficiency that is more direct than the general numerical method used in the existing software, *mj*Opt.

This new script also includes a very useful visualization tool that allows the viewer to see the bandgap optimization algorithm approaching the efficiency maximizing solution on screen. This is exceptionally helpful when optimizing bandgap combinations for terrestrial spectra because of the large number of absorption lines which have the potential to result in local maxima in the multidimensional efficiency map. Visualizing the solutions gives the user an intuitive feel for how their initial guess and boundary conditions are affecting the solution.

In order to explain the functionality of the new bandgap optimizer [12]we must first understand the steps used to determine cell efficiency (the parameter we want to maximize) from a combination of bandgaps (the parameters we are varying to do so). In a detailed balance calculation we account only for thermalization and transmission losses and thus the first step to finding cell efficiency is to determine the total number of photons in the input spectral irradiance that fall between each set of neighbouring bandgaps. It is assumed that all of these photons are absorbed and collected at the energy of the subcell bandgap doing the absorbing. We start with an initial guess at the optimal bandgap combination and then improve this guess iteratively.

Once the number of photons absorbed by each subcell has been integrated, the light generated current produced by that subcell can be calculated. This is used as input to simulate the IV curve of each subcell. If Eg_1 is the energy bandgap of the top subcell which is larger than Eg_2 which is the bandgap of the next subcell then using Equation 5 from Chapter 2 the current density, J_{L_2}, of the second subcell is,

$$J_{L_2} = q \int_{Eg_1}^{Eg_2} \frac{Irr(\lambda)}{E_{ph(\lambda)}} d\lambda, \tag{10}$$

where $Irr(\lambda)$ is the spectral irradiance in W/m^2/nm and $E_{ph(\lambda)}$ is the energy of a photon at wavelength λ.

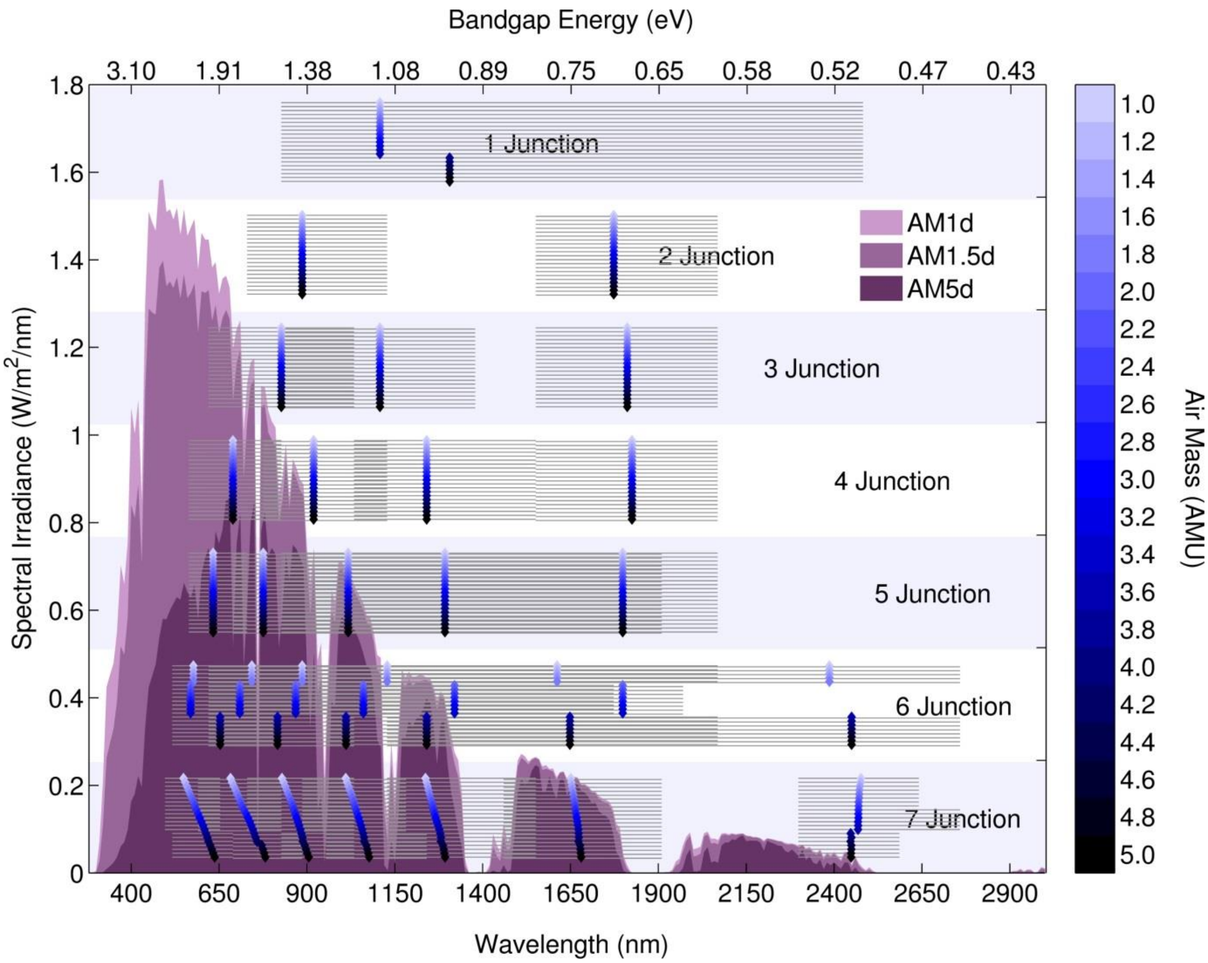

Figure 6: User specified initial guesses for 1-6 junction cell designs and optimized bandgap combinations for a 7 junction cell are shown. This optimization visualization tool shows the user their initial guesses, the optimization constraints (grey lines indicate value limits) and then updates in real time as optimization progresses. The position of the bandgaps relative to the input spectrum and the absorption lines gives the user an intuitive understanding of the optimization problem which has many local maxima so that good initial guesses may be selected.

The IV curve of the subcells is calculated next according to equation 6 assuming parasitic resistances are negligible. Finally we use equations 7 and 8 to compute the bandgap dependent parameter for each subcell. That is, we find the saturation currents, J_o, for each subcell from:

$$J_o = J_w exp\left(\frac{E_g}{k_B T}\right), \quad (11)$$

$$J_w = \frac{2\pi q}{h^3 c^2} k_B T\left[E_g^2 + 2k_B T E_g + 2(k_B T)^2\right], \quad (12)$$

which is a detailed balance limit in which only radiative recombination is considered [20].

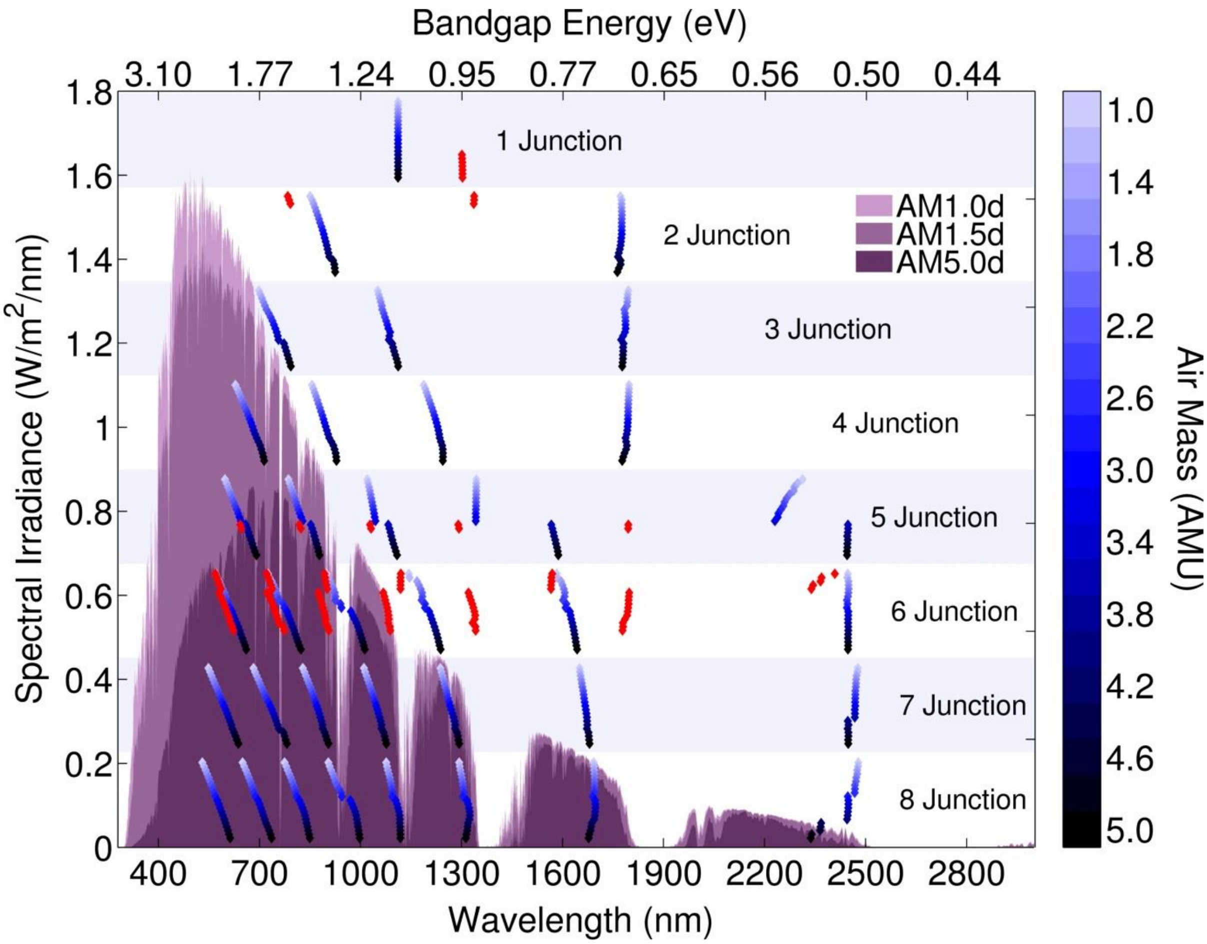

Figure 7: Output from bandgap optimization visualization tool used to watch MATLAB's interior point algorithm converge on the efficiency maximizing bandgap combination for a range of spectral design points between AM1 and AM5.

With the assumptions presented, the IV curves can be calculated analytically and the transcendental diode equation with parasitic resistances present does not need to be solved. This is important for speed. Finally, the new optimizer calculates the IV curves of each subcell at user specified resolution, adds them together in series by summing the spline interpolated subcell voltages at common cell currents and extracts the maximum power point by spline interpolating the multi-junction IV curve near the maximum power point for accuracy. Spline interpolation at each stage is necessary to achieve the 6 digits of precision required to ensure the efficiency map is smooth. Otherwise the interior point algorithm in MATLAB used to converge on the ideal bandgap combination gets caught in local minima and is unable to find the correct solution.

Figure 1 shows the final result of optimizing 1-8 junction bandgap combinations for 21 different input spectra. Three illustrative spectra are plotted in the background for reference against the bandgap positions. Horizontal bands indicate the number of junctions in the optimized combination. The colour graded lines correspond to the colour bar to the right which indicates the air mass of the input spectrum used to simulate the bandgap combination of the same colour.

5.3 Brute Force Energy Yield Calculations

A brute force energy yield calculator was developed such that realistic CPV systems could be modeled given solar resource inputs measured at the uOttawa test sites. This one dimensional model was accomplished with a versatile equivalent circuit model and incorporated the following system effects:

- semiconductor temperature dependence,
- a multi-junction external quantum efficiency (EQE),
- EQE temperature dependence,
- Geometric concentration factor,
- optical transfer function of the optics,
- and the effects of local atmospheric perturbations on the incident spectrum.

The algorithm calculates the energy produced by a multi-junction cell (described by the EQE input) given the ambient conditions (spectral irradiance, temperature), and the system design (concentration factor and optical transfer function). Figure 8 shows an example of annual energy

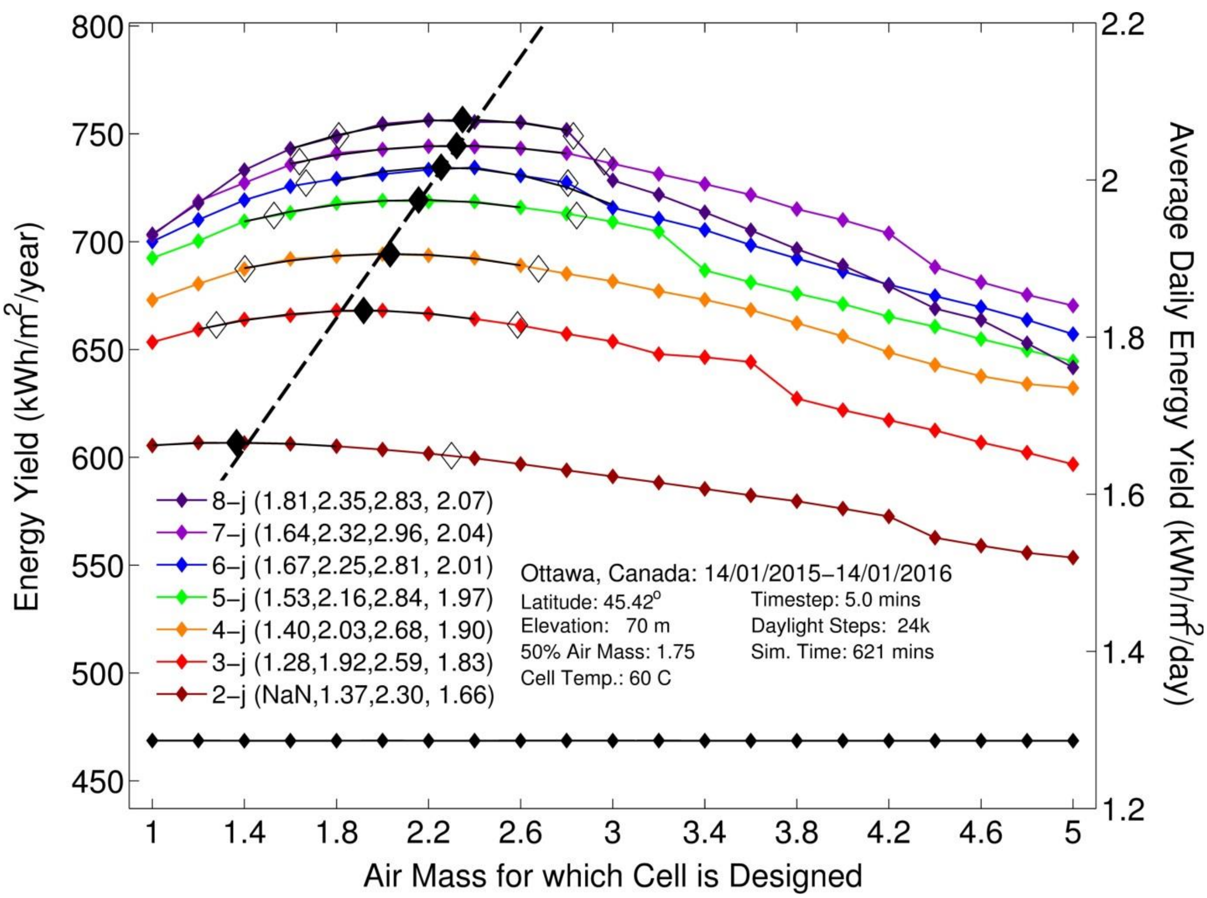

Figure 8: Example of brute force energy yield calculations for 21 different cell designs for 1-8 junction cells.

yield calculations performed to determine the expected CPV system performance in Ottawa given one year worth of measured spectral data from the uOttawa test site. Each diamond is an annual energy yield calculation. The black diamonds are the peaks and the open diamonds are the 99th percentiles. The dashed trend line indicates the change in optimal cell designs as a function of the number of subcells. The simulation details are summarized in the lower right of the plot.

5.4 AM Binning Based Energy Yield Calculations

Energy yield calculations performed at a resolution on the order of minutes can take a long time even in one dimension which does not take into consideration non-uniform illumination, chromatic aberration or temperature distribution across the area of the cell. In order to facilitate energy yield comparisons to determine broad trends in energy yield production as a function of atmospheric constituents for example, it is necessary to accelerate these calculations. Thus, in a separate tool, acceleration of the brute force method was achieved by incorporating an air mass binning algorithm. By approximating the atmospheric content with a standard atmosphere it is possible to use air mass as a proxy for time and eliminate energy yield calculations that are performed for the same air mass but on a different day thus reducing the number of energy yield calculations performed in a year by several orders of magnitude while maintaining the temporal resolution required to resolve the constantly changing position of the sun. The accuracy of the algorithm depends on the ability to find satisfactorily representative constant values for atmospheric constituents. Alternatively, it allows for the analysis of the effect of changing the average value of atmospheric constituents on annual energy yield. The time necessary to complete detailed annual energy yield calculations was reduced by more than 3 orders of magnitude in most cases. The algorithm was validated and used in the work presented in Chapter 4 of this thesis.

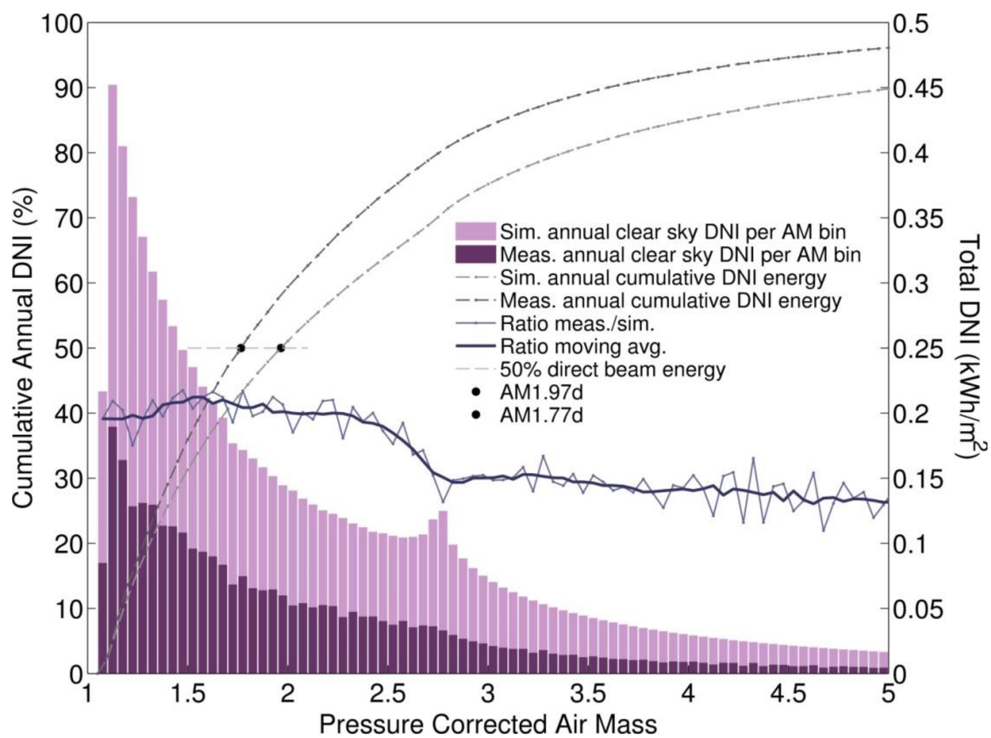

Figure 9: Annual solar resource in Ottawa binned by air mass such that an energy yield calculation can be made for each air mass bin instead of for each timestamp.

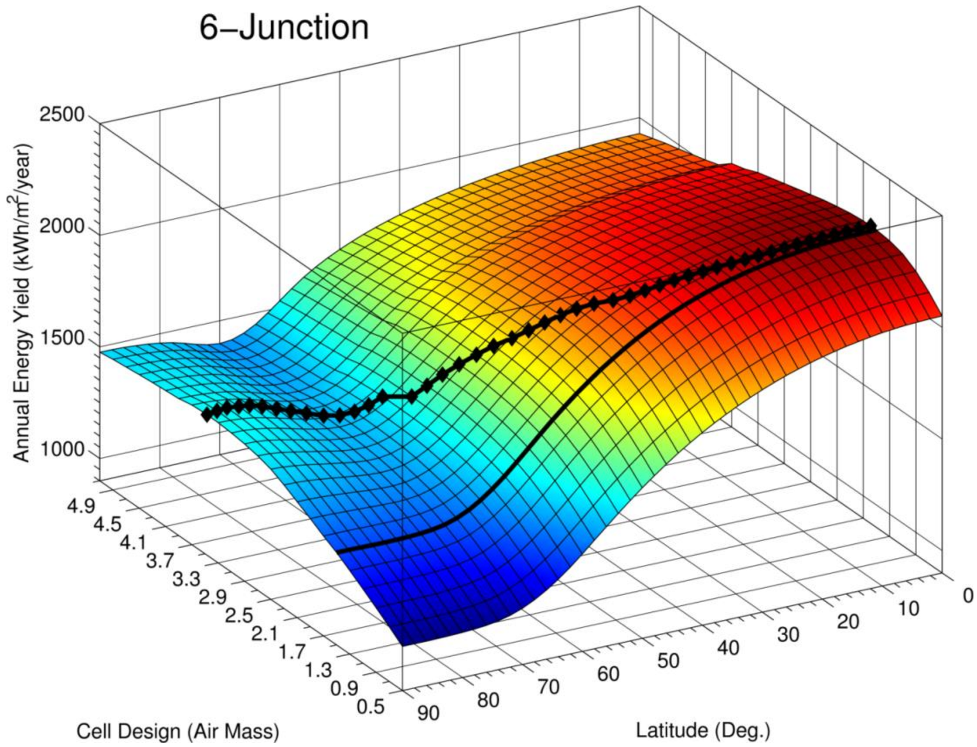

Figure 10: Annual energy yield calculations performed as a function of design point and latitude. The energy yield maximizing design points are indicated for each latitude by black diamonds. Black line indicated AM1.5. An annual energy yield calculation using 30 second time steps sorted into ~750 air mass bins was performed at every vertex to achieve the surface map.

6 Conclusions

At the end of 2016, the photovoltaics industry is a battle ground with fewer and fewer competing forces. Low cost, silicon flat panel manufacturers are forcing those companies with next generation technologies to innovate if they want to compete. Few seem to be up to the challenge. As waves of investment dry up only those with extremely long term vision are able to continue development. Nevertheless, the pursuit continues because the physical limits of photovoltaic technology have not yet been realized. This leaves a strong incentive for innovators to develop new ways of extracting energy from the sun or doing so with existing technology at lower cost. Alongside industrial partners, the Sunlab has positioned itself as a leading contributor to the type of innovation that is necessary. Each of the papers contained in this thesis is a summary of outcomes that were delivered to the Sunlab's industrial partners in the ongoing effort to help make their technologies profitable. The main results are now summarized in context.

In Section 3.1, the paper entitled, "Dynamic Real-Time I–V Curve Measurement System for Indoor/Outdoor Characterization of Photovoltaic Cells and Modules" describes the development of a test station that provides a real time picture of cell or module performance. This capability not only helped in the identification of an important failure mechanism but also provided the Sunlab with in invaluable diagnostic tool that was as versatile as module designs were plentiful. To our knowledge such a technique has never been applied in this type of application with the purpose of capturing dynamic system behavior.

In Section 3.2, the paper entitled, "Shutter technique for noninvasive individual cell characterization in sealed CPV modules" describes a technique that was developed in conjunction with the test station in the previous section. The primary outcome from this work was the non-invasive nature of the technique. It was shown that simply by selectively shuttering optical channels connected in a known electrical configuration it is possible to completely deconvolve the individual cell characteristics. This procedure probes the cells with light in precisely the same fashion that occurs under normal operating conditions. The result is a detailed picture of cell or bypass diode behavior with minimal time investment and almost no system down time or module replacement costs until after a root cause has been identified.

Both of these papers address the need for ever faster development cycles and add value at the implementation stage. This is an important part of research and development as it facilitates the commercial success of a product which ultimately motivates the endeavour in the first place. However, more fundamental questions should also be asked about the next generation technologies that are to be pursued. Several such questions regarding multi-junction solar cell design principles are asked in the latter half of this thesis.

In an attempt to reduce the cost and uncertainty associated with the complexity of the MJSC optimization problem, the final two papers in this thesis aim to prioritize a clear description of the broad trends and provide the reader with an intuitive understanding of the dynamics at play. With these dynamics well understood, detailed methodologies are then presented and validated experimentally which facilitate the development of targets and roadmaps to energy maximizing MJSC designs.

In Section 4.1, the paper entitled, "Maximized annual energy yield using representative spectra" detailed an accelerated methodology for determining energy yield maximizing bandgap combinations given a spectral irradiance dataset. The methodology was used to show the broad trends in optimal cell design as a function of latitude using a standard atmosphere. These trends provide the intuitive understanding necessary to estimate how many cell recipes might be necessary to serve all of the sunny deployment locations and to quantify the penalties for missing these design points. This paper provided a relative understanding of the problem but a demonstration of how local atmospheric dynamics might be incorporated into the analysis was beyond the scope of the work.

In Section 4.2, the paper entitled, “Representative Atmospheric Parameters for Multi-Junction Solar Cell Design” addresses precisely this limitation. It was first shown that representative atmospheric parameters could be used in the representative spectrum selection approach of the previous paper to accurately determine local, energy yield maximizing design points. This result meant that the annual fluctuations in these parameters did not significantly affect the optimal design points if the correct representative parameters were chosen from local data sets. A complete data set of spectral measurements collected in 2015 was employed to validate these conclusions.

Having, first, confirmed the usefulness of representative parameters as inputs to the representative spectrum selection process, and then, shown how to identify such parameters from real measurements, it was finally possible to vary these representative parameters one at a time and map the effect on the representative spectrum and the maximum energy yield. We did so for representative AOD_{500} and PW. The coefficients for linear approximations to these trends are summarized in the following table.

Table 1: Representative Spectrum Air Mass Coefficients for ADO_{500} and PW

Lat.	AMu/AODu				AMu/PWcm			
	0°	15°	30°	45°	0°	15°	30°	45°
2-J	6.4	6.6	7.0	7.2	-0.74	-0.76	-0.79	-0.82
5-J	4.6	4.9	5.5	6.0	-0.40	-0.41	-0.43	-0.44
8-J	3.3	3.4	3.7	4.2	-0.28	-0. 27	-0.25	-0.18

A natural follow up to this analysis would be the application of the technique to well-known historical datasets from sunny locations around the world. The publically available Aeronet atmospheric data could be use to determine performance maximizing cell designs for a broad range of interesting locations. The penalties for missing the ideal bandgap combinations could be quantified and alternative manufacturable cell designs could be recommended given the growth capabilities that are readily available.

REFERENCES

[1] Development of Terrestrial Concentrator Modules Using High-Efficiency Multi-Junction Solar Cells, Proceedings of the 2001 NCPV Program Review Meeting, 2001, p. 281

[2] Wang, X. & Barnett, A., The Effect of Spectrum Variation on the Energy Production of Triple-Junction Solar Cells, IEEE Journal of Photovoltaics, 2012, 2(4), pp.417–423.

[3] S.P. Philipps, G. Peharz, R. Hoheisel, T. Hornung, N.M. Al-Abbadi, F. Dimroth, A.W. Bett, Energy harvesting efficiency of III–V triple-junction concentrator solar cells under realistic spectral conditions, Solar Energy Materials & Solar Cells, 2010, 94:869–877

[4] Dobbin, A.L. et al., How important is the resolution of atmospheric data in calculations of spectral irradiance and energy yield for (III–V) triple-junction cells? In 6th International Conference on Concentrating Photovoltaic Systems: CPV-6. AIP, pp. 303–306.

[5] Chan, N. et al., Variation in spectral irradiance and the consequences for multi-junction concentrator photovoltaic systems. 35th IEEE Photovoltaic Specialists Conference (PVSC), 2010, pp.3008–3012.

[6] M. A. Green, K. Emery, Y. Hishikawa, W. Warta, E. D. Dunlop, Solar cell efficiency tables (version 45) Prog. Photovolt: Res. Appl., 2015; 23:1–9

[7] C. H. Henry, Limiting efficiencies of ideal single and multiple energy gap terrestrial solar cells, Journal of Applied Physics, 1980; 51:4494

[8] R. R. King, Raising the Efficiency Ceiling in Multijunction Solar Cells, Stanford Photonics Research Center Symposium, Sep. 14-16, 2009 Stanford, CA

[9] R. R. King, D. Bhusari, D. Larrabee, X.-Q. Liu, E. Rehder, K. Edmondson, H. Cotal, R. K. Jones, J. H. Ermer, C. M. Fetzer, D. C. Law, N. H. Karam. Solar cell generations over 40% efficiency. Prog. Photovolt: Res. Appl., 2012; 20:801–815.

[10] R. R. King, D. Bhusari, A. Boca, D. Larrabee, X.-Q. Liu, W. Hong, C. M. Fetzer, D. C. Law, N. H. Karam. Band gap-voltage offset and energy production in next-generation multijunction solar cells. Prog. Photovolt: Res. Appl., 2011; 19:797–812

[11] D. C. Law, R. R. King, Y. Yoon, M. J. Archer, A Boca, C. M. Fetzer, S. Mesropian, T. Isshiki, M. Haddad, K. M. Edmondson, D. Bhusari, J. Yena, R. A. Sherif, H. A. Atwater, N. H. Karam. Future technology pathways of terrestrial III–V multijunction solar cells for concentrator photovoltaic systems. Solar Energy Materials & Solar Cells, 2010; 94:1314-1318

[12] K. Ghosal, B. Fisher, D. Lilly, J. Gabriel, S. Seel, S. Burroughs, Ultra High Efficiency HCPV Modules, 42nd IEEE Photovoltaic Specialist Conference, New Orleans, LA, 2015.

[13] S. Kurtz, M. Muller, D. Jordan, K. Ghosal, B. Fisher, P. Verlinden,J. Hashimoto, D. Riley, Key parameters in determining energy generated by CPV modules, Prog. Photovolt: Res. Appl. 2015; 23:1250–1259.

[14] C. Gueymard, SMARTS2, A simple model of the atmospheric radiative transfer of sunshine: Algorithms and performance assessment, Florida Solar Energy Center, University of Central Florida, Publication number: FSEC-PF-270-95, Original Publication December 1995.

[15] J. Nelson, The physics of solar cells, Imperial College Press, London, UK, 2003.

[16] Schoenberg, E.. Theoretische Photometrie, Über die Extinktion des Lichtes in der Erdatmosphäre. In Handbuch der Astrophysik. Band II, erste Hälfte, Berlin, Springer, 1929

[17] I. Reda, A. M. Andreas, Solar position algorithm for solar radiation application, Measurement & Instrumentation Team, Solar Radiation Research Laboratory, National Renewable Energy Laboratory, 2003.

[18] V. Tatsiankou, K. Hinzer, J. Haysom, H. Schriemer, K. Emery, R. Beal, Design principles and field performance of a solar spectral irradiance meter, Solar Energy, 2016; 133 p. 94-102

[19] G. Arbez, A. Walker, M. Wilkins, J. F. Wheeldon, A. Trojnar, R. Li, K. Hinzer, H. Schriemer, “4 junction dilute nitride solar cell optimization: Comparing current matching approaches in detailed balance algorithms”, IEEE 39th Photovoltaic Specialists Conference, Tampa, USA, June 16-21st , 2013 p. 2073-2077.

[20] W. Shockley, and H. J. Queisser. Detailed balance limit of efficiency of p-n junction solar cells,” Journal of Applied Physics, 1961; 32:3, p. 510.